THESIS FOR THE DEGREE OF DOCTOR OF PHYLOSOPY

STRATEGIES FOR PUSHING NONLINEAR MICROSCOPY TOWARDS ITS PERFORMANCE LIMITS

Rodrigo Aviles-Espinosa

The Institute of Photonic Sciences

Thesis Advisor: Dr. Pablo Loza-Alvarez

Barcelona 2013

ACKNOWLEDGEMENTS

I would like to thank my supervisor Dr. Pablo Loza-Alvarez for his endless support and interest the development of this thesis. Thank you creating a very good and nice working atmosphere, for being so positive, and for all the support and advice in each of the projects where I developed this work.
I would also like to thank Dr. David Artigas, for his fruitful and valuable comments through the development of this work.

I was involved in different international projects and had the opportunity to meet, and work with academic and industry researchers which I would like to acknowledge. In the Fast Dot project I collaborated with people from the University of Dundee, the University of Sheffield, Tampere University of Technology, Politecnico di Torino, Technische Universitut Darmstadt, Eidgenössische Technische Hochschule (ETH), the University of Athens, III-V lab (Alcatel Thales), Innolume, Molecular Machines & Industries, MSquared Lasers, Time-Bandwidth Products, and Toptica Photonics. In the Stelum project I worked in collaboration with Imagine Optic.

Most of all, I am very grateful with my girlfriend Elizabeth and all my family: my parents Victor and Gabriela, and my brother Victor for their support.

The work was funded within the Seventh Framework Program "FAST-DOT", through Grant No. 224338, and the EU project STELUM (FP7-PEOPLE-2007-3-1-IAPP, 217997). This work is supported by the Generalitat de Catalunya grant 2009-SGR-159, the Spanish government grant TEC2009-09698, the NoE P4L, and Laserlab optobio. This research has been partially supported by Fundació Cellex Barcelona and has been mostly conducted at ICFO's "Super-Resolution Light Microscopy and Nanoscopy Facility" (SLN@ICFO).

Abstract

The requirement for imaging living structures with higher contrast and resolution has been covered by the inherent advantages offered by nonlinear microscopy (NLM). However, to achieve its full potential there are still several issues that must be addressed. To do so, it is very important to identify and adapt the key elements in a NLM for achieving an optimized interaction among them. These are 1) the laser source 2) the optics and 3) the sample properties for contrast generation. In this thesis, three strategies have been developed for pushing NLM towards its limits based on the light sample interaction optimization.

In the first strategy it is experimentally demonstrated how to take advantage of the sample optical properties to generate label-free contrast, eliminating the requirement of modifying the sample either chemically or genetically. This is carried out by implementing third harmonic generation (THG) microscopy. Here, it is shown how the selection of the ultra-short pulsed laser (USPL) operating wavelength (1550 nm) is crucial for generating a signal that matches the peak sensitivity of most commercial detectors. This enables reducing up to seven times the light dose applied to a sample while generating an efficient signal without the requirement of amplification schemes and specialized optics (such as the need of ultraviolet grade). To show the applicability of the technique, a full developmental study of in *vivo Caenorhabditis elegans* embryos is presented together with the observation of wavelength induced effects. The obtained results demonstrate the potential of the technique at the employed particular wavelength to be used to follow morphogenesis processes *in vivo*.

In the second strategy the limits of NLM are pushed by using a compact, affordable and maintenance free USPL sourcet. Such device was designed especially for two-photon excited fluorescence (TPEF) imaging of one the most widely used fluorescent markers in bio-imaging research: the green fluorescent protein. The system operating parameters and its emission wavelength enables to demonstrate how matching the employed fluorescent marker two-photon action cross-section is crucial for efficient TPEF signal production at very low powers. This enables relaxing the peak power conditions (40 W) to excite the sample. The enhanced versatility of this strategy is demonstrated by imaging both fixed and *in vivo* samples containing different dyes. More over the use of this laser is employed to produce second harmonic generation images of different samples. Several applications that can benefit by using such device are outlined. Then a comparison of the employed USPL source is performed versus the Titanium sapphire laser (the most used excitation source in research laboratories). The final goal of this strategy is to continue introducing novel laser devices for future portable NLM applications. In this case, the use of chip-sized semiconductor USPL sources for TPEF imaging is demonstrated. This will allow taking NLM technology towards the sample and make it available for any user.

In the last strategy, the light interaction with the optical elements of a NLM workstation and the sample were optimized. The first enhancement was carried out in the laser-microscope

optical path using an adaptive element to spatially shape the properties of the incoming beam wavefront. For an efficient light-sample interaction, aberrations caused by the index mismatch between the objective, immersion fluid, cover-glass and the sample were measured. To do so the nonlinear guide-star concept, developed in this thesis, was employed for such task. The correction of optical aberrations in all the NLM workstation enable in some cases to have an improvement of more than one order of magnitude in the total collected signal intensity.

The obtained results demonstrate how adapting the interaction among the key elements of a NLM workstation enables pushing it towards its performance limits.

Resumen

La creciente necesidad de observar estructuras complicadas cada vez con mayor contraste y resolución han sido cubiertas por las ventajas inherentes que ofrece la microscopia nolineal. Sin embargo, aun hay ciertos aspectos que deben ser ajustados para obtener su máximo desempeño. Para ello es importante identificar y adaptar los elementos clave que forman un microscopio optimizar la interacción entre estos. Dichos elementos son: 1) el laser, 2) la óptica y 3) las propiedades de la muestra. En esta tesis, se realizan tres estrategias para llevar la eficiencia de la microscopia nolineal hacia sus límites.

En la primera estrategia se demuestra de forma experimental como obtener ventaja de las propiedades ópticas de la muestra para generar contraste sin el uso de marcadores mediante la generación de tercer harmónico. Aquí se muestra como la selección de la longitud de onda del láser de pulsos ultracortos es crucial para que la señal obtenida concuerde con la máxima sensibilidad del detector utilizado. Esto permite una reducción de la dosis de luz con la que se expone la muestra, elimina intrínsecamente el requerimiento de esquemas de amplificación de señal y de óptica de tipo ultravioleta (generalmente empleada en este tipo de microscopios). Mediante un estudio comparativo con un sistema convencional se demuestra que los niveles de potencia óptica pueden ser reducidos hasta siete veces. Para demostrar las ventajas de dicha técnica se realiza un estudio completo sobre el desarrollo embrionario de *Caenorhabditis elegans* y los efectos causados por la exposición de la muestra a dicha longitud de onda. Los resultados demuestran el potencial de la técnica para dar seguimiento a procesos morfogénicos en muestras vivas a la longitud de onda utilizada.

En la segunda estrategia se diseñó una fuente de pulsos ultracortos que es compacta, de costo reducido y libre de mantenimiento para excitar mediante la absorción de dos fotones uno de los marcadores más utilizados en el entorno biológico, la proteína verde fluorescente. Los parámetros de operación en conjunto con la longitud de onda emitida por el sistema proporcionan la máxima eficiencia permitiendo el uso de potencias pico muy bajas (40 W), ideales para relajar la exposición de la muestra. La versatilidad de esta estrategia se demuestra empleando muestras fijas y vivas con diferentes marcadores fluorescentes. Este láser también es empleado para la obtención de señal de segundo harmónico en diferentes muestras. Adicionalmente, se llevó a cabo un estudio comparativo entre la fuente desarrollada y un sistema Titanio zafiro (uno de los láseres más utilizados en laboratorios de investigación). El objetivo final de esta estrategia es introducir fuentes novedosas para aplicaciones portátiles basadas en procesos nolineales. En base a esto se demuestra el uso de dispositivos construidos sobre un microchip para generar imágenes de fluorescencia de dos fotones. Esto permitirá llevar la tecnología hacia la muestra biológica y hacerla disponible para cualquier usuario.

En la última estrategia se optimiza de la interacción de la luz con los elementos ópticos del microscopio y la muestra. La primera optimización se lleva a cabo en la trayectoria óptica

que lleva el láser hacia el microscopio empleando un elemento adaptable que modifica las propiedades espaciales de la luz. Para mejorar la interacción de la luz y la muestra se miden las aberraciones causadas por la diferencia de índices refractivos entre el objetivo, el medio de inmersión y la muestra. Esto se realizo empleando el concepto de la "estrella guía nolineal" desarrollado en esta tesis. Mediante la corrección de las aberraciones en el sistema de microscopia nolineal se obtiene una mejora, en algunos casos de un orden de magnitud, en la intensidad total medida.

Los resultados obtenidos en esta tesis demuestran como el adaptar la interacción entre los elementos clave en un microscopio nolineal permiten llevar su desempeño hacia los límites.

List of publications:

This thesis is based on the work described in the following papers:

I. **Rodrigo Aviles-Espinosa,** Susana I.C.O. Santos, Andreas Brodschelm, Wilhelm G. Kaenders, Cesar Alonso-Ortega, David Artigas, and Pablo Loza-Alvarez "Third harmonic generation for the study of C. elegans embryogenesis", J. Biomed. Opt. 15(4), 046020 046020-7 (2010).

II. **Rodrigo Aviles-Espinosa,** Pablo Loza-Alvarez and Wilhelm G. Kaenders, "Ultrafast lasers + THG microscopy = flexible in-vivo cell research", BioOptics World. OptoIQ 3, 18-21 (2010)

III. **Rodrigo Aviles-Espinosa,** George Filippidis, Craig Hamilton, Graeme Malcolm, Kurt J. Weingarten, Thomas Südmeyer, Yohan Barbarin, Ursula Keller, Susana I.C.O Santos, David Artigas, and Pablo Loza-Alvarez "Compact ultrafast semiconductor disk laser: targeting GFP based nonlinear applications in living organisms," Biomedical Optics Express. 2 (4), pp. 739-747 (2011). **This paper was ranked 1st (of 38) most important contribution in the Fast-dot project**

IV. **Rodrigo Aviles-Espinosa,** Jordi Andilla, Rafael Porcar-Guezenec, Omar Olarte, Marta Nieto, Xavier Levecq, David Artigas, and Pablo Loza-Alvarez, "Measurement and correction of in vivo sample aberrations employing a nonlinear guide-star in two-photon excited fluorescence microscopy," Biomedical Optics Express, Vol. 2 (11), pp. 3135-3149 (2011).

V. Y. Ding, **R. Aviles-Espinosa**, M. A. Cataluna, D. Nikitichev, M. Ruiz, M. Tran, Y. Robert, A. Kapsalis, I. Simos, C. Mesaritakis, T. Xu, P. Bardella, M. Rossetti, I. Krestnikov, D. Livshits, Ivo Montrosset, D. Syvridis, M. Krakowski, P. Loza-Alvarez, and E. Rafailov, "High peak power picosecond optical pulse generation using a quantum-dot external-cavity passively mode-locked laser and a quantum-dot optical amplifier," Optics Express. 20 (13), pp 14308-14320 (2012). **This paper was ranked 2nd (of 38) most important contribution in the Fast-dot project**

My contributions to the appended papers:

Paper I. I designed and built the Third harmonic Generation (THG) microscope using the laser source provided by Toptica. I performed all the microscopy experiments, the image processing and I wrote the paper. Discussions and revisions were carried out with the coauthors.

Paper II. I prepared the biological samples and I performed all the microscopy experiments, the image processing and I wrote most of the paper in collaboration with the coauthors.

Paper III. I built the experimental setup using the laser source provided by Msquared personnel. I prepared the biological samples and I performed all the microscopy experiments, the image processing and I wrote most of the paper. Some of the coauthors were present in a few experiments. Discussions and revisions were carried out with the coauthors.

Paper IV. The experimental setup built for paper III was upgraded with Adaptive optics. I was involved in this task with the collaboration of Imagine Optic staff. I performed: the software modifications, sample preparation, all the microscopy experiments, the data analysis, and I wrote the paper. Discussions and revisions were carried out with the coauthors.

Paper V. I designed and built the experimental setup (nonlinear microscope part) including the employed software. The laser was provided and installed by University of Dundee with whom I performed the several demonstrations. I wrote the paper sections related with nonlinear imaging**.**

Additional relevant publications

•**Rodrigo Aviles-Espinosa**, R. Porcar-Guezenec, D. Zalvidea, D. Artigas, P. Loza-Alvarez, "Complete optical quality analysis of a non-linear microscope", Focus on microscopy, Krakow (Poland) Paper D09 (2009).

•**Rodrigo Aviles-Espinosa**, Jordi Andilla, Rafael Porcar-Guezenec, Omar Olarte, David Artigas and Pablo Loza-Alvarez, "New technique for aberration measurement and correction in TPEF microscopy", Photonics 4 life, Florence (Italy), (2009)

•**Rodrigo Aviles-Espinosa**, R. Porcar-Guezenec,, D. Artigas, P. Loza-Alvarez, D. Zalvidea "Optical análisis and aberration correction in a nonlinear microscope", Optoel, Malaga (Spain) Paper STD-5 (2009).

•**Rodrigo Aviles-Espinosa**, Jordi Andilla, Rafael Porcar-Guezenec, Omar Olarte, Susana I.C.O. Santos, Xavier Levecq, David Artigas, and Pablo Loza-Alvarez, "Practical optical quality assessment and correction of a nonlinear microscope," Proc. Photonics West, Sanfrancisco C.A (USA), Paper 7570-32 (2010)

•**Rodrigo Aviles-Espinosa**, G. J. Tserevelakis, Susana I. C. O. Santos, G. Filippidis, A. J. Krmpot, M. Vlachos, N. Tavernarakis, A. Brodschelm, W. Kaenders, David Artigas, Pablo Loza-Alvarez, "Cell division stage in C.elegans imaged using third-harmonic generation microscopy," in Proc. Biomedical Optics, Optical Society of America, Wasington,D.C., paper. BTuD78 (2010).

•**Rodrigo Aviles-Espinosa**, G. J. Tserevelakis, Susana I. C. O. Santos, G. Filippidis, A. J. Krmpot, M. Vlachos, N. Tavernarakis, A. Brodschelm, W. Kaenders, David Artigas, Pablo Loza-Alvarez, "Third-harmonic generation microscopy, at 1028nm and 1550nm for the study of C. elegans embryos" in International Summer school in nonlinear optics 2010, 66th Scottish Universities Summer school in physics) P. 01 (2010).

•**Rodrigo Aviles-Espinosa**, Susana I.C.O. Santos, Andreas Brodschelm, Wilhelm G. Kaenders, Cesar Alonso-Ortega, David Artigas, and Pablo Loza-Alvarez "In vivo recordings of morphogenesis in C. elegans embryos using non-invasive Third Harmonic Generation microscopy", in European Molecular Biology Organization, paper. C-196 (2010).

•**Rodrigo Aviles-Espinosa**, Susana I.C.O. Santos, Andreas Brodschelm, Wilhelm G. Kaenders, Cesar Alonso-Ortega, David Artigas, and Pablo Loza-Alvarez "In vivo third harmonic generation microscopy at 1550nm: morphogenesis studies in living Caenorhabditis elegans embryos", in BioPhotonics and Imaging Conference (BioPIC) 2010, paper. C8 (2010).

•**Rodrigo Aviles-Espinosa**, Susana I.C.O. Santos, Andreas Brodschelm, Wilhelm G. Kaenders, Cesar Alonso-Ortega, David Artigas, and Pablo Loza-Alvarez "In vivo third harmonic generation microscopy at 1550nm: morphogenesis studies in living Caenorhabditis elegans embryos", in P4L Paris, France 2010, paper. P02 (2010).

•**Rodrigo Aviles-Espinosa**, Susana I.C.O. Santos, Andreas Brodschelm, Wilhelm G. Kaenders, Cesar Alonso-Ortega, David Artigas, and Pablo Loza-Alvarez ""In-vivo third-harmonic generation microscopy at 1550 nm: three-dimensional long-term time-lapse studies in living C. elegans embryos."", Proc. Photonics West, San Francisco C.A (USA), Paper 7904-50 (2011).

•**Rodrigo Aviles-Espinosa**, G. Filippidis, Craig Hamilton, Graeme Malcolm, Kurt J. Weingarten,Thomas Südmeyer, Yohan Barbarin, Ursula Keller, David Artigas and Pablo Loza-Alvarez, "Compact ultrafast semiconductor disk laser for nonlinear imaging in living organisms." In Proc. Photonics West, San Francisco C.A (USA), Paper 7903-99 (2011).

•Jordi Andilla, Jerôme Ballesta, **Rodrigo Aviles-Espinosa**, Xavier Levecq, "Adaptive optics in sectioning microscopes: the practical implementation," Proc. Photonics West, San Francisco C.A (USA), Paper 79021A-1 79021A-9 (2011).

•**Rodrigo Aviles-Espinosa**, Jordi Andilla, Rafael Porcar-Guezenec, David Artigas and Pablo Loza-Alvarez, "Direct aberrations correction in two-photon microcopy by a single on-axis measurement," ." In Proc. OSA Novel Techniques in microscopy, Monterrey C.A (USA), Paper 1029754 (NWB6) (2011).

•**Rodrigo Aviles-Espinosa**, G. Filippidis, Craig Hamilton, Graeme Malcolm, Thomas Südmeyer, Yohan Barbarin, Ursula Keller, David Artigas and Pablo Loza-Alvarez, "Efficient nonlinear excitation of encoded fluorescent proteins in living samples using a semiconductor disk laser," In Proc. Focus on Microscopy, Konstanz Germany, Paper 39 (2011).

•**Rodrigo Aviles-Espinosa**, and Rafael Porcar-Guezenec, "Presentation of STELUM project: Industry-academy teaming up to push the limits of multiphoton microscopy," In enlightening Bio Light for health program, ICFO Barcelona Spain (2011).

•**Rodrigo Aviles-Espinosa**, Jordi Andilla, Rafael Porcar-Guezenec, David Artigas and Pablo Loza-Alvarez, "Open-loop wavefront sensing scheme for specimen aberrations correction in two-photon excited fluorescence microscopy" In Proc. European conferences on biomedical optics, Munich Germany, Paper 8086-2 (2011)

•**Rodrigo A. Aviles-Espinosa**, George Filippidis, Craig Hamilton, Graeme Malcolm, Kurt J. Weingarten, Thomas Südmeyer, Yohan Barbarin, Ursula Keller, David

Artigas-García, and Pablo Loza-Alvarez, "Portable semiconductor disk laser for in vivo tissue monitoring: a platform for the development of clinical applications," In Proc. European conferences on biomedical optics, Munich Germany, Paper 8092-19 (2011)

•**Rodrigo Aviles-Espinosa**, Jordi Andilla, Rafael Porcar-Guezenec, Omar Olarte, David Artigas and Pablo Loza-Alvarez, "New technique for aberration measurement and correction in TPEF microscopy", Light for Health, Barcelona (Spain), Paper 001 (2011)

•**Rodrigo Aviles-Espinosa**, G. Filippidis, Craig Hamilton, Graeme Malcolm, Kurt J. Weingarten,Thomas Südmeyer, Yohan Barbarin, Ursula Keller, David Artigas and Pablo Loza-Alvarez, "Compact ultrafast semiconductor disk laser for nonlinear imaging in living organisms." Light for Health, Barcelona (Spain), Paper 002 (2011)

•**Rodrigo Aviles-Espinosa**, Jordi Andilla, Rafael Porcar-Guezenec, Marta Nieto, Xavier Levecq, David Artigas and Pablo Loza-Alvarez, "STELUM - Spatio-temporal engineering of Light. Ultimate Multiphoton Microscopy," Marie curie Event, Warsaw (Poland), Paper YH-7 (2011).

•**Rodrigo Aviles-Espinosa**, Craig Hamilton, Graeme Malcolm, Kurt J. Weingarten,Thomas Südmeyer, Yohan Barbarin, Ursula Keller, David Artigas and Pablo Loza-Alvarez, "Portable ultrafast semiconductor disc laser for nonlinear bio-imaging applications." ICFO Corporate Liaison Program, Barcelona (Spain), Paper 02 (2011).

•Pablo Loza-Alvarez, **Rodrigo Aviles-Espinosa**, and David Artigas-García "Multiphoton imaging with compact semiconductor disk lasers," Proc. Photonics West, San Francisco C.A (USA), Paper 8242-23 (2012). (INVITED)

•**Rodrigo Aviles-Espinosa**, Jordi Andilla, Rafael Porcar-Guezenec, Xavier Levecq, David Artigas, and Pablo Loza-Alvarez, "Depth aberrations characterization in linear and nonlinear microscopy schemes using a shack-Hartmann wavefront sensor, " Proc. Photonics West, San Francisco C.A (USA), Paper 8227-49 (2012).

•**Rodrigo Aviles-Espinosa**, "FAST-DOT" Latin American Laser Lab meeting (LASER LAB), Salamanca Spain (INVITED), 2012

•**Rodrigo Aviles-Espinosa**, Y. Ding, M.A. Cataluna, D. Nikitichev, E. Rafailov, and P. Loza-Alvarez "Ultrashort-pulsed chip-sized lasers for two-photon excited fluorescence imaging," In Proc. Focus on Microscopy, Singapore, Paper P1-D13 (2012).

•**Rodrigo Aviles-Espinosa**, J. Andilla, R. Porcar-Guezenec, X. Levecq, D. Artigas, and P. Loza-Alvarez, "The nonlinear guide-star concept: A fast and noninvasive method to measure and correct sample induced aberrations," In Proc. Focus on Microscopy, Singapore, Paper P1-D13 (2012). MO-AF1-PAR-B-3

•**Rodrigo Aviles-Espinosa**, Jordi Andilla, Rafael Porcar-Guezenec, Marta Nieto, Xavier Levecq, David Artigas and Pablo Loza-Alvarez, "STELUM - Spatio-temporal engineering of Light. Ultimate Multiphoton Microscopy," Europhotonics Spring School, Casteldefells (Barcelona), (2012) collocated with Stelum workshop.

•**Rodrigo Aviles-Espinosa**, Y. Ding, M. A. Cataluna, D. Nikitichev, P. Loza-alvarez* and E. Rafailov, "Nonlinear Bio-imaging with a High Peak Power All-Quantum-Dot Master-oscillator Power-amplified System," CLEO 2012, San Jose C.A (USA), Paper ATh1M.2 (2012).

•"Fresh Ways to Shoot Faster Pictures," Interview to Pablo Loza-Alvarez featuring "Compact ultrafast semiconductor disk laser: targeting GFP based nonlinear applications in living organisms" by **Aviles-Espinosa** et al. Biophotonics, 19 (5), 50872 (2012).

•Sylvia Dyballa, **Rodrigo Aviles-Espinosa**, Pablo Loza-Alvarez, and Cristina Pujades, "Sensory versus neuronal cell fate determination? Global cell lineage tracing in the otic vesicle of zebra fish," Universidad Pompeu Fabra, Barcelona (Spain), P04, (2012).

•**R. Aviles-Espinosa**, David Artigas-García and Pablo Loza-Alvarez, "Semiconductor disk lasers for microscopy applications," 24th International Conference of the Society for Medical Innovation and Technology' (SMIT), Barcelona (Spain) FAST DOT project session experts panel INVITED (2012).

•B. Resan, **R. Aviles-Espinosa**, S. Kurmulis, J. Licea-Rodriguez, F. Brunner, A. Rohrbacher, H. Ammann, P. Loza-Alvarez, and K. J. Weingarten, "Multiphoton imaging with low cost 30 fs laser system tunable around 1 micron " NLO50, Barcelona (Spain), Paper MO7 (2012).

List of Abbreviations:

3D	Three dimensional
4D	Four dimensional
AO	Adaptive optics
AR	Anti reflection
C. elegans	*Caenorhabditis elegans*
CCD	Charge coupled device
CFP	Cyan fluorescent protein
CLSM	Confocal laser scanning microscopy
DIC	Differential interference contrast
DM	Deformable mirror
ECMLL	External cavity mode-locked laser
FOM2p	Two-photon figure of merit
FOV	Field of view
GFP	Green fluorescent protein
IR	Infra red
MOPA	Master oscillator power amplifier
NA	Numerical aperture
ND	Neutral density
NIR	Near infrared
NL	Nonlinear
NL-GS	Nonlinear guide-star
NLM	Nonlinear microscopy
PMT	Photo multiplier tube
QD-ECMLL	Quantum dot External cavity mode-locked laser
RMS	Root mean square
SDL	Semiconductor disk laser
SESAM	Semiconductor saturable absorber mirror
SH	Shack Hartmann
SHG	Second harmonic generation
SIU	Super imaging unit
SLD	Super luminescent diode
SNR	Signal-to-noise ratio
SOA	Semiconductor optical amplifier
THG	Third harmonic generation
Ti:S	Titanium:Sapphire
TPEF	Two-photon excited fluorescence
USPL	Ultra-short pulsed laser
UV	Ultraviolet
VCSEL	Vertical cavity surface emitting laser

VECSEL	Vertical external cavity surface emitting laser
WF	Wavefront
WFE	Wavefront error
WFS	Wavefront sensor
YFP	Yellow fluorescent protein

List of Figures

Figure: 3.4. Schematic of the experimental setup used for nonlinear imaging. SDL is the Semiconductor disk laser at 965 nm; M#, mirrors; GM are the galvanometric mirrors; L#, lenses; HM, dichroic mirror; C is the condenser optics (NA = 1.4); F#, band pass filters (F1 transmittance = 330 – 670 nm and F2 transmittance = 475 – 485 nm); and PMT are the photo multiplier tubes.

Figure: 3.5. TPEF images from a) green fluorescent beads and b) mouse intestine section labeled with Alexa Fluor 350 WGA (mucus of goblet cells), Alexa Fluor 568 phalloidin (filamentous actin prevalent in the brush border), and SYTOX Green nucleic acid stain (nuclei of goblet cells). All the images are 500x500 pixels.

Figure: 3.6. 3D projections of a) TPEF signal from neurons forming the nerve ring expressing GFP (blue) and b) SHG signal from the pharyngeal region (orange) of the *C. elegans* nematode. c) Merged TPEF (Green) and SHG (red) images of both structures. The 3D projection is composed of 55 stacks separated 1 μm. A single x-y optical section was taken in less than 2 seconds. For the SHG image an average of 10 frames was applied to improve the signal-to- noise ratio. All the images are 500x500 pixels.

Figure: 3.7. 3D projections of a) TPEF (blue) of a set of motor-neurons expressing GFP and b) SHG (orange) signal of the muscles in the uterus region of a *C. elegans* mid body region. c) Merged TPEF (Green) and SHG (red) images. The 3D projection is composed of 50 stacks separated 1 μm. A single x-y optical section was taken in less than 2 seconds. For the SHG image an average of 10 frames was applied to improve the signal-to-noise ratio. All the images are 500x500 pixels.

Figure: 3.8. TPEF images from different dyes in solution. All the images are 500x500 pixels. PMT voltages are Fluo 4: 819 V, Ca-Green: 757 V, DiO: 711 V, Fluorescein: 510 V, JC1: 478 V and Phantom (paint): 572 V. The field of view of all the images is of 40x40 μm.

Figure: 3.9. Photo-bleaching rate experiments employing the SDL at a constant average power of 34mW at a) the beginning of the imaging and b) after 0.5 hrs of continuous exposure in the nonlinear microscope.

Figure: 3.10. Left panel is the intensity decay as a function of depth. The right panel is the image of a phantom sample obtained employing the SDL prototype at a constant average power of 10 mW. Maximum depth is 230 μm

Figure: 3.11. Schematic of the experimental setup used for nonlinear imaging. SDL is the Semiconductor disk laser at 965 nm; Ti:S is the titanium sapphire laser at 860 nm; M#, mirrors; ND, neutral density filter; L#, lenses; FM1, is the flip mirror; GM are the galvanometric mirrors; HM, dichroic mirror; C is the condenser optics (NA = 1.4); F#, band pass filters; and PMT are the photo multiplier tubes.

1.90 (e) and 2.35 (f); 1.62 (h) and 2.02 (i). The gained improvement factor with respect to the coupling aberrations are 2.06 (c), 1.24 (f), and 1.24 (i). The plot profiles on the last column correspond to green line on each image. The red spot corresponds to the position where the NL-GS was measured. The WFS integration time was set to 800 ms for all the cases.

Figure: 4.12. Single frame images taken from an *in vivo C. elegans* sample. The imaged depths are 115 μm, 125 μm and 135 μm for the first, second and third rows respectively. The improvement factors with respect to the uncorrected case are 1.89 for (b) and 5.32 for (c); 1.58 (e) and 4.78 (f); 1.29 (h) and 9.1 (i). The gained improvement factor with respect to the coupling aberrations are 2.82 (c), 3.03 (f), and 7.08 (i). The plot profiles on the last column correspond to the green line on each image. The red spot corresponds to the position where the NL-GS was measured. The WFS integration time was set to 800 ms for all the cases.

Figure: 4.13. Single frame images taken from an *in vivo C. elegans sample*. The imaged depths are 105 μm, 115 μm, and 127 μm for the first, second, and third rows, respectively. The improvement factors with respect to the uncorrected case are 1.70 for (b) and 17.04 for (c); 2.15 (e) and 11.24 (f); 1.94 (h) and 22.59 (i). The gained improvement factor with respect to the coupling aberrations are 10 (c), 5.23 (f), and 11.66 (i). The plot profiles on the last column correspond to the green line on each image. The red spot corresponds to the position where the NL-GS was measured. The WFS integration time was set to 800 ms for all the cases.

Figure: 4.14. Single frame images taken from mouse brain slices expressing GFP in sparsely distributed neurons. The imaged depths are 10 μm and 40 μm for the first and second rows, respectively. The improvement factors with respect to the uncorrected case are 2.74 for (b) and 5.69 for (c); 1.98 (e) and 3.91 (f). The gained improvement factor with respect to the coupling aberrations are 2.08 (c) and 1.98 (i). The plot profiles on the last column correspond to the green line on each image. The red spot corresponds to the position where the NL-GS was measured. The WFS integration time was set to 1000 ms for all the cases.

List of Tables

Contents

Chapter 1

Introduction

Microscopes have given scientists an extremely important tool to study living organisms since its invention back in the 17th century. The first microscopy device was created by Antonie Van Leeuwenhoek. This apparatus was made of a single lens that enabled the magnified visualization of several samples such as red blood cells, bacteria, microorganisms etc [1, 2].

However, such devices required to be able to resolve adjacent structures within the sample to be observed with the maximum resolution possible. During the following centuries, the microscope was constantly improved with the introduction of optics that corrected chromatic and spherical aberrations.

Chromatic aberrations correction was mainly carried out by employing different types of glass to enable the all the light spectral components to be focused at the same focal position.

On the other hand, spherical aberration could be over passed through the use of diaphragms, or apertures to limit the light angles, as it is a distortion caused when light falls within the edge of a lens, which does not have precisely the same focal distance as the light that comes through the center of the lens. However this could be done at the expense of reducing the numerical aperture (NA), and therefore the achievable resolution, or by making lenses with less curvature, thus limiting its power. This problem was solved by Joseph Jackson Lister in 1830, by showing mathematically that if multiple low-power lenses were placed at certain distance away from each other, the spherical aberration of the first lens remained without any added component from the following lenses. Since the amount of aberration in the first lower-power lens could be reduced to a minimum, the aberration of the whole series would be insignificant even though magnification power was high. These lenses had a low tolerance in their position for proper image correction and the thickness of cover-glass to be used.

To overcome such problem ten years later Andrew Ross made adjustable objectives with a slide or rotating adjustment to correct for the presence of cover-glasses having different thicknesses. The rotation of a collar in the objective was used to adjust two of the lens element groups to either move them closer together or further apart.

With the correction of chromatic and spherical aberrations there was still another factor that impaired the optical performance of a microscope. This was solved by the discovery of

objective designs that achieved the theoretical resolution limit in air. However such designs were manufactured in a trial and error fashion by the microscope manufacturers [2]. The problem was that the microscope objective must collect as large a cone of light as possible from the object to reach the maximum resolution given by the diffraction limit [3]. These concepts where then studied and understand by the work of Ernst Abbe. His theory described how the resolution is ruled by the combination of the angular aperture of the light cone captured by the objective (i.e. the numerical aperture), the wavelength used to illuminate the specimen and the refractive index between the objective and the sample.

Later on, in the late 1870's the NA was increased by the design of an objective used with an immersion medium such as oil, glycerin or water. By using such media, the refractive index was matched to that of the cover-glass. This causes that rays of wider obliquity no longer undergo refraction thus allowing a better collection by the microscope objective maximizing its resolution [3].The use of oil immersion objectives enabled to reach NAs up to 1.4 allowing to resolve points at distances of 0.2 μm apart [2, 4, 5].

These led towards the continuous optimization of different aspects in microscopy such as the illumination characteristics, leading to the improvement of the image contrast. This made possible the invention of various microscopy techniques.

The modern microscopes provide a magnified view of the specimens under study in two and three dimensions (depending on the employed technique). This device is mainly formed by a light source, coupling optics, objective, specimen, condenser and detector. Light microscopy is often based on the Köhler illumination arrangement. Here the coupling and collecting optics are used to project a magnified and focused image of the light filament on the plane of the aperture diaphragm of the collecting optics (i.e. condenser). The condenser gathers the light from the microscope and concentrates it into a cone of light that illuminates the specimen with uniform intensity in its entire field of view (FOV). This optical element must provide an adequate illuminating cone. To achieve this, it must have a NA equal or greater to that of the employed microscope objective [2].

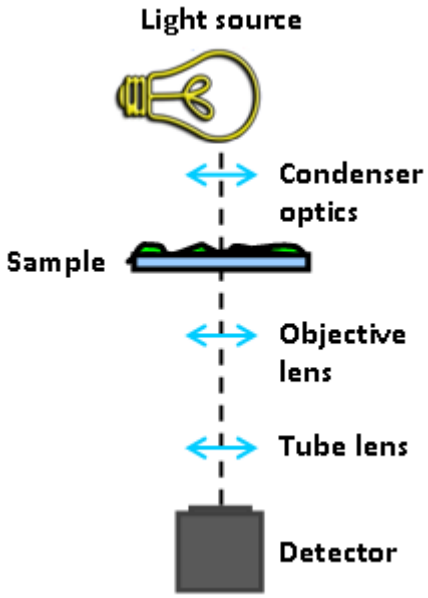

Figure: 1.1. Simplified schematic diagram of a bright field microscopy system. The microscope objective projects an image of the sample at infinity. A tube lens is used to move the image to a finite distance. The detector used for imaging can be positioned in this plane or in a conjugate plane to the image plane.

The objective lens is the most important component of a microscope as it is responsible of primary image formation, determines the magnification, image quality, and resolution. This element acts as a very high magnification lens, thus having a short focal length requiring to be placed very close to the sample under observation. The light from the sample plane is focused by the objective to a point inside the microscope tube lens. This real and inverted image is viewed by the eye piece that may provide additional magnification. Modern microscopes are infinity corrected. This means that the sample image is created at the objective back focal plane which at the same time produces a collimated beam of light that propagates into the microscope tube lens. This beam is brought into focus by the tube lens and forms an image in the back focal plane of the eyepiece. The microscope total magnification is given by the objective times that of the eye piece. Additionally there is an infinity space having parallel beams between the objective and the tube lens. This space is used to place additional microscopy accessories such as prisms, polarizer's, epi-fluorescence light sources etc.

The conventional bright field microscope can only image dark or strongly refracting objects efficiently, providing in some cases poor contrast. This happens because the sample structures usually have similar refractive index when compared with the surrounding medium (water). Thus, only the phase of the light passing through the sample is changed, while an intensity difference is required to achieve a good contrast enabling to separate the object to be studied from the background.

Differential interference contrast (DIC) microscopy was introduced to enhance the contrast in unstained, transparent samples. This technique is based on extracting through interferometric principles, the sample optical path length information to see invisible features.

The design of this microscopy technique is based on a linear polarizer inserted between the light source and the condenser (having an east-west orientation), a condenser Nomarski prism mounted close to the iris in the condenser back focal plane, an objective Nomarski prism mounted behind the objective and an analyzer mounted before the tube lens and the image plane (having a north-south orientation). A different prism is required for each magnification to be used. The image provided by this technique is similar to that obtained by phase contrast microscopy but without the bright diffraction halo. This is removed using the Nomarski prism that recombines the polarization components to reduce such effect [6]. Figure 1.2 shows the schematic if a DIC microscope.

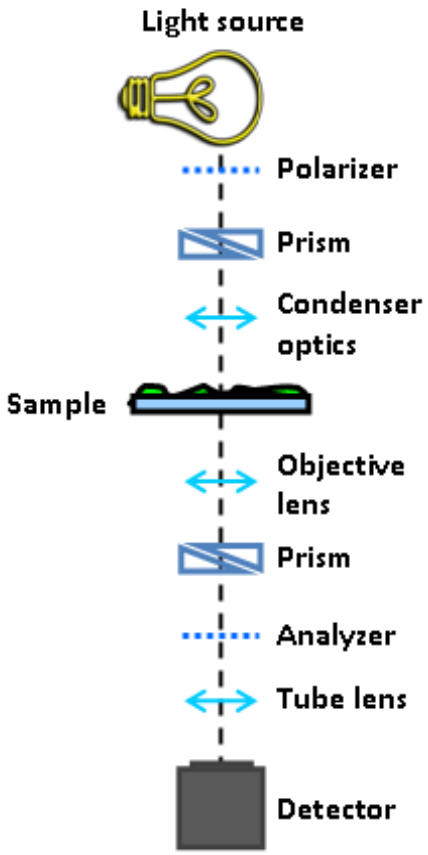

Figure: 1.2. Simplified schematic of a differential interference contrast microscope.

In DIC microscopy, the contrast is produced by the interference between light that has passed through the features of the sample (thickness, slopes and refractive index) producing a phase change and the light that has passed unaffected. This gives the appearance of a pseudo three-dimensional image that corresponds to the variation of optical density in the sample,

emphasizing lines and edges. However, this technique can only image dark or strongly refracting objects efficiently. Therefore other contrast mechanisms have been devised to selectively observe the structure to be studied such as fluorescence based techniques.

1.1. Linear fluorescence microscopy

The detailed study of living microstructures such as cells requires an imaging technique that enables the extraction of only the relevant information for the study to be performed. To enhance the contrast, fluorescence microscopy uses suitable light sources to visualize specific regions in a specimen previously labeled using a dye that selectively bonds to specific structures. Filtering the excitation source reveals the fluorescent dye distribution, showing the labeled structure. This enables a more efficient contrast generation mechanism.

The most important aspect that fluorescence imaging must have is that, it should be non-invasive as the natural evolution of the living organisms to be studied must be preserved, it must be fast, and sensitive.

Fluorescence imaging is based on the reaction that occurs rapidly after the absorption of light. Molecules that have fluorescence properties are known as fluorophores. Fluorescence is a three stage process. This starts when a fluorophore is illuminated using a suitable color of light known as the "excitation light". The energy of this light is absorbed by the fluorophore, changing its electronic state. If the absorbed energy is large enough the fluorophores being in an electronic ground state level (S0) will be excited to a higher but unstable electronic level (S1'). The fluorophore does not remain long at the S1' electronic level and within nanoseconds, it will return back to the electronic ground state through a relaxation process. In this process, energy is released in the form of fluorescent light.

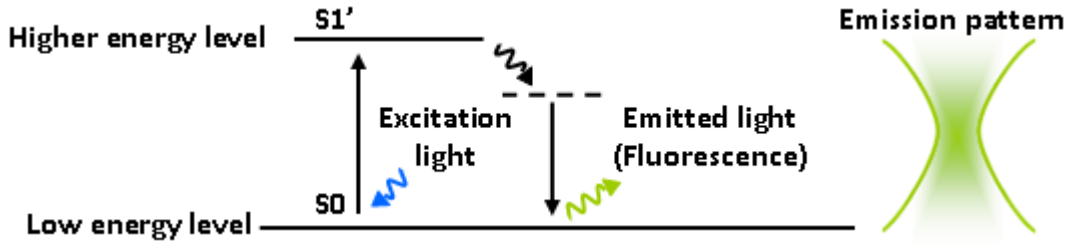

Figure: 1.3. Left panel is the simplified Jablonski diagram. Fluorophores are raised to a higher energy level by the absorption of excitation light. This energy is released at a weaker level or as light of longer wavelength. Right panel is the fluorescence pattern illuminating the whole sample.

Some energy is lost from the fluorophores, during the S1' state and therefore the resulting emitted fluorescence light will contain less energy and thus longer wavelength than the excitation light. The difference between the excitation and emission light is known as the Stokes shift. The most efficient way to generate the highest fluorescence signals is to use the wavelength at the maximum absorption of a particular fluorophore. However, due to the lack of the exact match between the specific light sources there will be cases when these

fluorescent molecules cannot be excited at their peak absorption wavelength. In this case the emission profile of the fluorophore remains unchanged except for a reduction in its emission intensity.

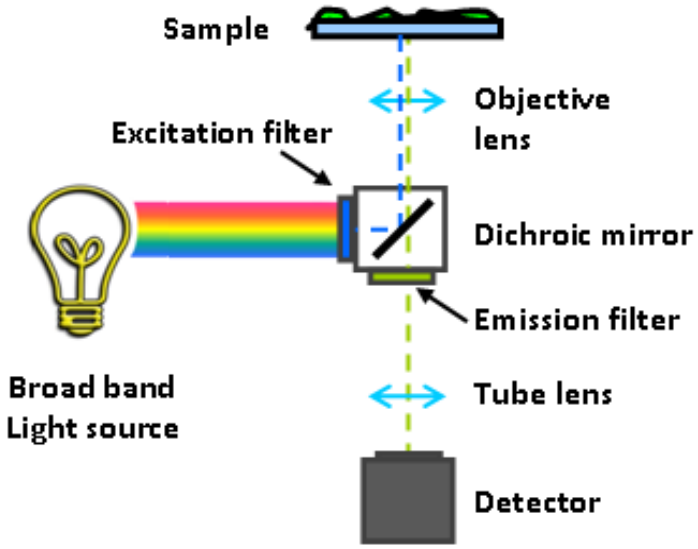

Figure: 1.4. Simplified schematic of the fluorescence microscope. The filter cube is used for separating the excitation and fluorescent emission light.

The most common implementation of fluorescence microscopy uses a broad band light source. The light separation is carried out through a filter cube containing 3 elements (excitation filter, dichroic mirror and emission filter). Firstly the excitation wavelength is selected using an excitation filter. This light is reflected by the dichroic mirror towards the sample, and then the emitted fluorescent wavelengths coming from the sample are transmitted through the dichroic filter. The emission filter is used to separate the fluorescent light from the scattered excitation light (as the dichroic mirror is generally does not all of the reflected excitation light). This allows the fluorescence image to form having a dark background providing contrast of the specimen under study. However, in this type of microscopy, the whole sample is illuminated (see figure 1.3 right panel). This causes fluorescence to originate from all the illuminated planes. The obtained images will therefore suffer from a reduced contrast, low resolution and the inability to distinguish between different focal planes (i.e. for three dimensional imaging).

To overcome these limitations, considerable improvements occurred in the early 1960s with the creation of the confocal microscope [7]. This was the basis for the introduction of confocal laser scanning microcopy (CLSM), a high-resolution microscopy technique which can non-invasively increases the image contrast and resolution. In general, this technique uses clever opto-mechanical components, providing important advances from epi-fluorescence imaging techniques. Here, a laser source passing through a pinhole is coupled to a scan head to raster scan the beam in the x and y directions. Then the beam is enlarged to

take advantage of the full NA of the microscope objective using a beam expander. After passing through a dichroic mirror, light is then coupled onto the microscope objective. This creates an intense diffraction limited spot which is used to image the sample in a point by point fashion (see figure 1.5).

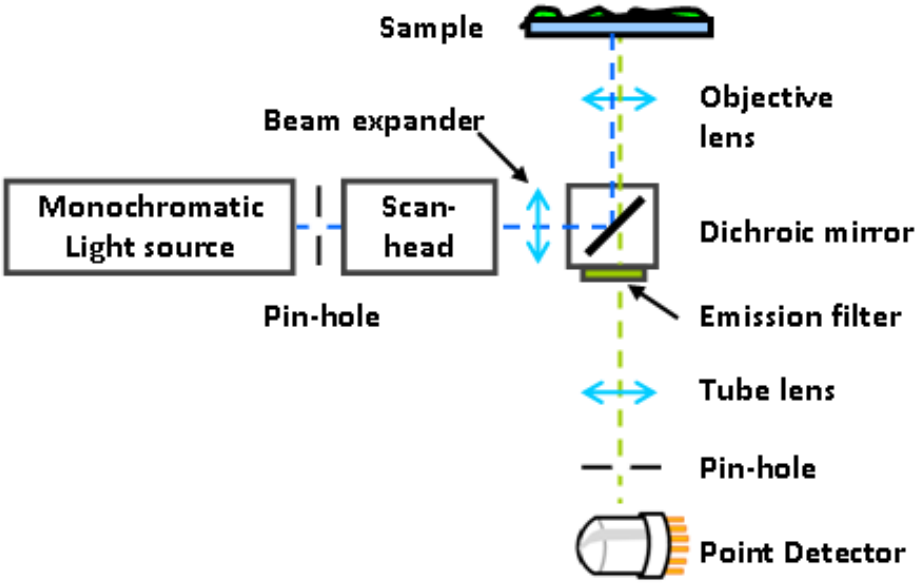

Figure: 1.5. Simplified schematic of the confocal laser scanning microscope.

The emitted fluorescent signal from the specimen (in the same focal point) is collected by the same objective and focused as a confocal point. Fluorescence light coming from above and below is then filtered by a second pinhole to enable the visualization of only what it is at the objective focal plane. This eliminates the blurring effect coming from the adjacent planes and allows having a high contrast and the ability to image the desired focal plane of thick specimens. In fact the addition of this confocal aperture, results in a sectioning capability that allows the researcher to build up three-dimensional (3D) images. Finally the fluorescent signal is separated from the excitation light by using the appropriate filters before entering the point detector (such as a photo multiplier tube).

Although powerful, CLSM is based on linear excitation used to produce fluorescence. This means that it requires short wavelengths (mainly in the ultraviolet and blue-green spectral region) that are prone of causing damage to the sample (photo-bleaching and photo-toxicity). At the same time these wavelengths are strongly scattered by thick specimens, greatly reducing its capability for reaching large penetration depths (limited up to 200μm) [8].

All the techniques presented until this sub chapter are based on the linear interaction of light with the sample. There are several microscopy techniques and other effects where the light is used to interact with the sample in a nonlinear way. This will be discussed in the next subchapter.

1.2. Nonlinear microscopy techniques

When the properties of matter do not depend of the intensity of light, one speaks of linear optics. This situation occurs with low intensity sources such as the ones described in the previous subsection. In this case the behavior of a material to light can be characterized by a set of parameters such as the index of refraction, the absorption and reflection coefficients and the orientation of the material to the polarization of light. These parameters depend only on the nature of the material. This situation changed totally after the development of lasers in the early 1960's which allowed the generation of greater light intensities reaching a kilowatt per square centimeter levels. Such large intensities are now routinely used thanks to the development of ultra-short pulsed laser systems [9].

A pulsed operation of a laser system can be achieved through mode-locking. When a laser system is operating, there are usually several longitudinal modes competing between each other to be amplified. This competition causes fluctuations in the relative phases and amplitudes of the modes. The purpose of locking the modes is to organize this competition in such a way that the relative phases stay constant. This means that if something is inserted inside the cavity which modulates the modes at a frequency close to the intermode frequency interval, the competition for maximum gain inside the amplifying medium will result in a coupling between each mode and the side bands created by the modulation of the neighboring modes. The phases of the modes could then lock onto each other. If these conditions are well chosen the situation may arise where all the energy of the cavity is concentrated in a single pulse [10].

These high peak power systems enabled the discovery of new phase effects taking place during the propagation of pulses through a material. Such effects are mostly related to the large spectral bandwidth of short light pulses which are affected by the wavelength dispersion of the linear index of refraction. [10, 11]

In such large intensity regime the optical properties of a material become functions of the intensity of the radiated light. This intensity dependence of the material response is what defines nonlinear (NL) optics. The distinction between linear and nonlinear regimes can be observed using the polynomial expansion of the polarization of a medium when it is illuminated with an electric field. In such expansion, the linear first order term in the electric field describes linear optics, while the nonlinear higher order terms account for the NL optical effects (i.e. second harmonic generation, third harmonic generation).

In general, these concepts were taken as the basis for the development of several nonlinear microscopy (NLM) techniques. These are based on different types of light sample interactions which may differ according to the biological specimen optical and/or compositional properties. These microscopy techniques can generate contrast based on the use of fluorescent markers such as Two-photon excited fluorescence (TPEF), or based on scattering processes such as second harmonic generation (SHG) and third harmonic

generation (THG) [12]. Such techniques and the contrast mechanism generated by the nonlinear effect will be described in this section.

It is important to keep in mind that what damages a sample is the energy deposition; the trick used in NLM is the use of ultra-short pulsed laser (USPL) oscillators. These sources deliver small amounts of energy in extremely short amounts of time, hence delivering huge amounts of instantaneous powers but with average powers comparable with those used in CLSM. The ultra-short pulse durations are shorter than the relaxation time of the samples. This means that the pulse interacts for a time that it is too short to heat up the sample.

The main advantages of NLM techniques are several. Firstly, as infrared (IR) wavelengths are used, less damage is experienced compared to ultraviolet (UV) excitation. In addition, larger penetration depths are possible, because IR wavelengths are less scattered by tissue [13 -17]. Moreover, the excitation is confined into a localized focal volume (compared to CLSM) that provides intrinsic optical sectioning capabilities (eliminating the use of a confocal aperture). This reduces out of focus photo-damage in all NLM techniques and photo-bleaching for the case of TPEF as fluorescent markers are required. In addition this also enables to reconstruct three dimensional models of the imaged specimens.

One of the first applications of the NL effects in microscopy was TPEF microscopy, which was developed during the early 1990's [18]. In this technique the non linearity relies in the absorption of the excitation light. Two-photon excitation was theoretically described by Maria Göppert-Mayer in 1931. This fluorescence process is based on the simultaneous absorption of two photons. This NL process occurs if the sum of the energies of the two photons is greater than the energy gap between the lower energy and excited electronic states of the molecule. In a more detailed way, what happens is that the first photon induces the transition from the low energy level (S0) to a virtual state, and then a second photon induces the transition from the virtual state to the higher but unstable electronic state (S1'). Fluorescence emission occurs as it was explained for the linear case.

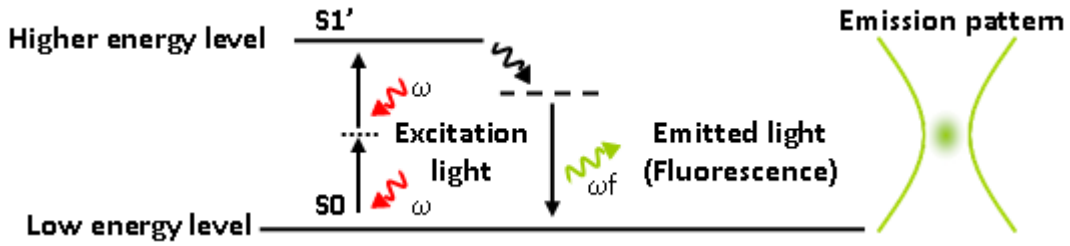

Figure: 1.6. Left panel is the simplified Jablonski diagram. Fluorophores are raised to a higher energy level by the simultaneous absorption of two photons of excitation light. This energy is released at a weaker level or as light of longer wavelength. The right panel shows the emission pattern.

For producing a two-photon absorption process, two photons should coincide in space and time. Therefore, a high photon flux density at the same position (focus) is achieved through the use of a high NA microscope objective. The second condition can be achieved by the use of an USPL, being this element one of the key parts for the development of NLM techniques. Since this process depends on the simultaneous absorption of two photons, the probability of this event to happen is a quadratic function of the excitation radiance. This means that above and below this point the photons are not sufficiently concentrated and therefore two-photon events are less likely to occur. This results in a confined focal excitation volume as the excitation is likely to occur only at the focus of the microscope objective where the intensity is higher. This is very similar to what occurs in CLSM where a pinhole is employed to eliminate the out of focus information. However, in this case the advantage is that no pinhole is required as a focal volume is intrinsically generated due to the nonlinear effect.

The TPEF microscope uses the same principle of image formation as the CLSM (point by point scanning and detection) together with the use of fluorescent markers. The TPEF microscope setup is similar to the CLSM, except that in this microscope the requirement of the pinhole is eliminated. This results in an advantage in the sense that scattered light coming from the sample that would be blocked by the CLSM pinhole, can be detected using TPEF resulting in a signal-to-noise ratio improvement [8].

TPEF microscopes are usually equipped with non-descanned detectors and the required filters, which can be placed in one of the microscope output ports (behind the objective) or on top of the condenser making it simple to implement. The choice of geometry is very important if other NL imaging techniques (SHG, THG) have to be implemented in the same optical setup.

SHG was one of the first effects to be observed after the invention of lasers. In this process two photons having the same angular frequency can be combined when traveling through a suitable material. Thus giving place to the formation of a single photon having twice the original frequency [10].

This can also be observed in terms of an energy level diagram as the one shown on figure 1.7.

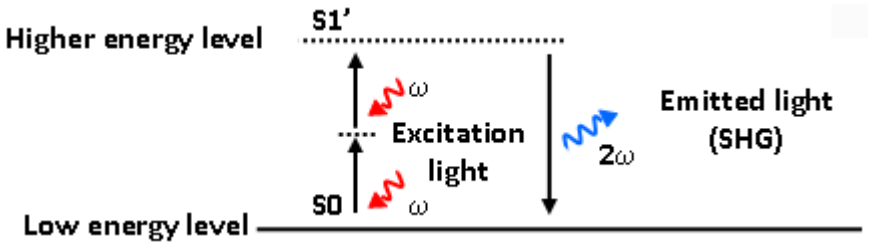

Figure: 1.7. The left panel is the energy level diagram of the second harmonic generation process.

Second harmonic signal originates from the non-linear polarization in non-centrosymmetric materials. In a more detailed view this can be explained by having an input wave generating a set of dipoles inside a given material where all radiate weakly at twice the frequency of the input wave. As the input light has a well defined phase and amplitude at every point inside the material at a given time, the relative phase of the induced dipoles is fixed. To obtain an efficient second harmonic output it is important that the induced dipoles radiate in phase. This process is referred to as phase-matching which ensures that all the contributions from all positions in the material add up constructively promoting the generation of second harmonic signal [11].

As in TPEF, the generated intensity of second harmonic light scales quadratically with the input intensity. By focusing the light to a tiny spot it is possible to achieve higher conversion efficiencies. These concepts were employed for its application into SHG microscopy.

For SHG to take place in a biological sample, structures having a non-centrosymmetric geometry must be present. In such case the requirement of fluorescent markers is eliminated and as a consequence photo-bleaching effects do not occur [19].

As discussed before the same microscopy setup used for TPEF can be employed for SHG. Based on the coherent nature of the SHG process, and that the harmonic is always in phase with the excitation beam, the signal is highly directional and propagates mostly in the forward direction. This requires the use of a forward detector together with a narrow band-pass filter. In this way TPEF can be collected using a backwards detector. Therefore both signals can be obtained in a simultaneous way, giving different but complementary information. The same forward detection mount can also be employed to collect THG signal, in this case also a narrow band pass filter at the appropriate wavelength can be employed.

The following diagram shows a simplified schematic representation employed for NLM.

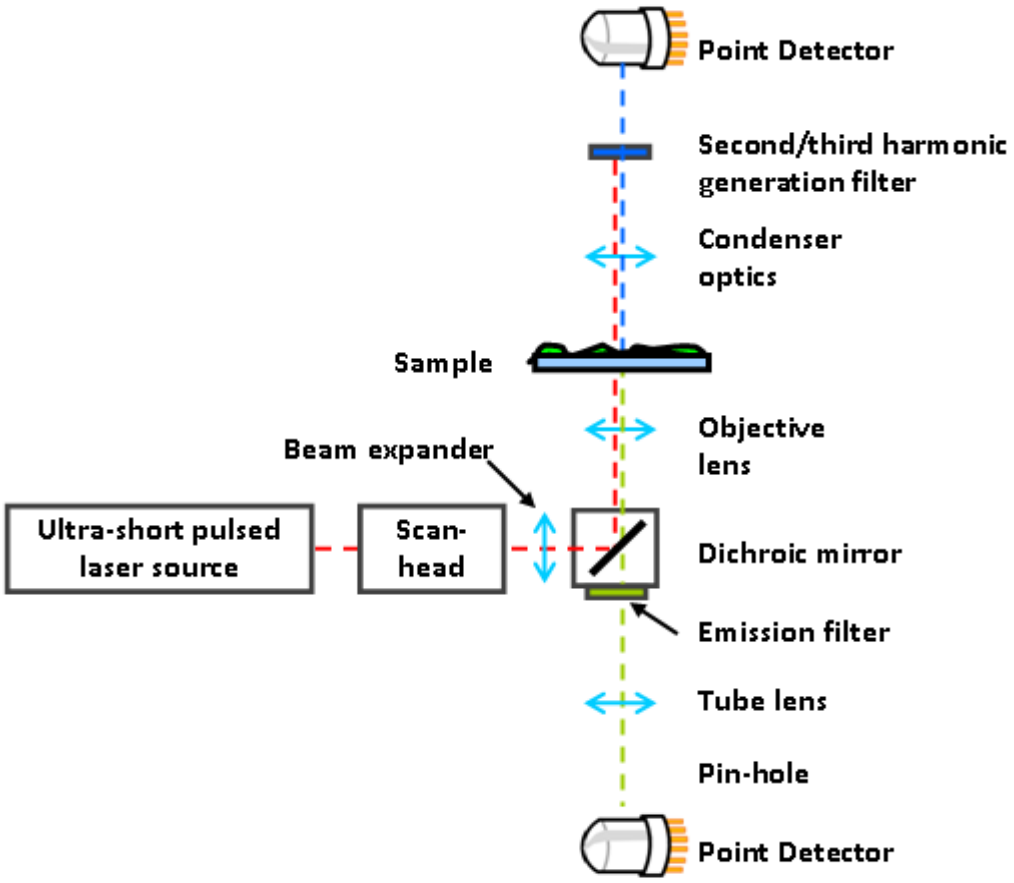

Figure: 1.8. Simplified schematic of the nonlinear microscopy setup used for Two-photon excited fluorescence, second harmonic generation or third harmonic generation imaging.

In THG, tree photons traveling through a suitable material having the same angular frequency are employed to generate a single photon having three times the original frequency [10, 20]. This NL effect depends on an odd order susceptibility which does not disappear in the presence of centrosymmetric materials (see figure 1.9). Therefore THG can be produced even in such type of materials. Here the amplitude of the emitted signal depends on the cube of the incident light intensity thus requiring higher intensities than SHG. This means that THG decreases as the power of three with decreasing excitation intensity, thus providing greater optical sectioning than SHG. As before this emission is a forward directed signal.

From the above it could be thought that THG could be produced on any material. However, in principle it can be produced in any type of media having a non-zero third order nonlinear coefficient ($\chi^{(3)}$). Therefore, in a homogenous, isotropic medium of infinite extension and with normal dispersion, no third-harmonic is generated by a high intensity or tightly focused beam in case of perfect phase matching. This can be explained by considering the Gouy phase shift accumulated by a focused laser beam during its propagation across the focal plane. In this case, the third harmonic emission created before the focal plane interferes

destructively with that generated after the focal plane [21]. In a medium having inhomogeneities either on its refractive index or in the $\chi^{(3)}$ nonlinear coefficient, within the focal volume gives a rise to THG signal.

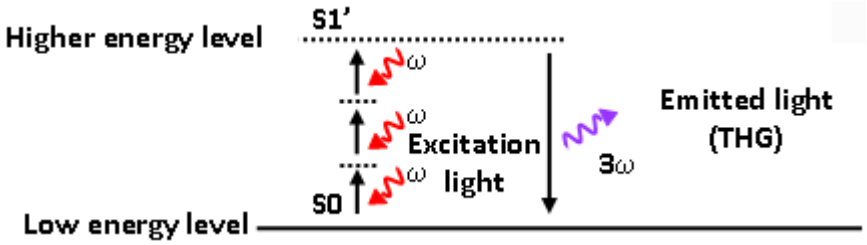

Figure: 1.9. The left panel is the energy level diagram of the Third harmonic generation process.

Because biological samples are typically composed of different structures, THG microscopy can be used to image unlabeled specimens. This is possible as any specimen has structural interfaces such as cells and organelles having inhomogeneous compositions (i.e. refractive index variations), etc. In this sense THG is used as a general tool to produce contrast in any specimen being studied. This, in contrast to labeled based techniques, produce unselective topological information of every interface inside the sample (label based techniques are selective as they can target only the structure of interest). However, THG can be used to follow morphological and developmental processes in a label-free fashion.

As discussed before, the geometry of the employed microscopy setup would be similar to the one employed for SHG (i.e. THG is collected in the forward propagating direction). In addition, as it has been discussed before, TPEF gives information of a labeled structure, while SHG is produced on non-centrosymmetric structures. Moreover, THG gives information of the structural profile of the boundaries inside a sample. This means that THG can be easily combined with the previously mentioned NL techniques giving different but complementary information.

The following table is a summary of the presented nonlinear microscopy techniques describing its applications advantages and disadvantages.

Table 1.1. Confocal laser scanning microscopy comparison versus nonlinear microcopy techniques applications, advantages and disadvantages.

Features	Confocal laser scanning	2-photon excited fluorescence	Second harmonic generation	Third harmonic generation
Excitation	▪ Continuous wave laser in the visible range	▪ Ultra-short pulsed laser in the infrared range	▪ Ultra-short pulsed laser in the infrared range	▪ Ultra-short pulsed laser in the infrared range
Contrast mechanism	▪ Fluorescent markers/Auto-fluorescence	▪ Fluorescent markers/Auto-fluorescence	▪ Non centrosymmetric structures	▪ Interfaces / $\chi^{(3)}$ nonlinearities
Advantages	▪ High resolution achieved using a confocal pinhole	▪ Intrinsic high resolution ▪ Deeper imaging ▪ Reduced out of focus damage	▪ Intrinsic high resolution ▪ Deeper imaging ▪ Reduced out of focus damage ▪ No energy deposition	▪ Intrinsic high resolution ▪ Deeper imaging ▪ Reduced out of focus damage ▪ No energy deposition ▪ General unstained tissue
Disadvantages	▪ Limited Penetration depths ▪ Out of focus photo bleaching and damage ▪ Affected by aberrations ▪ Requires the use of fluorescent markers and wavelength at maximum absorption	▪ Requires using expensive and maintenance intensive laser systems ▪Optical elements not designed for IR wavelengths ▪ Affected by aberrations ▪ Requires the use of fluorescent markers and wavelength at maximum absorption	▪ Requires using expensive and maintenance intensive laser systems ▪Optical elements not designed for IR wavelengths ▪ Affected by aberrations	▪ Requires using expensive and maintenance intensive laser systems ▪Optical elements not designed for IR wavelengths ▪ Affected by aberrations

All these advantages have allowed NLM to become an important tool in biology; however there are still some aspects that may limit its full potential. These are the performance of NL microscopes at IR wavelengths, the use of commercially available laser sources not designed specifically for NLM, and the aberrations caused by the index mismatch between the objective and the sample. These will be discussed in the next subsection.

1.3. Imaging limitations in nonlinear microscopy

1.3.1. The performance of nonlinear microscopy optics at longer wavelengths

As it has been discussed before, NLM techniques benefit from the use of IR wavelengths to overcome the drawbacks of linear based fluorescence microscopy techniques. However commercial systems such as CLSM were already optimized for visible wavelengths. Therefore the existing optics had to be used as a baseline for the development NLM. The optical elements available in commercial microscopy systems were not designed to operate at the IR wavelengths which yielded to low transmission values, and inefficient aberration correction at such wavelength range.

Most of the imaging limitations of multi-photon microscopy appear, as these devices were designed using the existing technologies instead of adapting the imaging device to interact in an efficient way with the optics, the excitation light, and the emitted signal. This is the case of the microscope objective and lenses which are the most important components in a microscope. An important aspect in objective design is the improvement of the antireflection (AR) coating technology which reduces the unwanted reflections that occur when light passes through a lens system. Each uncoated air glass interface can reflect ~5% of an incident beam normal to the surface, resulting in a reduced transmission value of ~95 to 96 % in each element. As objectives become more sophisticated, with the increasing number of lens elements, the need to eliminate internal reflections grows correspondingly greatly reducing the transmittance values to more than a ~50%. This imposes the requirement of having a laser system that must deliver more power to overcome such losses. However, the application of a quarter wavelength thick AR coating with the appropriate refractive index can increase these transmittance values by an additional ~4% on each lens. This results in transmission values up to ~99.9% (in the visible range).

This is of extreme importance if a NLM technique has to be implemented for a specific study given that the employed wavelength in the IR range must be selected according to the required contrast generation mechanism to obtain the desired information. Although this has been started to be addressed by some of the microscope manufacturers, only a few microscope objective designs can be found nowadays.

1.3.2. Commercially available laser systems and fluorescent probes

In terms of the excitation source, the development of multi-photon microscopy was based on the technology available at the time of its invention (1990). Thus a colliding-pulse mode-locked laser was employed to successfully demonstrate the advantages of TPEF [18]. According to [18] nonlinear imaging technology enhancements have been driven by the commercial availability of laser scanning microscopy, fluorescent probes (in the case of TPEF) and the availability of commercial laser sources. Particularly, in the last case, several commercially available laser systems, such as the Ti:Sapphire (Ti:S), have been gradually implemented to extend the capabilities of this nonlinear imaging technique. The Ti:S laser system offers a broad tunability range together with large output powers and short pulse durations [22, 23]. All these advantages were available in a single system at the price of being an expensive device requiring intensive maintenance and having large space requirements.

Five years later after the introduction of TPEF microscopy, another major outcome was the discovery of green fluorescent protein (GFP) [24]. This enabled to mutate animals allowing the expression of such protein. This was carried out by introducing a gene and maintaining it in their genome through breeding, injection with a viral vector, or cell transformation throughout a given organism. This biomarker became a standard as it was possible to introduce it and express the gene in many living organisms including bacteria, fungi, model organisms, mammalians etc. This enabled to establish it as one of the most widely fluorescent markers used in biological research.

A year later after the discovery of GFP (1996), the two-photon action cross section of such fluorescent protein was measured by [13] employing mainly a Ti:S laser system (due its long tunability range). However the power delivered by such laser at the required wavelengths where the maximum two-photon absorption occurs suffers from an important reduction. These findings gave an important area to be targeted on the design of application oriented laser sources to be used specifically for NLM applications. However, laser manufacturers seemed to be more interested mostly on the laser specifications such as widest tuning range, shortest pulse and greatest output power instead of designing a device for targeting the specific needs of NLM techniques (i.e. laser system operating at a wavelength where two-photon absorption is maximum). As a result the developed systems continue to have price, maintenance and space restrictions.

1.3.3. Optical aberrations

In the early design of optical devices, it was found that aberrations are caused by the intrinsic optical elements quality, its alignment, and the refractive index mismatch from the objective, immersion media, and the cover-glass. This leaded to the continuous improvement of imaging optics such as the microscope objective.

Many bio-imaging applications require the use of a cover-glass to mount and protect the specimen. As mentioned on the introduction, these elements, also introduce chromatic and spherical aberrations that must be corrected by the objective design.

Another issue that reduces the optical performance of microscopes is the numerical aperture. Here there are a few critical design parameters of the objective that limit the maximum achievable resolution of the microscope. These are the angular aperture of the light cone emitted by a point, the wavelength of the light used to illuminate the sample as well as the refractive index in the object space between the objective front lens and the specimen.

The imaging media between the objective front lens and the cover-glass is very important with respect to the correction of spherical aberration. Low magnification objectives have a reduced NA and are designed to be used in air as the medium between the objective and the cover-glass. The effect of cover-glass thickness variation is negligible for air objectives having NAs smaller than 0.4, such deviation starts to become important when the NAs start exceeding 0.65 where thickness variations as small as 0.01 mm can introduce spherical aberrations. For example in a phosphate buffered saline medium where the refractive index is significantly different from that of the cover-glass, the objective must focus through a layer of water of a few microns thick. This leads to significant aberrations and a distortion of the point spread function causing the upper and lower planes to be asymmetrical. These factors add to the effective variations in refractive index as well as the thickness of the cover-glass which may be difficult to control.

In an ideal case, light rays passing to the specimen find a homogenous medium between the cover-glass and the immersion objective. Light rays will not be refracted as they enter the lens, but only when they find the surface of the specimen.

Properly corrected oil immersion objectives, also correct for chromatic defects produced by the first two lens elements (hemispherical front end lens followed by a positive meniscus lens and a doublet lens group) while introducing minimal spherical aberration. This is due to the fact that the light cone has partially converged before entering the first lens element which aids the control of spherical aberration [25, 26]. However when the light reaches the specimen under study having unknown optical properties, leads to aberration effects as the index of refraction and sample thickness may be different to the one of the employed immersion fluid. This situation can be found when maximum resolution is required, thus imposing the need of the highest NA possible. In particular, when imaging deep inside thick samples, aberrations can produce important beam degradation leading to reduced image contrast and resolution. Correcting for aberrations will ensure a better focusing, higher peak powers and therefore, a more efficient NL process.

1.4. Strategies for pushing NLM towards its imaging limits

As it has been discussed, the most important aspects to consider for the design of an imaging device are the performance of the optical elements at IR wavelengths, together with the employed excitation source, the optical sample properties and the type of study to be performed. These parameters can be used as the guidelines to develop strategies to push the limits of a NL imaging device.

In this thesis the above mentioned aspects have been taken into account to identify possible opportunity areas of research and what can be implemented to develop several strategies to push NLM towards its limits. These topics were also considered as part of the Fast-dot and the Stelum European projects (where I participated) given that, such research areas are of great importance for the laser development and bio-imaging communities. To do so it has been taken into account what do the available state of the art techniques offer and what would be the most efficient way to address these problems. The approach taken in this thesis work consists on modifying the required elements in a NLM setup to enhance its interaction with the sample to preserve its viability.

The main areas to be targeted will be divided into three chapters.

In chapter two it will be addressed how to take advantage of the light and the sample interaction to gain contrast always taking care of the sample viability. Here it will be experimentally demonstrated how the use of novel laser sources enable to provide label-free techniques reducing sample manipulation. To do so an IR laser system operating at 1550 nm was used to develop a THG microscope. By employing such wavelength the generated signal was emitted in the visible range. This provides the benefit that most of the conventional detectors used for NLM have its peak sensitivity within this range (~516 nm). Moreover, as the signal is emitted within the visible range, there is no requirement of using UV grade optics or signal amplification schemes (as it is done in the conventional THG microscopes). All this enables reducing the amount of power required to image living samples. These advantages are experimentally demonstrated firstly by imaging different *in vivo* samples. Then the system is compared versus a conventional THG microscope operating at 1028 nm to demonstrate the advantages of the developed system. In this part of the research it is demonstrated that possible to reduce seven times the required power to image a sample by using 1550 nm as the excitation wavelength.

To further demonstrate the advantages of employing THG, the system is proposed for solving some of the problems related with developmental imaging such as photo-bleaching effects due to long term imaging. This is carried out by performing a complete study of the developmental process of *in vivo Caenorhabditis elegans* (*C. elegans*) nematodes. Particularly in the cell division stage the THG signal enables a clear identification of the cell nucleus from the surrounding structures. This technique is proposed as a potential way to solve the difficulties of cell tracking experiments where complex algorithms are used to

distinguish between both structures. Finally the wavelength exposure effects on the sample are experimentally investigated showing that THG at the employed wavelength can be used for long term imaging of living samples.

Despite the efforts of showing label-free imaging, the use of fluorescent markers is a highly common and well established practice. In chapter three it is demonstrated how to optimize the interaction of light considering a fluorescent dye inside the sample or a genetically modified sample expressing a fluorescent reporter.

As it was explained before, the most efficient way to generate the highest fluorescence signals is to use the wavelength at the maximum absorption of a particular fluorophore. However, due to the lack of the exact match between the specific light sources there will be cases when these fluorescent molecules cannot be excited at their peak absorption wavelength. In this section it will be presented how the operating parameters of a compact (240 x 140 x 70 mm) USPL source enable an efficient light interaction with the fluorescent dye contained in several biological samples. For this purpose a laser system was designed to operate at 965 nm which is located in the two-photon absorption peak of one of the most widely used fluorescent dyes in biological research, the GFP. To demonstrate the advantages, the results obtained from this research will be presented showing how this enables reducing the peak power from kilowatt to watt level when performing *in vivo* imaging without sacrificing the obtained signal. The extended versatility of the system will be presented by showing the simultaneously obtained SHG signal from the imaged sample. Moreover, it is shown that the presented laser system can be used to efficiently excite other fluorescent dyes. Results outlining the potential applications for which the laser system can be employed are presented. Finally, the compact device is benchmarked versus the Ti:S laser system available in the lab, as a way to outline additional improvements to be performed in the system.

In a similar approach, chip-sized ultra-short pulsed lasers and optical amplification devices where implemented into the NL microscope. Its operating wavelength is centered at ~1260 nm which is located within the infrared penetration window of most biological tissues. This asset could potentially offer greater penetration depths and reduced sample damage compared with the classical ultra-short pulsed laser systems (Ti:S). Preliminary results of TPEF imaging highlight the importance of having non expensive portable, chip-sized systems to push the limits of imaging tools and promote its adoption into clinics, hospitals or even into remote areas. Future implementations include its application into lab-on-a-chip devices, micro endoscopes etc.

In chapter four the imaging limitations produced by aberrations including both the microscope optical elements and the sample are studied. It will be presented how the performance of the NLM can be affected by these, especially when imaging deep inside samples. The strategies used to measure and correct for such aberrations will be introduced to enable the laser light to efficiently interact with all the optical elements in the NLM setup and

the sample. To achieve an efficient interaction with the optical elements in the NL microscope, aberration measurements are performed by implementing a shack-Hartmann wavefront sensor. Then a concept developed in this thesis called the nonlinear guide-star will be introduced to measure sample aberrations to obtain the information of how to modify/adapt the NLM for its further correction. In this section such methodology is experimentally evaluated to demonstrate its applicability. The validation of such concept is carried out by demonstrating that the localized focal volume produced by the TPEF emission generates a secondary light source being this independent from the excitation beam, thus enabling to measure sample induced aberrations. This is followed by demonstrating that such fluorescent focal volume acts as a point source which is required by the wavefront sensor to measure aberrations. It is then demonstrated that a single measurement can be used to efficiently correct for sample aberrations at different depths.

To demonstrate the impact of such methodology, the aberration measured data is used to shape an adaptive element to correct for the NL microscope and sample induced aberrations. The aberration effects produced by *in vivo* samples having different optical properties are then corrected at different depths showing that it is possible to achieve a signal intensity improvement up to 22 times in less than a second. The developed concept enables having a simple and robust methodology which is able to overcome the complexity of current state of the art methodologies also reducing the time to achieve such correction. This enables pushing the limits of NLM bringing several advantages. These include the reduction of the light required to image a sample minimizing sample interference, as well as the ability to provide more information from the studied sample at greater depths.

Finally in chapter five conclusions and future prospects will be outlined. In this section the design of simple but efficient optical devices that further decrease the complexity of the optical NLM setup which I have already started to work with are presented.

References

1. B. J. Ford “Single lens: the story of the simple microscope,” Harper & Row, (1985).
2. G. L. Clark, “The encyclopedia of microscopy,” Reinhold Pub. Corp., pp 445-460 (1961).
3. M. J. Kidger “Fundamental optical design,” SPIE-The international society for optical engineering, (2002).
4. E. Abbe, “A letter from professor Abbe,” The American quarterly microscopical journal 1, 157,159 (1878).
5. H.L. Smith, “Notes on Dr. Abbe’s letter,” The American quarterly microscopical journal 1, 239,240 (1878).
6. A. H. Bennett, H. Osterberg, H. Jupnik, and O. W. Richards, “Phase microscopy; principles and applications,” John Willey and Sons Inc. (1951).

7. M. Minsky, “Microscopy apparatus,” U.S Patent No. 3013467, (1961).

8. P. TC. So, “Two-photon fluorescence light microscopy,” Macmillan Publishers LTD. Nature publishing group1-5 (2002).

9. D. E. Spence, P. N. Kean, and W. Sibbett, "60-fsec pulse generation from a self-mode-locked ti-sapphire laser," Optics Letters 16 (1991).

10. C. Rullière, “Femtosecond laser pulses principles and experiments,” Springer, chapter 2 and 3, (2005)

11. R. W. Boyd, “Nonlinear Optics” Elsevier Science chapter 1, (2003).

12. P. Török, and FJ. Kao, “Optical imaging and microscopy techniques and advanced systems,” Springer, (2003).

13. C. Xu, W. Zipfel, J. B. Shear, R. M. Williams, and W. W. Webb, "Multiphoton fluorescence excitation: New spectral windows for biological nonlinear microscopy," Proceedings of the National Academy of Sciences of the United States of America 93, 10763-10768 (1996).

14. T. Yeh, N. Nassif, A. Zoumi, and B. J. Tromberg, "Selective corneal imaging using combined second-harmonic generation and two-photon excited fluorescence," Optics Letters 27, 2082-2084 (2002).

15. D. Yelin, and Y. Silberberg, "Laser scanning third-harmonic-generation microscopy in biology," Optics Express 5, 169-175 (1999).

16. D. Yelin, D. Oron, E. Korkotian, M. Segal, and Y. Silbergerg, "Third-harmonic microscopy with a titanium-sapphire laser," Applied Physics B-Lasers and Optics 74, S97-S101 (2002).

17. A. C. Millard, P. W. Wiseman, D. N. Fittinghoff, K. R. Wilson, J. A. Squier, and M. Muller, "Third-harmonic generation microscopy by use of a compact, femtosecond fiber laser source," Applied Optics 38, 7393-7397 (1999).

18. W. Denk, J. H. Strickler, and W. W. Webb, "2-photon laser scanning fluorescence microscopy," Science 248, 73-76 (1990).

19. S. Psilodimitrakopoulos, D. Artigas, G. Soria, I. Amat-Roldan, A. M. Planas, and P. Loza-Alvarez, "Quantitative discrimination between endogenous SHG sources in mammalian tissue, based on their polarization response," Optics Express 17, 10168-10176 (2009).

20. L. Moreaux, O. Sandre, S. Charpak, M. Blanchard-Desce, and J. Mertz, "Coherent scattering in multi-harmonic light microscopy," Biophysical Journal 80 (2001).

21. R. S. Pillai, G. J. Brakenhoff, and M. Muller, "Analysis of the influence of spherical aberration from focusing through a dielectric slab in quantitative nonlinear optical susceptibility measurements using third-harmonic generation," Optics Express 14 (2006).

22. P. F. Moulton, "Spectroscopic and laser characteristics of Ti-Al2O3," Journal of the Optical Society of America B-Optical Physics 3 (1986).

23. W. R. Rapoport, and C. P. Khattak, "Titanium sapphire laser characteristics," Applied Optics 27 (1988).

24. M. Chalfie, "Green fluorescent protein," Photochemistry and Photobiology 62 (1995).

25. D. Ganic, X. S. Gan, and M. Gu, "Reduced effects of spherical aberration on penetration depth under two-photon excitation," Applied Optics 39, 3945-3947 (2000).

26. F. Helmchen, and W. Denk, "Deep tissue two-photon microscopy," Nature Methods 2, 932-940 (2005).

Chapter 2

Laser sources for efficient and less disturbing sample imaging

In this chapter the design and characterization of a nonlinear imaging workstation for imaging at longer wavelengths will be described. I will start by describing the design considerations, starting from the microscopy system (coupling the beam into the galvanometric scanner, the beam size adaptation and alignment), then, the impact of the microscope objectives will be analyzed. Here, a microscope objective will be selected based on a performance characterization. Finally the implementation of a forward detection system will be described for the third harmonic generation (THG) experiments.

This will be followed by presenting THG images of different samples and a performance comparison with a conventional THG microscopy device. This will be carried out to demonstrate the advantages of the developed workstation.

Finally, a biological study conducted with this imaging device will be presented for long-term time-lapse imaging studies. This will be presented together with an assessment of the wavelength effects imposed to the imaged samples for large periods.

This will be followed by the final remarks and future prospects for the improvement of this technique.

2.1. Imaging at longer wavelengths: Nonlinear microscopy work station design considerations and characterization.

To demonstrate the advantages of NLM such as reduced scattering, intrinsic optical sectioning, reduced out of focus sample damage etc. The first requirement was to build an imaging workstation being capable of working at longer wavelengths at the infrared (IR) region (750 to 1550 nm). A bright field microscope (Nikon TE eclipse 2000U) was modified to work as a nonlinear (NL) imaging workstation. In this way, the system was developed to eventually host simultaneously several laser inputs to further enable pushing nonlinear microscopy (NLM) towards its limits (i.e. for the full development of this thesis work).

As the device must be able to work at longer wavelengths and reflection losses must be reduced, silver mirrors were selected. This was done given that the reflectivity of such mirrors has an average value of 98% (based on the manufacturer data) at IR wavelengths. In addition to this, the number of required reflections in the setup was reduced as much as possible in the designed path.

To scan the laser beam passing through the microscope objective an x-y galvanometric scanning unit was employed. A non-resonant linear scanner was selected as it enables to raster scan the beam, using a saw-tooth pattern with a relatively slow linear recording time followed by a fast retrace. The benefit of this device is that the scanning speed and rotating angle can be adjusted, thus providing a digital zoom.

A 4-f telescope system or beam expander is required to adjust the beam size of the laser and to image the galvanometric scanning mirrors onto the back aperture of the microscope objective. The design of such element was carried out considering that the entire entrance pupil of a microscope objective must be completely filled to take advantage of its full effective numerical aperture (NA). Uncoated lenses were employed as the NL imaging work station was required to operate at different wavelengths (i.e. from 750 to 1550)

A very important aspect to take into consideration is to have a good conjugation between the galvanometric scanner plane and the microscope objective plane (to have continuous sample illumination). This was as done by checking that the beam reaching the microscope revolver was not being displaced during an x-y scan. To ensure this condition, slight adjustments of the 4-f telescope system distance where carried out until this condition was met.

The objective lenses used in the NL microscope must provide tight focusing conditions to ensure an efficient nonlinear effect while offering at the same time good transmission to minimize losses. In particular, this transmission should be high for both the excitation (in the near IR) and the generated wavelengths (in the visible region). Based on this requirement, the performance from several microscope objectives available in the lab were characterized employing the laser operating at a central wavelength of 1550 nm.

Table 2.1. Microscope objectives characterization at 1550 nm.

n	Media	Objective/ NA	Specialized optical properties	Aberration correction	Transmittance @1550nm	Calculated Intensity [mW/μm^2]
1	AIR	10x/0.3	DIC	Plan fluor	64.5%	0.002
1	AIR	20x/0.45	PH1	Plan fluor	53.2%	0.006
1	AIR	20x/0.4	PH1	-	40.1%	0.002
1	AIR	40x/0.95	DIC	Plan Apo	29.9%	0.034
1.51	OIL	40x/1.3	DIC	Plan fluor	20.6%	0.051
1.51	OIL	60x/1.4	DIC	Plan Apo	15.4%	0.037

The transmittance of each microscope objective was measured experimentally by comparing the measured average power at the microscope revolver with that after passing through each microscope objective. The results are shown on table 2.1 where the calculated intensity, has been obtained taking into account their respective NA.

As a NL effect is dependent on the intensity, it is clear from these results that the 40x 1.3 NA microscope objective is the best choice, as it combines good transmission together with a high NA.

The emitted signal from the sample must be collected with a lens having similar or higher NA than the employed excitation objective, to capture the more scattered emissions. For this reason, the 0.52 NA air condenser was changed for a 1.4 NA oil immersion type.

To detect the signal, a de-scanned detection scheme was employed as the NL signal is recorded in a point by point fashion (as explained before) and stored into a two dimensional matrix. For that, a photomultiplier tube (PMT) was used to collect the emitted signal photons. The choice of detector was based on the best compromise between its quantum efficiency and noise characteristics.

Based on the above measurements and calculations, the NLM workstation was built. The configuration employed for THG imaging will be presented on the next subchapter. In this part, the importance of developing techniques or strategies to push NL imaging technology towards its limits will be outlined. To carry out the biological studies presented in this thesis, it has been taken into consideration that the sample interference must be reduced as much as possible. In other words, the utilized method should not alter the specimen natural evolution. At the same time these imaging techniques should be able to minimize the sample preparation procedures, allow extended sample viability during the whole imaging process and provide enough spatial resolution to capture information in the sub-cellular level.

2.2. Third harmonic generation based imaging

In this section, the application and versatility of the developed imaging device will be demonstrated by presenting THG images of several samples. A comparison of the developed imaging platform with another system used to perform THG imaging will be presented. Finally, the application of this device will be demonstrated as a potential solution for the current difficulties of morphogenesis studies. This will be done by presenting the results obtained for long-term time-lapse imaging studies of *C. elegans* embryos morphogenesis.

In particular, in the past, the use of wavelengths within the range of the 1500 nm from a synchronously pumped optical parametric oscillator has been reported. In these experiments, fixed samples such as neurons and epithelial cells have been imaged using the THG technique [1]. Other demonstrations indicate that fiber based femto-second lasers could be used for such purposes. These lasers have aided on the simplification and integration of NLM techniques into biology, thanks to their compact design, output wavelength, pulse duration and repetition rates. These lasers use reliable state-of-the-art telecommunications components that have been developed for long-term operation, minimum maintenance and moderate costs. Thus, in the past, a fiber laser operating at 1560 nm has been used to produce THG images of chloroplasts and flowing erythrocytes [2].

For THG imaging, the NLM workstation was based on a compact erbium fiber pulsed laser system (Toptica Photonics, FemtoFiber FFS laser) operating at a central wavelength of 1550 nm, having a pulse duration of 100 fs and a repetition rate of 107 MHz. The laser output average power was ~350 mW.

An RG1000 filter (Schott, transmittance: 830 – 2000 nm) was placed at the laser output to block any spurious signal below 1000 nm from the laser itself. The microscope is equipped with a pair of x-y galvanometric mirrors (Cambridge Technology, 6215H) used to scan the excitation beam over the sample. A filter cube, containing a dichroic mirror (Thorlabs, DMSP 1000) to direct the excitation beam towards the sample was used. Based on the results obtained in subsection 2.1, a 40x oil immersion microscope objective with NA = 1.3, (Nikon, Plan Fluor) was used during the experiments. The measured average power (at the sample plane) was 4.9 mW which corresponds to 460 W peak power.

The THG signal was collected by an oil immersion condenser NA = 1.4, (Nikon). A custom-made forward detection mount using an attached PMT (Hamamatsu, H9305-04) to detect the THG signal at the central wavelength of 516nm was employed. This mount contains a band pass filter to separate the fundamental beam from the generated THG signal (Semrock, transmittance: 512 - 521 nm). A home-made LabView interface was used to control both scanning units and the data acquisition card. Figure 2.1 shows a schematic of the real arrangement mounted for the THG experiments.

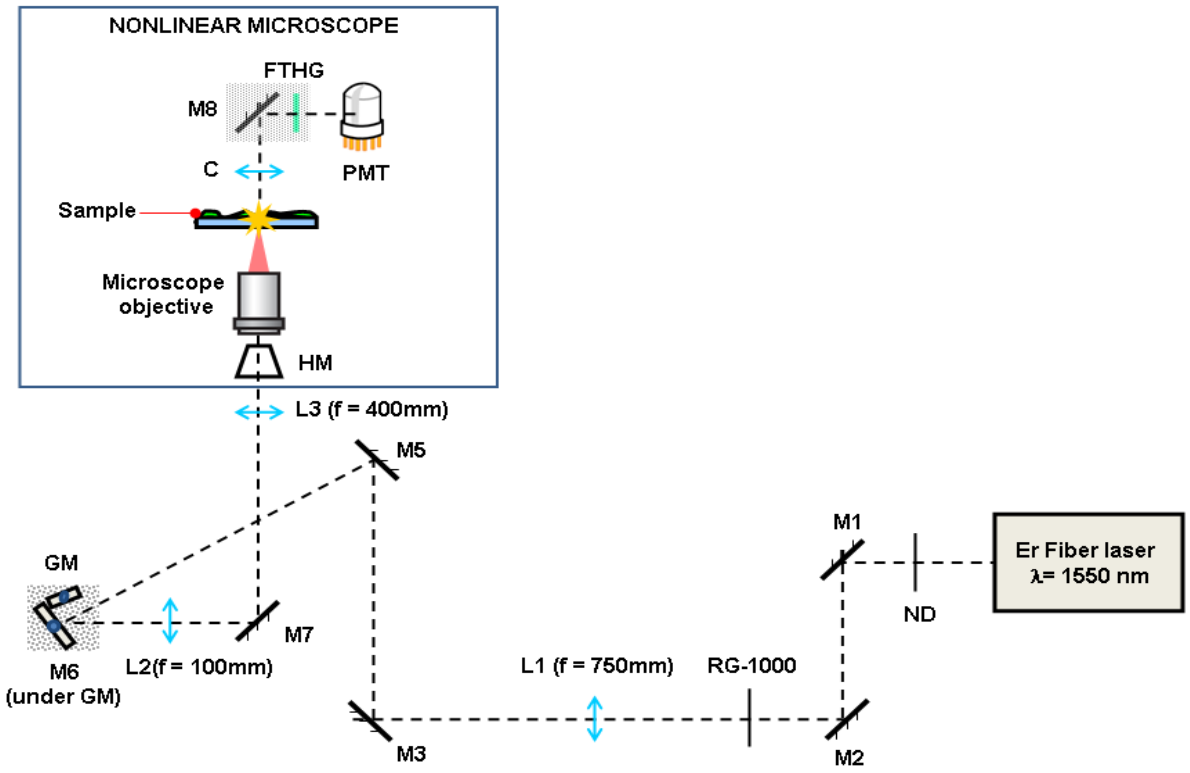

Figure: 2.1. Schematic of the real experimental setup used for third-harmonic generation. Er Fiber laser is the FemtoFiber FFS laser at 1550 nm; ND, neutral density filter; M#, mirrors; RG-1000, bandpass filter; L#, lenses; GM, galvanometric mirrors; HM, dichroic mirror; C, condenser (NA=1.4); FTHG, bandpass filters (transmittance=512–521 nm); and PMT, photomultiplier tube.

To make sure that the nonlinear effect is in fact THG, a series of tests were carried directly at the sample pane. A test sample consisting of a starch and water interface sandwiched between two cover-glasses was prepared. To obtain the spectrum traces the sample was placed into the microscope and it was then excited using the above mentioned laser. The spectrum was then collected using the designed forward mount, which also enabled fiber coupling. This was then connected into a spectrometer (Avantes, USB2000 and IST E202LSA03A). For the fundamental excitation beam, the spectrum was collected without employing any filter. For the THG signal, the appropriate filters (previously described) were employed to record its spectrum. Figure 2.2 shows the normalized spectral traces.

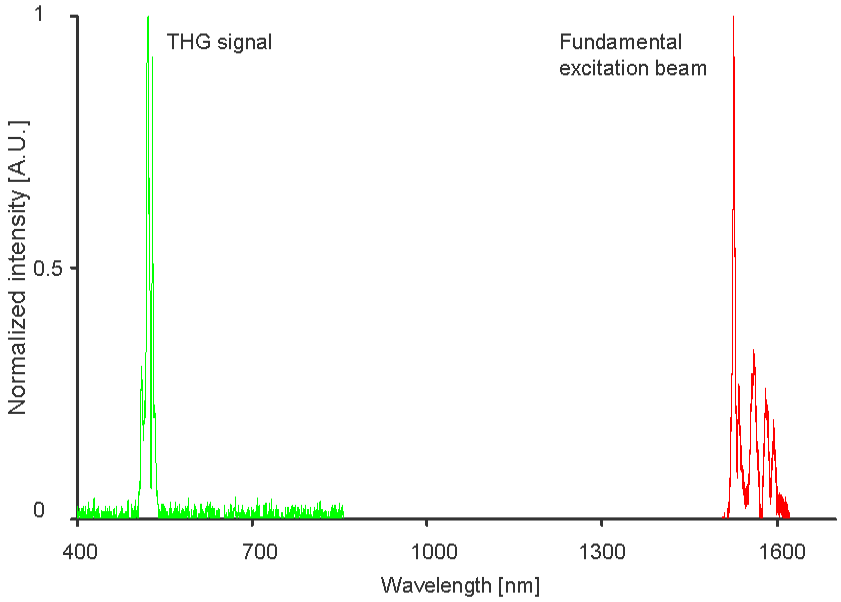

Figure: 2.2. Normalized spectrum traces from the fundamental excitation beam (erbium fiber based pulsed laser system) and corresponding THG signal.

From figure 2.2 it is evident that the generated signal corresponds to a THG signal. This was verified by observing each peak from the fundamental excitation beam and their corresponding THG counter parts. These peaks were approximately 1535 nm, 1561 nm and 1580 nm and their corresponding THG signals were 510 nm, 521 nm and 528 nm. The slight difference between the obtained data could be attributed due to the fact that 2 different spectrometers were employed as the ones available in the lab do not cover the full spectral range, having slight differences in their calibration.

Importantly, the emitted THG signal will be located within the visible range (~516 nm), eliminating the requirement of specialized optics (ultra violet grade) to collect such signal. In addition, most of the detectors (including the employed one in this work) have their peak sensitivity within this wavelength range. The benefit of employing this wavelength for imaging is that very low average powers are required and no signal amplification schemes are needed to image the sample. In addition as THG is a label-free imaging technique, this will eliminate sample preparation, thus minimizing side effects that could be produced to it. This will be demonstrated firstly by presenting THG images of several samples and then by performing a comparison with another THG microscope operating at 1028 nm. Finally, long-term time-lapse imaging of unlabeled *C. elegans* morphogenesis process is demonstrated.

As a first demonstration of the NLM workstation capabilities different samples (starch granules) including *in vivo* model organisms such as, *Danio rerio* embryos, *drosophila melanogaster* embryos *Caenorhabditis elegans* (*C. elegans*) were imaged (see appendix A 1.5 for mounting procedures).

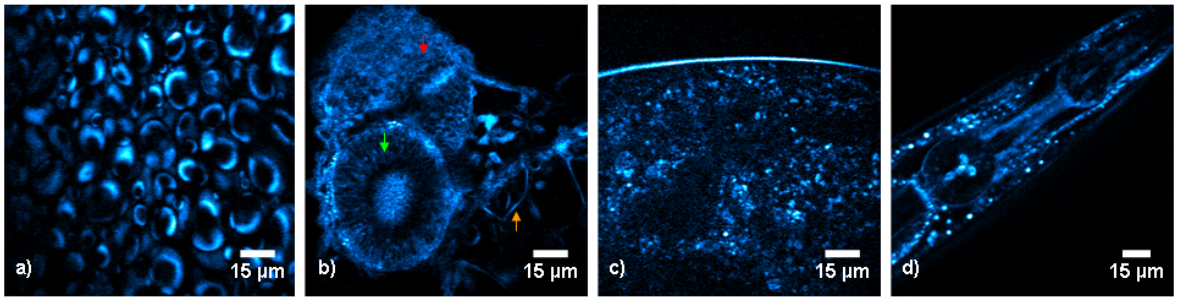

Figure: 2.3. THG images obtained using the developed work station. a) starch granules, b) *Danio reiro* embryo eye, brain and yolk region, c) *drosophila melanogaster* embryo yolk region, and d) *C. elegans* nematode pharyngeal region. THG signal is depicted in blue.

Figure 2.3 shows how the interfaces give a rise to the THG signal. For the case of starch granules the signal is obtained in the region where an interface is formed between the water and the starch molecule, highlighting its perimeter. For more complex organisms that are composed of numerous features having different compositions, several structures can be outlined. For the case of *Danio rerio* embryo the membranes forming the yolk region can be observed in the bottom right corner of figure 2.3b (orange arrow). In addition to this, the eye together with the brain region can be clearly identified (green and red arrows respectively). In the case of figure 2.3c a *drosophila melanogaster* embryo was imaged, here the outer membrane surrounding the yolk region can be observed. Finally in figure 2.3d a *C. elegans* nematode was imaged in the head area where the pharyngeal lobes together with a portion of the intestine region can be observed. The signal was obtained from hypodermis, lipid depositions in the intestine region, sub-cellular organelles, inclusions, cavities, pharyngeal epithelium, boundaries in the pharyngeal muscles etc. The main benefit of this technique relies on the fact that wild type samples can be imaged without the requirement of using any external marker.

To demonstrate the benefits of employing 1550 nm, a performance comparison of the developed system was carried out versus a THG microscope operating at 1028 nm [3, 4]. Table 2.2 summarizes both system capabilities.

Table 2.2. THG microscope comparison.

Laser system	Excitation / Collection NA	λ [nm]	Δτ [fs]	Avg. power [mW]	Peak power [kW]	Intensity [W/cm^2]
T-pulse (Amplitude systems)	0.8/1.4	1028	200	35	3.5	1.88E+10
Femto Fiber FFS (Toptica Photonics)	1.3/1.4	1550	100	4.9	0.45	3.05E+9

As it can be observed from table 2.2, the generated THG signal of the employed lasers is emitted at 340 nm for the case of the T-pulse laser system and around 516 nm for the case of the femto fiber FFS system. The first system emits a THG signal near the ultra violet (UV) region.

This requires changing the conventional optics to UV grade, to avoid the absorption of emitted signal by the same optical elements. Moreover, although the intensity at the sample plane in the 1028 nm microscope was six times greater compared to the 1550 nm THG microscope, a lock-in amplification scheme was required due to the detector efficiency at the emitted wavelength. In contrast to this, the system here described benefits from the fact that the generated signal falls within the peak sensitivity of most of the commercially available detectors. This enables to reduce the amount of power required to image the sample (i.e. less intensity), thus helping to minimizing sample damage effects.

Both systems were employed to image *C.elegans* embryos at cell division stage (see appendix A 1.7 for mounting procedures). The obtained images revealed that a dark nucleus can be identified from its surroundings. In addition, the limiting boundary or cell membrane of each cell can be identified [3, 4]. The fact that the two different microscopy setups give the same qualitative information indicates, as expected, that this method is intrinsic to the THG nature and not to the particular experimental set up or laser wavelength used. This study suggests that THG can be used for cell tracking studies in embryogenesis, helping to minimize the complexity of the currently used methodologies. This can be achieved without using any fluorescent marker, at very high resolution and increasing, at the same time, sample viability during imaging.

Based on the obtained results, the use of the developed NLM work station to follow the embryogenesis/ morphogenesis processes in living samples will be demonstrated.

2.2.1. Morphological studies on living *C. elegans* nematodes.

In embryology, there have been several works that have attempted to track morphogenesis. Such works have used a combination of differential interference contrast (DIC)/Nomarski and fluorescence microscopy [5-10]. As it has been explained before, in DIC microscopy contrast that is generated from the encoded phases inside the sample but it lacks from being specific to structures and it possesses limited axial resolution [11, 12]. However, if the development of a specific structure needs to be recorded individually other techniques, such as fluorescence microscopy, have to be used [13]. In such a case, the use of fluorescent markers or vital dyes endogenously expressed is required for a selective observation. This has, however, time, technical and sample viability limitations besides the inability to produce high resolution three-dimensional (3D) images [14].

Alternative works have proposed the use of confocal laser scanning microscopy (CLSM) to overcome the limitations of the previous methodologies. This has enabled to compare wild

type organisms, study a large number of existent mutant alleles, and transgenic reporter strains. In addition CLSM has also been used to perform lineage analysis and recordings of embryogenesis in living *C. elegans* [15]. However, this technique requires the use of fluorescent reporters. Moreover, as a linear excitation scheme is used, care should be taken to minimize photo-damage effects (i.e. photo-bleaching and photo-toxicity). In addition, the excitation power must be dynamically adjusted to allow for long-term recordings in order to reduce exposure effects on the sample [15]. As a consequence, the dim signal of the system can limit the cell/tissue identification task. Therefore, to track cells and morphological processes, the development of relatively complex algorithms is required [6, 8, and 16].

A successful implementation using two-photon Excited Fluorescence (TPEF) to perform four dimensional (4D) developmental analyses in *C. elegans* was reported by [17]. Thanks to the reduced sample damage (based on the non linear effect using excitation wavelengths in the near infra-red) it is possible to image living specimens for longer periods. However, the use of fluorescent probes is still required. To overcome these, a label-free strategy in developmental studies can be used.

Recalling what has been discussed in the introduction section; Second Harmonic Generation (SHG) and THG offer the advantage of being label-free techniques. These valuable tools have been used to study different biological samples (i.e. *Pristionchus, C. remanei and C. elegans*). The generation of SHG signal requires a non centro-symmetric structure, limiting its applicability in tissue, mainly to collagen, muscle and microtubules [18]. In contrast, for the case of THG as it has been shown before, the only requirement is to have interfaces within the sample either having variations in its refractive index or in the χ^3 nonlinear coefficient [2]. Based on this a significant THG signal is produced from lipid bodies in different samples such as *Drosophila melanogaster*, fresh mouse lung tissue, *Arabidopsis thaliana*, etc. [19-22].

To demonstrate the non invasive nature of THG microscopy and all its related advantages, images of embryogenesis/morphogenesis process of *in-vivo C. elegans* embryos will be presented. This wavelength has neither been used in living samples nor for long-term exposure experiments and, therefore, the sample viability is unknown. On one hand, UV light is not involved in the imaging process, increasing the sample viability. On the other hand, water absorption caused by the excitation wavelength starts to be important. In the following text the demonstration of THG microscopy at 1550 nm for long-term time-lapse recordings will be presented, the sample viability effects caused by the use of this wavelength will be discussed in the next subchapter. Importantly, to the best of my knowledge, this was the first time that THG imaging at this wavelength is used to obtain 4D embryogenesis/morphogenesis information of *in-vivo C. elegans* samples.

Wild type (N2) *C. elegans* embryos were used to perform the THG 4D recordings (see appendix A 1.7 for mounting procedures). This nematode was selected because it is a widely

used model organism for many different research fields. Its short life cycle, small size, transparency, invariant cell lineage, and easiness of maintenance in the lab make this model organism highly attractive for microscopy studies such as embryogenesis. The *C. elegans* nematode completes its life cycle in three and a half days at 20ºC [23]. Therefore, its development is relatively fast (once the eggs are laid). Hatching will take place in approximately 13 hours [15].

A total of 27 *C. elegans* embryos, at different developmental stages, were imaged. An emitted THG signal was observed in all the development stages as well as dynamic changes on its position and intensity along the different phases of the *C. elegans* wild type embryos. Figure 2.4 depicts all the *C. elegans* stages starting from the cell division process inside the hermaphrodite, passing through the gastrula, coma, multiple fold stages (previous to the hatching process) and the L1 larva (after the hatching process).

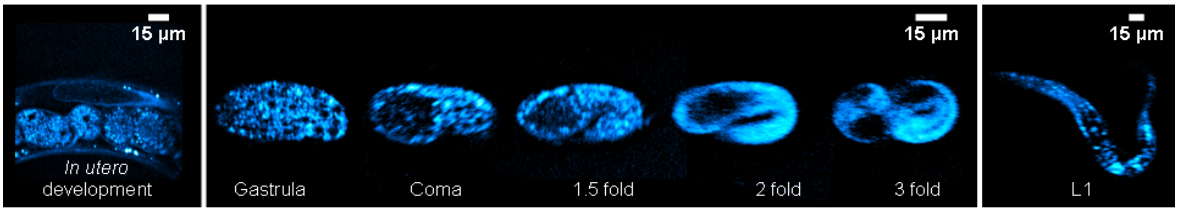

Figure: 2.4. THG signal from all the *C. elegans* developmental stages during the morphogenesis process. The THG signal is depicted in blue

At the early development stages the emitted signal was generated from the individual cells (see figure 2.5). In later development stages occurring between the coma and the two-fold stages (see figure 2.6) the nerve and muscle cells start differentiating. At this stage the embryo begins to move inside the egg. In this case, the signal arose mainly from the outer layers of the embryo becoming more restricted to tissues/structures. In what follows the different developmental stages of the embryos starting from the cell division stage will be explained.

Figure 2.5 shows different embryos at the cell division stage (i.e. before gastrulation occurs). The emitted THG signal was observed in all the embryo cells (having the nuclei as a dark region due its homogeneous nature) thus, every cell can be outlined as being the precursor from different structures/tissues. During these stages the cells contain lipid and carbohydrates depositions (i.e. vacuoles shown in bright yellow spots) which are internal storages that allow the embryos development in the absence of external sources of energy. Thanks to these depositions, the embryos are able to complete the morphogenesis/embryogenesis process. These lipid depositions have already being suggested to give rise to the THG signal [19, 20, 21, 22].

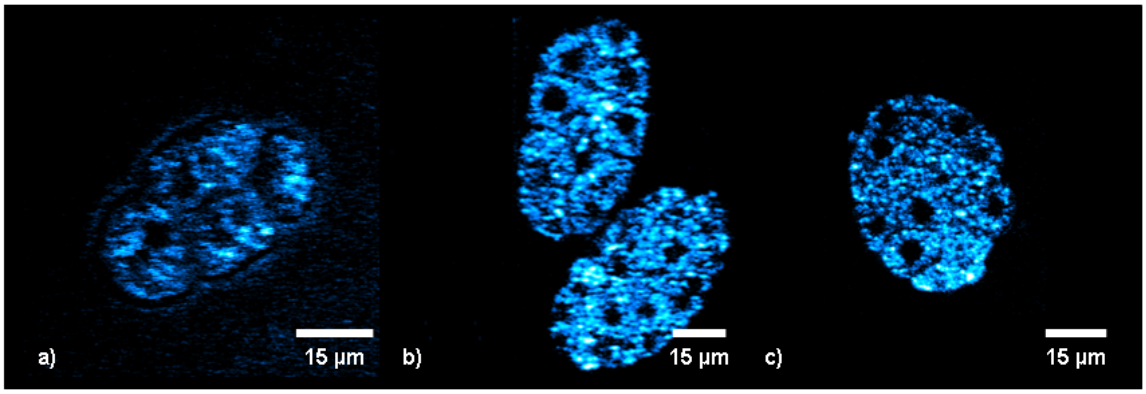

Figure: 2.5. Images of THG signal from *C. elegans* embryos at the early stages of development. These images show identifiable dividing cells and nuclei (black circles inside delimited cells). The images depict a) four cell stage egg, b) and c) multiple cell stage eggs. THG signal is depicted in blue.

In figure 2.6 a group of embryos at different developmental stages is shown. These were subjected to a 2D time-lapse recording (10 images were taken to improve the signal-to-noise ratio; the background of the image is due to the M9 medium buffer-glass interface [24]). At the beginning of this time-lapse experiment, the acquired images allowed to easily classify the embryos in two groups. These are, the earlier developed (before ventral enclosure), such as embryos labeled with "a" and "b", and late developed (after ventral enclosure took place), embryos labeled with "c" to "f".

In this set of images part of the *C. elegans* embryos elongation process can be followed. For example, this can be observed in the one-fold embryo depicted in figure 2.6 as "a" (strategically positioned ventrally). Additionally, in the more developed embryos "c" to "f", this process could also be followed regardless of the intense movement restrictions imposed by the two and three-fold stage embryos.

Moving forward in the developmental stages (embryo depicted as "f" in figure 2.6, which is at the two-fold stage) the observed THG signal arose from a more superficial section of the embryo. This signal might be generated by tissues that could be hypodermal cells (skin cells, ectoderm etc.), or even resulting from body wall muscles. Finally, for the more developed embryos (three-fold embryos: "c", "d" and "e") it was also observable an increased intensity signal at the outer portion of the embryo. This could possibly be attributed to the cuticle formation.

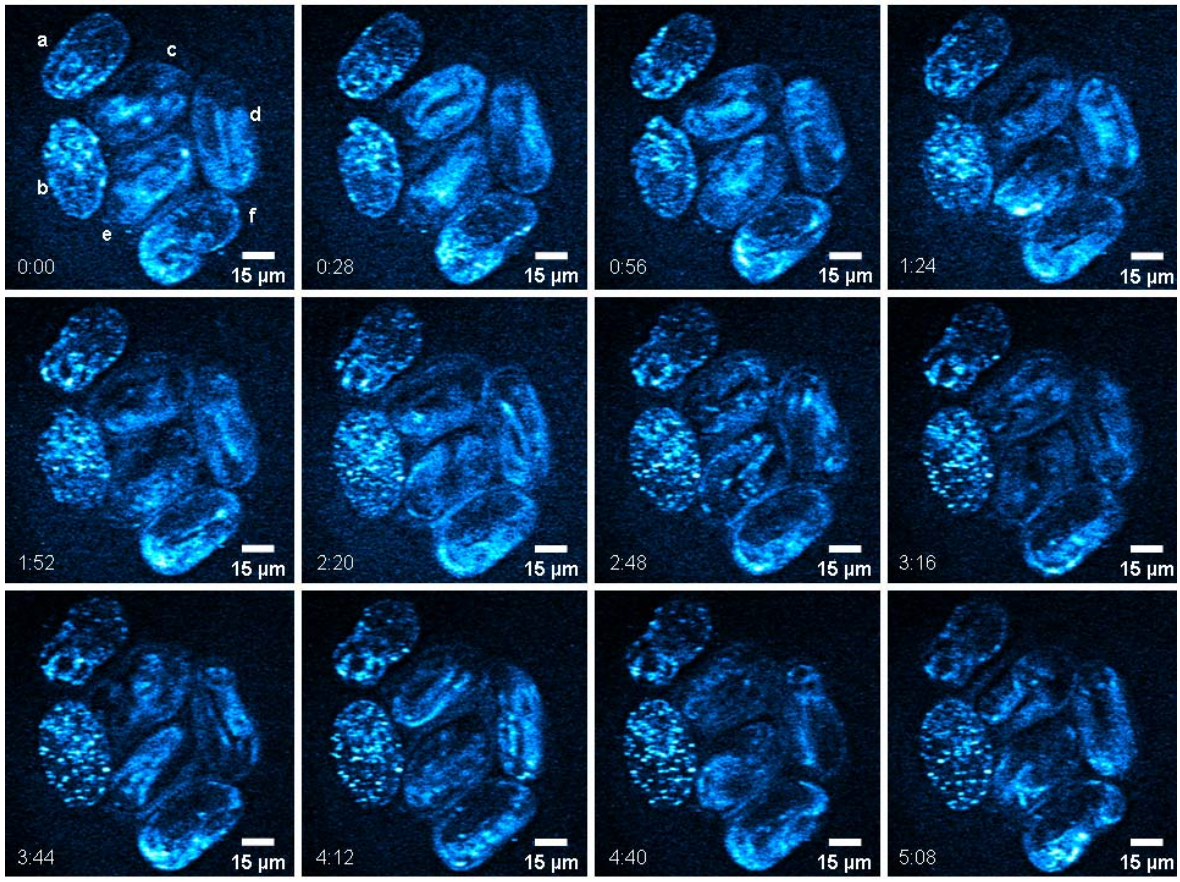

Figure: 2.6. Single frames from a video recording of THG signal in a 2D reconstruction of six *C. elegans* embryos at different developmental stages. "a" and "b" are earlier developed (before ventral enclosure occurs); "c" to "f" are late developed (after ventral enclosure takes place). THG signal is depicted in blue. Each frame is composed of 10 scans to improve the signal-to-noise ratio. The sample was imaged up to 5 hours and the time between images is 28 minutes. The shadow below the image is due to the M9 buffer-glass interface.

To illustrate these events an embryo at the ventral closure and elongation stage was imaged to specifically visualize such event. A detailed description of these structural changes will be discussed. This will be followed by a discussion of the imaging capabilities of the developed system.

Morphogenesis of the *C. elegans* is mainly controlled by the development of epidermis, which involves cell interactions with tissues. This process is dramatic in terms of speed, and the changes that occur in the embryos shape, taking place in a period of 5 hours [25]. Paying special attention to dynamic processes, in figure 2.7 the morphological changes occurring in the later developed embryos such as ventral closure, and elongation can be observed.

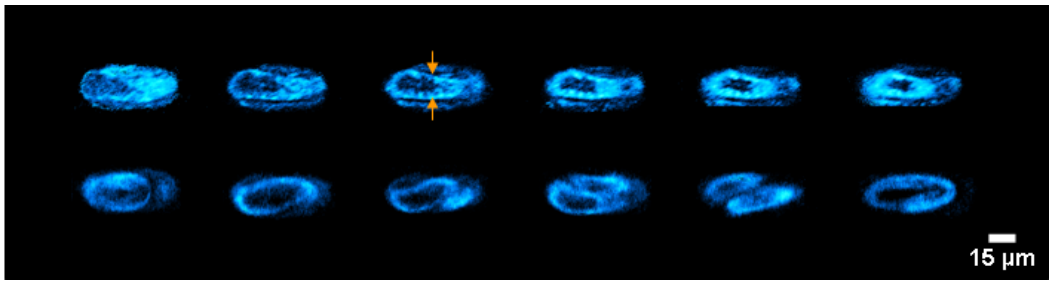

Figure: 2.7. THG signal from an embryo at the ventral closure and elongation stages. The total recording time was five hours; each frame was taken every 5 minutes. The time between images is 25 minutes.

The recorded THG signal provides valuable information of the specimen at the different development stages. In the top row of figure 2.7 (orange arrows) the enlargement of the two rows of epidermal cells coming closer to each other towards forming a single row at the ventral mid line can be observed. This process is known as the dorsal intercalation, which begins after cells have differentiated into epidermal precursors. This process has already been recorded by [26] using green fluorescent protein reporters. Importantly the use of the proposed technique enables to observe this process in a label-free fashion and in a minimally invasive way, simplifying the whole imaging procedure.

Once the dorsal closure has been successfully completed, the embryo suffers from a major morphological change known as elongation (see figure 2.7 bottom row). At his point the bean-shaped embryo actin filaments decrease and the cells correspondingly elongate along the anteroposterior axis.

After elongation has been completed, the motion of the *C. elegans* nematode is faster than the acquisition rate of the NLM workstation, as trans-epidermal attachments transmit force causing muscular contraction to the cuticular exoskeleton causing the embryo to move rapidly [27] (see figure 2.7 bottom row last three frames). The correct identification of the exact signal location source is difficult to track due to the rapid muscular movement of the embryo.

To further show the advantages of this methodology, figure 2.8 is a volume rendered model of a *C. elegans* sample (rotated for a perspective view). To create the 3D reconstruction of the nematodes, a series of optical sections separated 1-1.3 µm apart were acquired. The choice of this parameter was based on the theoretical point spread function axial resolution calculation (resulting value of 1.3 µm) [28]. For each specimen, an average of 24 stacks were taken (eggs had an average size of 60x30x30 µm). For each optical section 10 frame (500x500 pixels) scans were performed and subsequently averaged in order to improve the signal-to-noise ratio (SNR). Each scan took about 2 seconds to complete. To acquire the whole 3D image the exposure time was optimized to 15 minutes. By making these considerations adequate signal was obtained while having minimized sample exposure. This

was required as no reference for the stress induced to the embryo or of sample deterioration at this specific wavelength is known.

The 3D reconstruction of the studied sample enables locating the real position of the cells and structures evolution in this specimen. In this figure, the 3D time-lapse model enables to follow the morphological evolution of five embryos ("a" and "b" earlier developed, "c" to "e" late developed). In embryos "a" and "b", the THG signal arose from the inner spots. These THG sources had a flashing behavior during the different recorded time points. These strong flashing signals could be caused by the programmed cell deaths, migrations, fusions, or due to the loss of membrane integrity. All these processes occur particularly during the morphogenesis process. Additionally, as previously shown on figures 2.6 and 2.7, this 3D model also aids to easily identify the elongation process occurring in embryos "c" to "e". However, it is worth mentioning that during two-fold and three-fold stages, the cuticle synthesis begins in the elongation process. As observed on figure 2.7, the embryos start to move rapidly and this method is able to record this movement. However, as before, the scanning speed of the galvanometric mirrors (~300 Hz) imposed a time resolution restriction, limiting the ability of obtaining a full 4D model reconstruction.

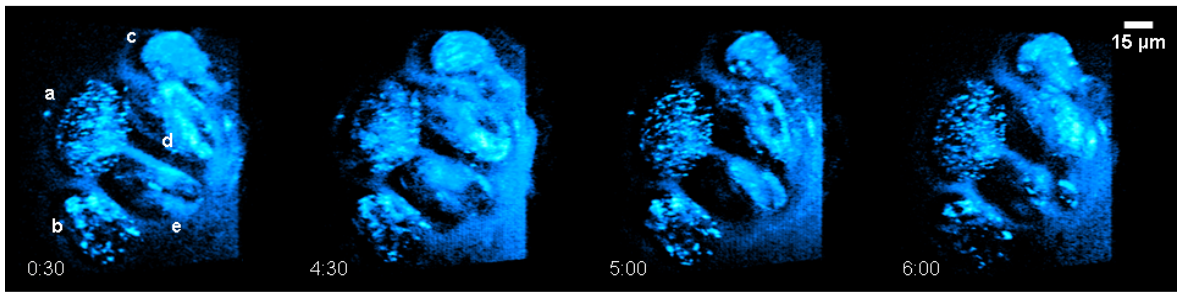

Figure: 2.8. 3D reconstructions of THG signal (rotated for a perspective view) from five living *C. elegans* embryos at different developmental stages. The images were taken every 30 minutes (depicted times are 0.5, 4.5, 5 and 6 hours, respectively). The sample was imaged for 6 hours. THG signal is depicted in blue. The shadow below the image is due to the M9 buffer-glass interface.

For detailed studies, the samples could be imaged at lower temperatures as it has been reported that at 15°C, the embryos development is 1.5 times slower than at 20°C [23]. In this case specialized microscope temperature controls must be implemented. Alternatively, an optimized scanning strategy could be implemented to enable faster scanning rates. To achieve this, several aspects should be taken into account such as, minimization of aberrations [22, 29] the use of objectives optimized for such long wavelengths for extracting more THG signal (based on their commercial availability), or employing a laser system having an increased repetition rate (>100 MHz). Once these considerations are met other scanning configurations could be used to speed up the frame acquisition rate such as acousto-optical deflectors [30] or a polygonal mirror [31].

By close observation of figures 2.4-2.8 it is clear that the THG signal has the potential to provide a great amount of information occurring during the *C. elegans* morphogenesis process.

One of the potential applications of THG microscopy is cell tracking at early cell division stages. This is currently done with either DIC or fluorescence microscopy [9]. Consequently, tracking the cell division process is based on the image smoothness differences [13] (i.e. the texture of the cytoplasm and spindles) therefore complex algorithms must be used. However, based on these results, the cell nucleus (at earlier stages) being an homogeneous structure does not produce third harmonic signal (in contrast with some surrounding structures). As a consequence, the presented images show that this structure is extremely clear and delimited (see figure 2.5). All the above indicates that the presented technique has the potential to be used as an aiding tool in cell tracking when no fluorescent markers are available or desired for any particular reason. This type of information is relevant for cell lineage studies where these are tracked to determine which cells are precursors of different tissues. Importantly, this technique could be used to provide enough information to easily identify the imaged structures without having to employ the previously mentioned complex image analysis algorithms to track the development of each structure.

For the more developed *C. elegans* embryos, epidermal morphogenesis is a process that could be potentially followed employing the here proposed technique.

Note that a frequency-doubled version of the same fiber laser source could be used for a multimodal microscopy approach, allowing the simultaneous implementation of other techniques such as TPEF [32], SHG, [19-21, 33-35] etc. Adding these techniques will comprise an improved and supporting tool that would provide complementary information useful to investigate the sources of the THG signal.

2.3. Long-term imaging effects of longer wavelengths in living samples

In this subchapter, an evaluation of the effects induced by 1550 nm for continuous sample imaging was assessed. Before proceeding with the experiments, a power absorption approximation based on using Beer's law to estimate the temperature raise at the focal plane of a microscope in optical trapping applications was used. The calculation is based on the power absorbed by a test sample (two cover-glasses sandwiching a drop of water) at a given wavelength. This model can be applied to biological samples as these are mainly constituted of liquids that may behave similarly to water [36]. This was done as it is known that 1550 nm has an increased water absorption coefficient causing a temperature increase at the sample plane [37].

For the calculation, a reference wavelength (980 nm) having a reduced water absorption coefficient was employed. The Lambert absorption coefficients for 980 nm and 1550 nm are

0.5 cm^{-1} and 9.6 cm^{-1} respectively. However, imaging follows from the rapid heat diffusion inside biological tissues due to beam scanning [38]. For this calculation, the power absorbed at each wavelength was calculated considering the employed power at the sample plane (~4.9 mW) together with the dwell time (i.e. the time spent by the laser in a single point of the sample is ~ 6.6 μs for this particular study). Employing the parameters from the experiment, it results that the sample will experience a temperature raise of 0.016 ºC at each point when 1550 nm is used, in contrast with this, the temperature raise for 980 nm will be 0.002 ºC. Based on this approximation it can be observed that the temperature increase will be eight times more when using 1550 nm compared to 980 nm. These calculations were employed to have an estimation of sample heating compared to other wavelengths. However, the effects of 1550 nm exposure on a real sample must be experimentally studied. For this purpose several imaging trials were conducted to fully assess the use of this specific wavelength as it has never been used for long-term imaging experiments.

For the sample viability experiments, control dishes containing non-irradiated *C. elegans* eggs were used to take into account other constraints that might prevent the embryos from a normal development. The survival rate for a total of 416 unexposed embryos was 89%.

The survival rates of the embryos after long-term imaging exposure were studied. These rates were strongly dependent on the actual embryo development stage and the beginning of the time-lapse experiments. Thus, several long-term exposure trials evaluating embryos survival rates were performed. The samples were imaged for several hours and afterwards left unexposed for another period of time to be able to hatch.

Based on the obtained results and the *C. elegans* nematode development cycle, the specimen behavior was classified into two main groups: Embryos before two-fold stage and embryos after two-fold stage. On one hand, the embryos before two-fold had a survival rate of 41% (compared to the control sample). During the first hours, these embryos presented a normal development. Morphological processes such as, gastrulation, cell migration and fusion were recorded. However, in some cases, after long-term sample exposition there was a slight slow down on its development. A possible cause for this performance could be that during this stage the embryo lacks of developed tissue (i.e. hypodermic/ectodermic) making the differentiating cells more vulnerable to this kind of radiation (see figure 2.9) .

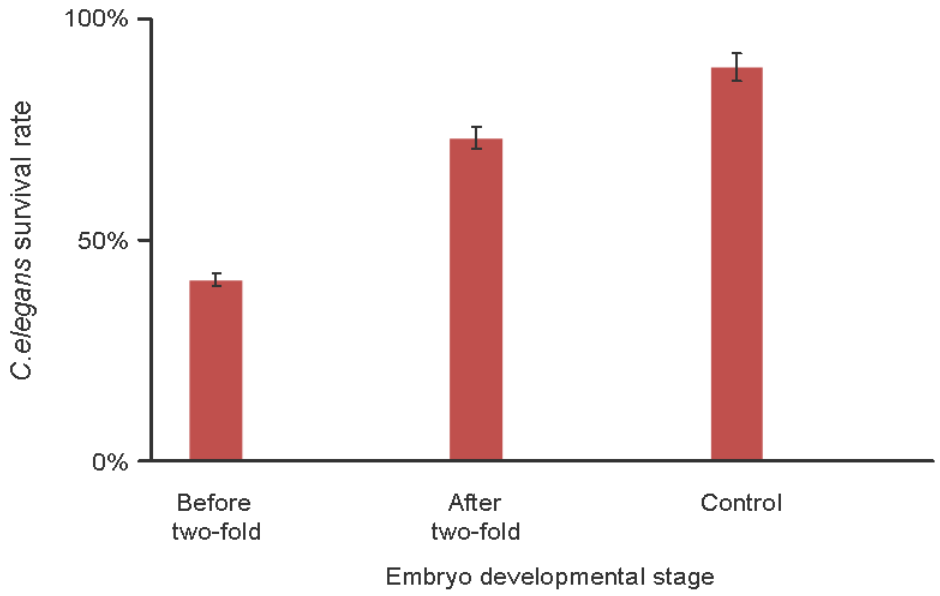

Figure: 2.9. Survival rates of *C. elegans* embryos after long-term imaging versus non laser radiated control samples. The reported margin of error is typically about twice the standard deviation.

On the other hand, and contrary to the less developed embryos, the two-fold and three-fold stage embryos had a survival rate of 73% (compared to the control sample). This was confirmed as the more developed embryos presented a continuous muscular movement during the whole imaging process. In these experiments the embryos presented a normal development without any detectable morphological defects (observable in the 2D and 3D volume rendered images of figures 2.6-2.8 respectively). After the acquisition process was finished, several hours later, the embryos were able to hatch normally.

Moreover, as previously mentioned, even when three-fold stage embryos were exposed up to 6 hours (see figures 2.6 - 2.8) they were able to hatch normally. Based on these results, a possible cause for this behavior could be that the development of structures like hypodermal/ectodermic tissue may act as a protection to IR light exposure.

Although the hatching and the viability of the embryos cannot be considered an ideal indicator for the absence of possibly induced damage with this particular wavelength, the high survival rate percentages are strong indicators of tiny inflicted embryo damage. Moreover, a close anatomical observation of the L1 larvae with DIC post 4D imaging and the integrity of anatomical and behavioral characteristics of the nematode sustain the previous statement of a minimum induced damage.

The application of 1550 nm laser wavelength *in-vivo* and, more importantly, its use for long-term 4D imaging experiments (to record developing organisms such as *C. elegans* embryos) has enormous potential. Not only because intrinsic signal from different structures inside the

embryo (employing the sample interfaces as a contrast agent) are obtained. But also, because embryogenesis/morphogenesis processes can be recorded *in-vivo*.

As previously demonstrated, this process can take several hours, however, employing this particular wavelength no apparent damage was caused to the sample. These results were not expected, because it is known that IR wavelengths above 1500 nm are associated with increased water absorption in tissue and may lead to unwanted heating of biological specimens [1]. Based on this, one might think that this wavelength cannot be used for imaging living samples, nor for long-term imaging experiments. However, in this case, and in agreement to other works [2, 19-22] the used laser is able to produce an efficient THG signal from the sample using very low average powers. All this helps reducing the expected damage. This is mainly because the generated THG signal (516 nm) falls within the peak sensitivity region of most PMTs (i.e. Hamamatsu, H9305-04 peak sensitivity at 530 nm) allowing for an efficient signal collection. Another important and practical issue is that by using this wavelength, there is no requirement to use specialized collection optics (as it is the case when conventional Ti:Sapphire lasers are used). Therefore, the obtained results have demonstrated that this wavelength is suitable to perform 4D imaging in living *C. elegans* samples and even in one of the most sensitive stages of its life, such as morphogenesis/embryogenesis.

2.4. Summary

A THG microcopy work station was developed to work at 1550 nm for long-term time-lapse imaging studies. This device was designed using a state of the art telecommunications ultra-short pulsed laser system to simplify its integration into NLM. At the same time, this offers the advantage of having a signal within the visible range to minimize sample damage effects, thus offering alternatives to overcome the difficulties found in developmental imaging.

According to the research conducted in this field, this is the first time that this wavelength is applied for THG imaging to perform morphogenesis/embryogenesis studies in living *C. elegans* embryos. It has been demonstrated that using 1550 nm wavelength it is possible to track *in-vivo* morphological processes for several hours without altering the anatomical and behavioral characteristics of the sample.

This simplifies the procedure required to perform typical 4D imaging as this is a label-free technique. Therefore, this will aid reducing the complexity of sample preparation, as well as the interference with the specimen.

THG microscopy provides the exact spatial localization of individual cells and tissue thanks to its optical sectioning capability. Importantly, its enhanced resolution enables to easily identify individual cells, and different structures present in the whole development cycle of the *C. elegans* nematode. Therefore, it could be used to track the cells position and divisions

during the morphological process opening the possibility to apply this methodology in cell lineage studies and/or epidermal morphogenesis studies.

The observation of morphological processes occurring after gastrulation such as ventral closure and elongation was recorded in a non invasive way always keeping in mind the minimization of sample damage and interference effects

An important aspect that still needs to be investigated is the identification of every structure in all the development stages of the *C. elegans* embryos which is certainly a challenging future work. This task requires knowledge and time to label each structure to be imaged to perform co-localization studies. Once the THG signal sources (in all the embryo developmental stages and in the larvae) are identified, the requirement of using reporters expressed in different cell types to track these developmental processes could be over passed. Then, the use of this technique, and this particular wavelength, could be used as a non-invasive technique to study different dynamic processes such as the development of certain cell/tissue precursors.

It is important to keep in mind that the main goal of this thesis is to provide the end users with the tools to perform this task and at the same time to push NLM towards its limits rather than performing complete specimen structures co-localization. To do so it should always be taken into account the laser exposure effects on the sample. Therefore a laser system being able to fulfill these requirements is essential to aid such an important task. As the procedure involves the use of fluorescent markers (only for identification purposes) an ultra-short pulsed laser system being able to image samples efficiently without employing large amounts of average and peak power is therefore required. The use of other fiber based laser systems or any other novel technologies for this purpose will enable a simpler implementation on NLM if these are compact, robust and inexpensive.

Another important challenge that still needs to be addressed is the requirement of an optimized scanning strategy. For this purpose and as it was discussed on section 2.2 several paths can be taken. The main goal is to scan faster without having to increase the amount of power applied to the sample, as it would result in a temperature increase. A possible way to solve this would consist on having a laser system operating at higher repetition rates (i.e. >100MHz). In such case, the mean power of the emitted signal is enhanced by increasing the number of pulses per second, while maintaining the same pulse energy and peak intensity. This could potentially allow for an improvement in signal intensity and consequently a faster and better detection, while avoiding nonlinear photo-damage. This enhancement in detection also affords some potential for real-time imaging, as the pixel dwelling time can be reduced to collect the same number of photons (as compared to the low-repetition rate case), thus reducing the acquisition time per frame.

An additional aspect to keep in mind is that developmental studies require imaging at different depths for assembling a 3D model. Aberration effects can decrease the intensity of the confined focal volume as imaging is performed deeper inside the sample. To address this it would be beneficial to restore the spatial intensity confinement to have a more efficient nonlinear effect without having to apply additional average power as imaging is carried out deep inside the sample. In this way the scanning speed could be also increased and at the same time the diffraction limited performance of the NLM could be preserved at different imaging depths. This represents a major challenge as it requires the full development of a strategy to be implemented into the existing imaging platform. The implementation of a strategy to correct for sample induced aberrations will be presented on chapter 4.

References

1. Yelin, D. Oron, E. Korkotian, M. Segal, and Y. Silbergerg, "Third-harmonic microscopy with a titanium-sapphire laser," Applied Physics B-Lasers and Optics 74, S97-S101 (2002).

2. A. C. Millard, P. W. Wiseman, D. N. Fittinghoff, K. R. Wilson, J. A. Squier, and M. Muller, "Third-harmonic generation microscopy by use of a compact, femtosecond fiber laser source," Applied Optics 38, 7393-7397 (1999).

3. R. Aviles-Espinosa, G. J. Tserevelakis, S. I. C. O. Santos, G. Filippidis, A. J. Krmpot, M. Vlachos, N. Tavernarakis, A. Brodschelm, W. Kaenders, D. Artigas, P. Loza-Alvarez, "Cell division stage in C.elegans imaged using third-harmonic generation microscopy," in Proc. Biomedical Optics, Optical Society of America, Wasington,D.C., paper. BTuD78 (2010).

4. R. Aviles-Espinosa, S. Santos, A. Brodschelm, W. G. Kaenders, C. Alonso-Ortega, D. Artigas, and P. Loza-Alvarez, "Third-harmonic generation for the study of Caenorhabditis elegans embryogenesis," Journal of Biomedical Optics 15 (2010).

5. M. F. Portereiko, and S. E. Mango, "Early morphogenesis of the Caenorhabditis elegans pharynx," Developmental Biology 233 (2001).

6. J. Hench, J. Henriksson, M. Luppert, and T. R. Burglin, "Spatio-temporal reference model of Caenorhabditis elegans embryogenesis with cell contact maps," Developmental Biology 333, 1-13 (2009).

7. R. Schnabel, M. Bischoff, A. Hintze, A. K. Schulz, A. Hejnol, H. Meinhardt, and H. Hutter, "Global cell sorting in the C-elegans embryo defines a new mechanism for pattern formation," Developmental Biology 294 (2006).

8. R. Schnabel, H. Hutter, D. Moerman, and H. Schnabel, "Assessing normal embryogenesis in Caenorhabditis elegans using a 4D microscope: Variability of development and regional specification," Developmental Biology 184 (1997).

9. Thomas, P. DeVries, J. Hardin, and J. White, "Four-dimensional imaging: Computer visualization of 3D movements in living specimens," Science 273 (1996).

10. J. E. Sulston, E. Schierenberg, J. G. White, and J. N. Thomson, "The embryonic-cell lineage of the nematode caenorhabditis-elegans," Developmental Biology 100, 64-119 (1983).

11. B. R. Masters, “Techniques that provide contrast,” Chapter 5 in Confocal Microscopy and Multiphoton Excitation Microscopy: The Genesis of Live Cell Imaging, pp. 55–64, SPIE Press, Bellingham, WA (2006).

12. M. Oheim, D. J. Michael, M. Geisbauer, D. Madsen, and R. H. Chow, "Principles of two-photon excitation fluorescence microscopy and other nonlinear imaging approaches," Advanced Drug Delivery Reviews 58, 788-808 (2006).

13. S. Hamahashi, and S. Onami, "Objective measurement of spindle orientation in early Caenorhabditis elegans embryo," Genome informatics. International Conference on Genome Informatics 16 (2005).

14. J. T. Yasuda, H. Bannai, S. Onami, S. Miyano, and H. Kitano, “Toward automatic construction of cell-lineage of C. elegans from Nomarski DIC microscope images,” Genome informatics 10, 144–165 (1999).

15. Z. R. Bao, J. I. Murray, T. Boyle, S. L. Ooi, M. J. Sandel, and R. H. Waterston, "Automated cell lineage tracing in Caenorhabditis elegans," Proceedings of the National Academy of Sciences of the United States of America 103, 2707-2712 (2006).

16. S. Hamahashi, S. Onami, and H. Kitano, "Detection of nuclei in 4D Nomarski DIC microscope images of early Caenorhabditis elegans embryos using local image entropy and object tracking," Bmc Bioinformatics 6 (2005).

17. W. A. Mohler, and J. G. White, "Multiphoton laser scanning microscopy for four-dimensional analysis of Caenorhabditis elegans embryonic development," Optics Express 3, 325-331 (1998).

18. L. Moreaux, O. Sandre, M. Blanchard-Desce, and J. Mertz, "Membrane imaging by simultaneous second-harmonic generation and two-photon microscopy," Optics Letters 25, 320-322 (2000).

19. W. Supatto, D. Debarre, B. Moulia, E. Brouzes, J. L. Martin, E. Farge, and E. Beaurepaire, "In vivo modulation of morphogenetic movements in Drosophila embryos with femtosecond laser pulses," Proceedings of the National Academy of Sciences of the United States of America 102, 1047-1052 (2005).

20. D. Debarre, W. Supatto, E. Farge, B. Moulia, M. C. Schanne-Klein, and E. Beaurepaire, "Velocimetric third-harmonic generation microscopy: micrometer-scale quantification of morphogenetic movements in unstained embryos," Optics Letters 29, 2881-2883 (2004).

21. D. Debarre, W. Supatto, A. M. Pena, A. Fabre, T. Tordjmann, L. Combettes, M. C. Schanne-Klein, and E. Beaurepaire, "Imaging lipid bodies in cells and tissues using third-harmonic generation microscopy," Nature Methods 3, 47-53 (2006).

22. Jesacher, A. Thayil, K. Grieve, D. Debarre, T. Watanabe, T. Wilson, S. Srinivas, and M. Booth, "Adaptive harmonic generation microscopy of mammalian embryos," Optics Letters 34, 3154-3156 (2009).

23. I. A. Hope, “The genome project and sequence homology to other species,” Chapter 2 in C. Elegans; A Practical Approach, pp. 17–33, Oxford University Press, Oxford, New York (1999).

24. P. Török and F. Kao, “Parametric nonlinear optical techniques in microscopy,” Chapter 8 in Optical Imaging and Microscopy, pp. 197–214, Springer Series, Berlin–Heidelberg (2003).

25. J. S. Simske, and J. Hardin, "Getting into shape: epidermal morphogenesis in Caenorhabditis elegans embryos," Bioessays 23, 12-23 (2001).

26. P. J. Heid, W. B. Raich, R. Smith, W. A. Mohler, K. Simokat, S. B. Gendreau, J. H. Rothman, and J. Hardin, "The zinc finger protein DIE-1 is required for late events during epithelial cell rearrangement in C-elegans," Developmental Biology 236, 165-180 (2001).

27. J. R. Priess, and D. I. Hirsh, "Caenorhabditis-elegans morphogenesis - the role of the cytoskeleton in elongation of the embryo," Developmental Biology 117, 156-173 (1986).

28. W. R. Zipfel, R. M. Williams, and W. W. Webb, "Nonlinear magic: multiphoton microscopy in the biosciences," Nature Biotechnology 21, 1368-1376 (2003).

29. R. Aviles-Espinosa, J. Andilla, R. Porcar-Guezenec, O. E. Olarte, M. Nieto, X. Levecq, D. Artigas, and P. Loza-Alvarez, "Measurement and correction of in vivo sample aberrations employing a nonlinear guide-star in two-photon excited fluorescence microscopy," Biomedical Optics Express 2, 3135-3149 (2011).

30. Y. Kremer, J. F. Leger, R. Lapole, N. Honnorat, Y. Candela, S. Dieudonne, and L. Bourdieu, "A spatio-temporally compensated acousto-optic scanner for two-photon microscopy providing large field of view," Optics Express 16, 10066-10076 (2008).

31. K. H. Kim, C. Buehler, and P. T. C. So, "High-speed, two-photon scanning microscope," Applied Optics 38, 6004-6009 (1999).

32. M. Mathew, S. Santos, D. Zalvidea, and P. Loza-Alvarez, "Multimodal optical workstation for simultaneous linear, nonlinear microscopy and nanomanipulation: Upgrading a commercial confocal inverted microscope," Review of Scientific Instruments 80 (2009).

33. S. Psilodimitrakopoulos, V. Petegnief, G. Soria, I. Amat-Roldan, D. Artigas, A. M. Planas, and P. Loza-Alvarez, "Estimation of the effective orientation of the SHG source in primary cortical neurons," Optics Express 17, 14418-14425 (2009).

34. S. W. Chu, S. Y. Chen, T. H. Tsai, T. M. Liu, C. Y. Lin, H. J. Tsai, and C. K. Sun, "In vivo developmental biology study using noninvasive multi-harmonic generation microscopy," Optics Express 11 (2003).

35. K. Sun, S. W. Chu, S. Y. Chen, T. H. Tsai, T. M. Liu, C. Y. Lin, and H. J. Tsai, "Higher harmonic generation microscopy for developmental biology," Journal of Structural Biology 147, 19-30 (2004).

36. S.P. Gross, “Application of optical traps in vivo,” Methods Enzymol 361, 162-174 (2003)

37. W. M. Irvine and J. B. Pollack, "Infrared optical properties of water and ice spheres," Icarus, 8, 324-360, (1968).

38. D. Kobat, M. E. Durst, N. Nishimura, A. W. Wong, C. B. Schaffer, and C. Xu, "Deep tissue multiphoton microscopy using longer wavelength excitation," Optics Express 17, 13354-13364 (2009).

Chapter 3

Compact laser sources matching sample properties

In the previous chapter the use of third harmonic generation (THG), a label-free technique, was used to follow the development of living samples. As it was mentioned, this technique gives information of the boundaries inside a sample. This means that if the source of THG signal needs to be identified, other techniques such as two-photon excited fluorescence (TPEF) should be employed for this task. More over and despite the efforts of showing label-free imaging, the use of fluorescent markers is a highly common and well established practice. This requires a laser system that enables an efficient interaction of the light and the fluorescent dye inside the sample. In other words, the most efficient way to generate the highest fluorescence signal is to use the wavelength at the maximum absorption of a particular fluorophore. However, commercial laser systems have not yet been designed specifically for targeting such a specific application. The extra features of these sources are not always required for nonlinear microscopy (NLM). This increases the price, complexity and space requirements, limiting its use to research laboratories and specialized facilities.

An ideal laser source for nonlinear imaging should be able to excite several fluorophores, be cost-effective, easy to use, reliable and compact. If these conditions are met, such excitation sources could potentially replace the expensive and bulky solid-state ultra-fast laser sources. Based on these requirements, in this chapter, I will present a new family of highly efficient ultra-short pulsed laser technologies designed for targeting NLM applications. The aim of this work is to provide lasers targeting the most commonly used fluorescent markers. This would enable the full exploitation of such devices outside research laboratories, providing the end users (biologists, anatomists, clinicians etc.) with highly efficient, reliable and compact sources that in the near future could be used to replace the Ti:Sapphire (Ti:S) laser systems among others. This has the potential to mark the beginning of a new era where the use of affordable miniature (shoe box to match box sized) devices can be implemented for the design of portable instruments such as micro endoscopes, lab-on-a-chip devices etc.

All the advantages of these devices will be presented following a similar methodology as the one presented on the previous chapter. To accomplish this, the optimum laser parameters for nonlinear imaging were defined. To do so the sample properties have been considered to achieve an optimized interaction with light, specifically the case when the sample is expressing a fluorescent protein (considering the most widely used fluorescent reporters in biological research). The required laser system specifications for NLM are: Peak power ~300 W, repetition rate < 2 GHz, Pulse duration < 2ps, wavelength ~ 750-1300 nm, beam quality ~1.5 M^2.

Based on such specifications, the elements forming the compact laser systems (i.e. gain media, semiconductor saturable absorber mirrors, heat-syncs etc.) were integrated in into a prototype as part of a collaboration work. This was then followed by the implementation of such devices into the NLM work station to be characterized as part of this thesis. The obtained results in this research were used as feedback to improve the laser system performance accordingly.

In this strategy, I will start by briefly describing the state of the art commercial laser systems that have been used for NLM. Then the parameters to be modified in the design of a compact ultra-short pulsed laser (USPL) system for NLM applications will be discussed. This will be followed by caring out the compact devices implementation into the previously developed NLM workstation.

A set of tests for exhaustive testing and characterization of the USPLs to assess its full potential for nonlinear bio-imaging applications will be shown. First an optimized compact device will be presented. Then the full characterization to evaluate its full potential for several bio-imaging applications will be demonstrated. The performance of this novel laser source will be compared to one of the most widely used commercially available laser sources employed in NLM, the Ti:S laser system. The future improvements to keep pushing the technology towards an optimized performance will be described. Finally the future developments of compact USPLs will be outlined. The first demonstration of chip-sized devices for nonlinear (NL) imaging will be presented. Final remarks and future prospects to keep on pushing NLM technology towards its limits will be outlined.

3.1. Laser source design and scaling

A key element in a nonlinear microscope is the use of an USPL system. These are natural sources that are able to produce the required high intensities needed for exciting nonlinear processes. Historically, Ti:S sources have been used in NLM due to its available large peak powers along with its large tunability range. However, its complexity, high price and maintenance requirements, have limited the widespread adoption of these powerful imaging techniques into daily routine bio-imaging applications.

Efforts in the past have explored developing compact, lower-cost, and easy to use ultra-fast semiconductor saturable absorber mirrors (SESAMs) for mode-locking diode-pumped solid-state lasers [1, 2]. Compact designs can be realized by “folding” long cavities using careful mechanical design, or by increasing the repetition rate of the lasers which naturally allows short cavity lengths. However these sources have been limited by the available peak powers. More recently, compact ultrafast Cr-doped laser systems such as Cr:LiCAF, Cr:LiSAF, Cr:LiSGAF, lasers [2-4] (see Ref [2], Table. 2.1.2 for an overview on these sources) have been developed. Some of these have been employed for TPEF imaging [5-9] and although

average powers reaching 500mW have been demonstrated [4], they are often limited in their ability to sufficiently scale their average power.

Other alternative sources based on fiber lasers [10-12] and semiconductor laser diodes with amplification schemes [13-15] have also been successfully demonstrated as compact lasers for NLM applications. Fiber lasers can generate very short pulses via passive mode-locking; however, they are limited to wavelengths around 1030 nm and 1550 nm. In semiconductor lasers with amplification schemes the simplicity and compactness of such systems is compromised, as they need several stages to compress and/or amplify the pulses. Several examples can be found in literature such as a gain-switched laser source based on vertical cavity surface emitting lasers (VCSELs) [14], a gain-switched InGaAsP Distributed-Feedback-Bragg, laser diode [15] and an external cavity mode-locked laser diode consisting of multiple quantum wells (AlGaAs) [13].

One key aspect for optimizing a compact laser for TPEF, second harmonic generation (SHG) or third harmonic generation microcopy is the critical trade-off between repetition rate of the laser and the multi-photon signal strength generated [16, 17]. The signal strength in TPEF, SHG or THG imaging scales as the product of the peak power times the average power (assuming image spot size, absorption, sample, detection path, etc. remain constant). This can be used as a two-photon figure of merit (FOM2p) that allows one to make relative comparisons of laser sources as a function of their average power, pulse duration, and repetition rate (since peak power equals average power divided by repetition rate divided by pulse duration). Typical Ti:S lasers used for TPEF imaging give a peak-power-average-power product (FOM2p) of approximately 1.56 W^2 (e.g. 200 fs pulse duration, 80 MHz repetition rate, and 5 mW average power at the sample). Alternative laser sources should have a FOM2p value of a similar order of magnitude. Higher repetition rate devices allow for more compact designs, but require higher average power to achieve the same FOM2p value. This value is useful for determining if the laser source is suitable for nonlinear excitation as the detected signal level from a two-photon process is proportional to this FOM2p [18-20]. This concept was employed in this research as a way of having a single score representing the combination of all the optimum parameters to enable the interplay between these and at the same time to enable the system to be used for NL imaging applications (see figure 3.1).

In this section a strategy to address such needs is proposed, here it is demonstrated that the laser source can be designed to operate at a large set of wavelengths, well-matched to key TPEF dyes or fluorescent proteins, while maintaining its simplicity and ease of operation. The presented system was designed to match the two-photon absorption properties of one of the most widely used florescent proteins in bio-imaging research, the green fluorescent protein (GFP).

For the first time, it was experimentally demonstrated that an ultra-short pulsed semiconductor disk laser (SDL) or vertical external cavity surface emitting laser (VECSEL)

that is mode-locked by a "quantum-dot-engineered" SESAM [21] can be in fact used for nonlinear microscopy.

SDLs provide a compelling source for TPEF, SHG or THG, as they combine key features such as excellent beam quality, output power, short pulse durations, and amplitude stability. In addition, the repetition rate of these lasers can be adjusted into the 100's of MHz to 1 GHz, resulting in a compact laser cavity, but still working in a range where the FOM2p can be reasonable (compared to the standard Ti:S laser) without requiring excessively large average powers. The higher repetition rates (i.e. >100MHz) at which SDL systems can operate have the potential to be very useful for NLM applications such as SHG and THG (or any sum/difference-based frequency generation) microscopy. In such case, the mean power of the emitted SHG is enhanced by increasing the number of pulses per second, while maintaining the same pulse energy and peak intensity (below damage threshold). This will potentially allow for an improvement in signal intensity and consequently a faster and better detection, while avoiding nonlinear photo-damage (i.e. if the sample viability threshold is not over passed). This enhancement in detection also affords some potential for real-time imaging, as the pixel dwelling time can be reduced to collect the same number of photons (as compared to the low-repetition rate case), thus reducing the acquisition time per frame.

SDLs also have the potential for low-cost manufacturing, as their gain element is based on wafer technology and because they have a relatively simple laser cavity design requiring only relatively low-cost and low-brightness pump diodes.

In section 3.2 the performance of a mode-locked VECSEL [21] (provided by M Squared lasers) having a footprint of only 140x240x70 mm was evaluated for *in vivo* multi-photon microscopy in both, fixed and *in vivo* samples.

The successful implementation of this, non-expensive, maintenance-free, turn-key, compact laser system for a wide range of biological applications (based on different markers and SHG) could potentially facilitate the wide-spread adoption of nonlinear imaging techniques into "real-life" applications.

Based on the experience obtained working with the SDL system, the aim of this work was to take a step forward on the development of chip-sized ultra high performance lasers at substantially lower cost. Therefore, the ultimate goal consisted on implementing chip-sized devices capable of producing the required peak intensities to produce NL excitation. This ambitious goal was motivated by the need of taking the laser systems towards the sample, rather than doing it the other way around, as it has been done for many years. As it is known part of the technology evolution consists on the miniaturization of devices linked to a reduction on their price. Therefore the future outlook for these laser systems is to reach pocket-sized devices with high wall plug efficiencies.

Although the use of such devices was planned as a future work, the strong motivation and the obtained results in this thesis allowed presenting the first NL imaging demonstrations of chip-sized devices (provided by The University of Dundee). The achieved results enable to outline the future developments in ultra-short pulsed technology devices which could potentially be used for a wide range of bio-imaging applications such as micro-endoscopes, lab-on-a-chip devices etc.

In order to bring into context the laser systems employed in this research, figure 3.1 depicts the employed chip-sized and SDL devices. Additionally, other reference devices such as the Ti:S laser which is one of the most known USPL system are shown. These are plotted according to the employed average and peak powers at the sample plane. The diagonal lines are the FOM2p values obtained for each device.

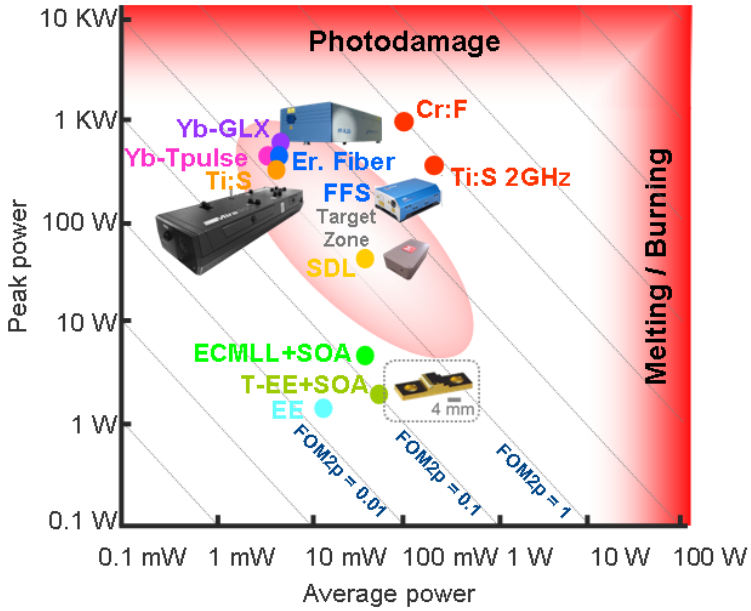

Figure: 3.1. Two-photon figure of merit plot of the laser sources employed in the work and reference sources such as: Ti:S (Coherent), Yb-GLX (Time-Bandwidth Products), Er-Fiber FFS (Toptica Photonics), and Yb-Tpulse (Amplitude Systems). The diagonal lines represent the figure of merit. The target zone refers to the region where FOM2p is optimum for NL imaging (Acknowledgement to K. J Weingarten).

3.2. *Laser source characterization for nonlinear imaging*

In this section, the integration and characterization of compact laser sources into the developed nonlinear imaging workstation will be described. The advantages of having a device designed to match the sample properties will be demonstrated by imaging prepared slides containing different dyes and *in vivo Caenorhabditis elegans* (*C. elegans*) nematodes expressing GFP in a specific set of motor-neurons. In addition, the extended versatility of the laser is shown by presenting SHG images of pharynx, uterus and body wall muscles,

followed by a demonstration of the ability of this source to excite various commercially available dyes.

The experimental setup shown in Figure 3.4 was implemented in the NLM workstation. The mode-locked VECSEL or SDL system (provided by Msquared lasers) was characterized for NL imaging considering its operating parameters (wavelength, repetition rate, pulse width and output average power) for achieving efficient NL imaging. The SDL available for this work was a sealed system that required no maintenance or cleaning. Its operation is based on a simple web-based interface accessed through a PC.

This laser design is basically a V-shaped cavity centered on the VECSEL chip mounted on a heat sink. The pump beam of this laser is focused at an angle of 45 degrees towards the VECSEL. A quantum-dot SESAM and a curved output coupling mirror form the end-mirrors of the laser cavity (see figure 3.2).

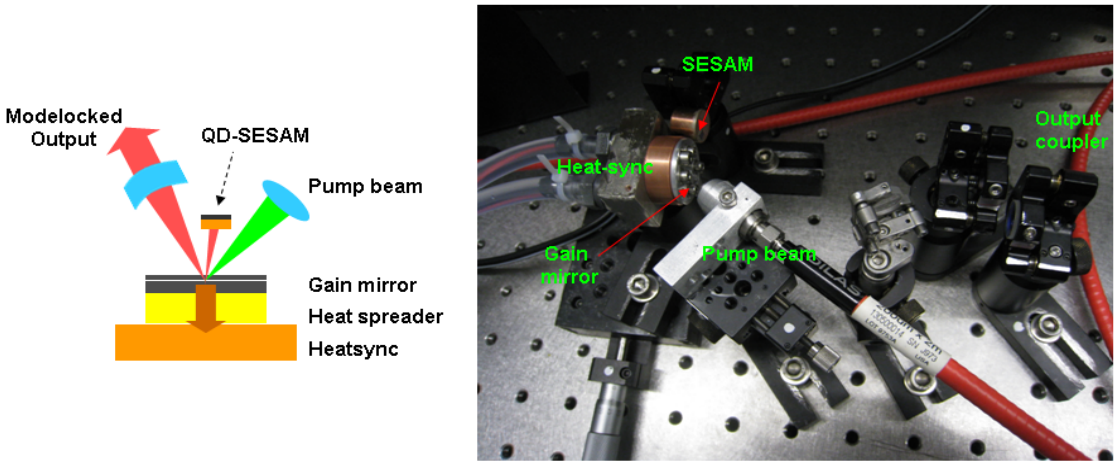

Figure: 3.2. Schematic of the V-shaped cavity centered on the VECSEL chip and mounted on top of a heat sink (left side). The pump beam of this laser is focused at an angle of 45º towards the VECSEL. A quantum-dot SESAM and a curved output coupling mirror form the end-mirrors of the system cavity. The right panel is the actual laser system configuration (provided by Msquared).

The VECSEL gain chip is mode-locked with a quantum-dot SESAM [22-24] to produce 1.5 ps pulses at 500 MHz with an output average power of 287 mW corresponding to 0.4 KW peak power. Importantly the laser output wavelength was selected/developed to be centered at 965 nm in order to match the two-photon action cross-section of GFP (see figure 3.3), one of the most widely used fluorescent markers for bio-imaging applications, [25-29].

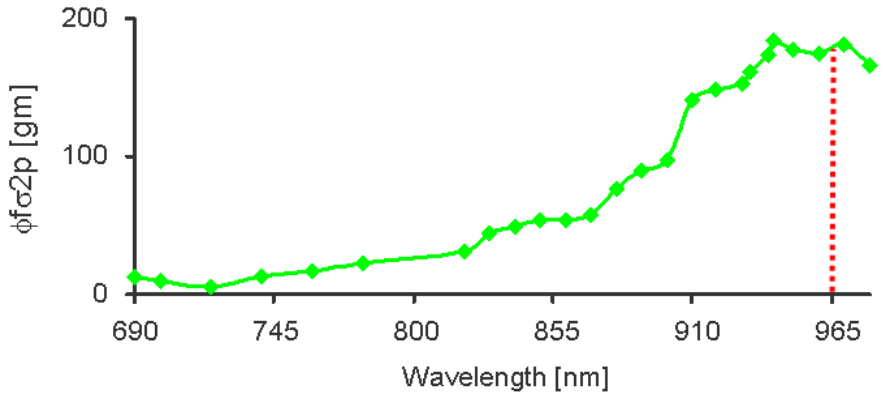

Figure: 3.3. Two-photon action cross-section plot of green fluorescent protein [29]. The red line is the SDL laser system operating wavelength.

Exciting the GFP at 965 nm substantially relaxes the required FOM2p (ranging between 0.1 and 1.36 W^2) and directly allows for the reduction of the corresponding average and peak power values needed for TPEF-based imaging.

A path was built to couple the light source into the NLM workstation taking advantage of all the previously placed optical elements (the same design considerations taken in chapter 2 section 2.1 were followed). For this specific strategy the corresponding filters were changed. A filter cube, containing a hot mirror (Semrock, Inc., FF670-SDi01 transmittance = 360 nm – 650 nm reflectance = 680 nm – 1080 nm) and a BG39 band pass filter were used to separate the excitation beam from the generated TPEF signal. A 40x oil immersion microscope objective with NA = 1.3, (Nikon, Plan Fluor) was used during the experiments (based on the microscope performance assessment carried out in chapter 2). The SHG signal was collected by an oil immersion condenser NA = 1.4 (Nikon). The filter inside the forward detection mount contained a band pass filter (transmittance = 475 - 485 nm) to acquire the SHG signal. To detect the TPEF emission an additional detector (Hamamatsu, H9305-04), was mounted on one of the microscope ports. The real arrangement schematic placed on the optical table employed for this imaging strategy is shown on figure 3.4.

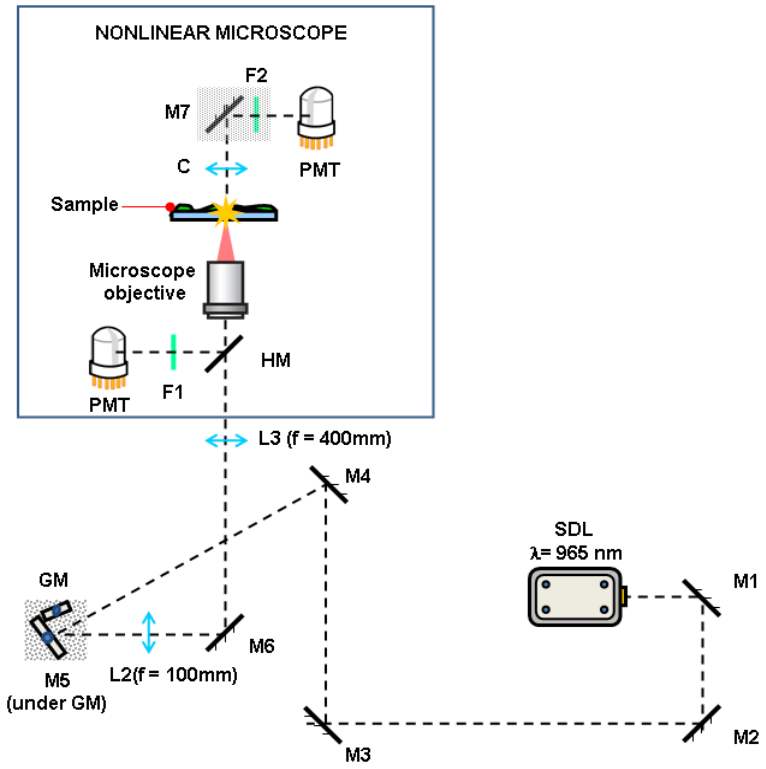

Figure: 3.4. Schematic of the experimental setup used for nonlinear imaging. SDL is the Semiconductor disk laser at 965 nm; M#, mirrors; GM are the galvanometric mirrors; L#, lenses; HM, dichroic mirror; C is the condenser optics (NA = 1.4); F#, band pass filters (F1 transmittance = 330 – 670 nm and F2 transmittance = 475 – 485 nm); and PMT are the photo multiplier tubes.

3.2.1. SDL tests using fixed and *in vivo* samples

The capability of the mode-locked SDL for TPEF imaging purposes was first tested employing 1 µm fluorescent beads (Figure 3.5a) and a mouse intestine section (Figure 3.5b). To obtain these images the average power, measured at the sample plane, was of ~10 mW.

The beads shown in Figure 3.5a containing green fluorescing firefly dye (Duke Scientific G0100) can be excited at 468 nm (if linear excitation is considered) and therefore these are very efficiently imaged with this laser employing TPEF. From image 3.4b (Invitrogen fluo cells slide #4 F-24631) it is possible to see the nuclei of goblet cells labeled with SYTOX green, and the border surrounding these cells arrangement labeled with Alexa Fluor 568 phalloidin. In this sample, SYTOX green possess an absorption peak located around 940 nm. This is very close to the operating wavelength of such laser and therefore, cell nuclei are visualized very efficiently. For the structure labeled with Alexa fluor 568 (filamentous actin in the brush border) the image region is very faintly observed as the dye is more efficiently excited in the 720-840 nm wavelength range. Finally, for the cells labeled with Alexa Fluor 350 (mucus of goblet cells) there is no TPEF signal observed as the excitation wavelength range is restricted to the 720 - 800 nm [30].

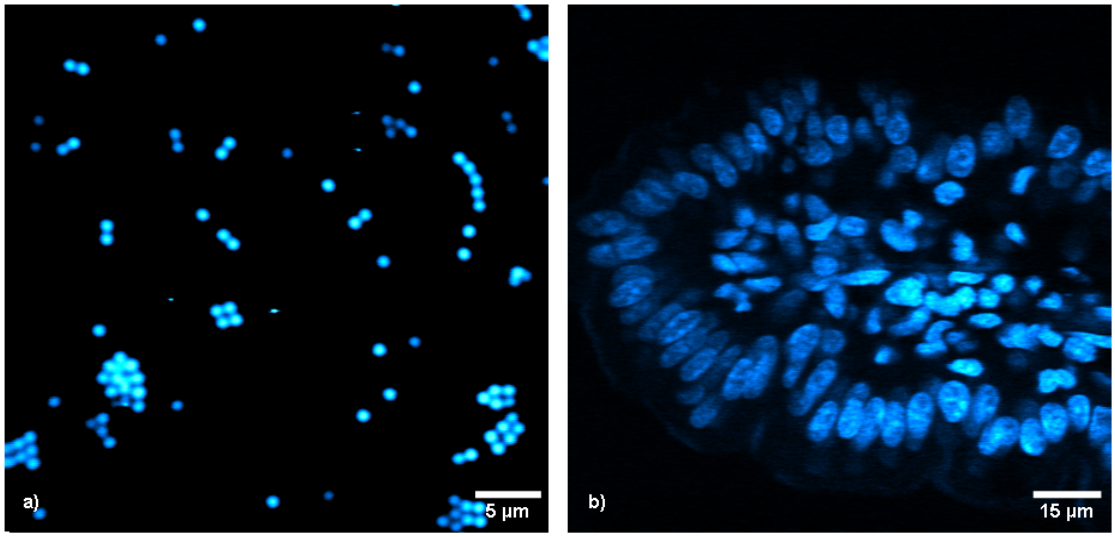

Figure: 3.5. TPEF images from a) green fluorescent beads and b) mouse intestine section labeled with Alexa Fluor 350 WGA (mucus of goblet cells), Alexa Fluor 568 phalloidin (filamentous actin prevalent in the brush border), and SYTOX Green nucleic acid stain (nuclei of goblet cells). All the images are 500x500 pixels.

The next experiment consisted on testing the laser for *in vivo* imaging. For this purpose genetically modified *C. elegans* nematodes expressing GFP in VD-Type (ventral/dorsal) motor-neurons and in the pharyngeal nerve ring neurons (juIs76 [unc-25::gfp]) were employed (see appendix A 1.5 for mounting procedures). Furthermore, to emphasize the imaging capabilities of the SDL all the TPEF images where simultaneously recorded with any SHG signal that could be originated from the nematode. Sample imaging was performed employing an average power of 34 mW (measured at the sample plane) which corresponds to a peak power of ~0.04 KW and a FOM2p = 1.36 W^2. Employing this configuration, no exposure related changes on the anatomical and behavioral characteristics of the sample was observed. In these experiments, the threshold peak power for getting a TPEF image from the GFP expressed in the nematode was ~0.01 KW, corresponding to a FOM2p of approximately 0.1 W^2.

The first region to be imaged was the head of an adult *C. elegans* nematode (see Figure 3.6). Figure 3.6a (TPEF signal depicted in blue), shows the three dimension (3D) projection of the GFP tagged neurons in the *C. elegans* pharyngeal region. Image 3.6b (SHG signal depicted in orange) shows the anterior bulb of the pharyngeal region. In this figure, some parts of the neurons forming the nerve ring are also observed even though a narrow band SHG filter was used (see green arrow). This could possibly be due to fluorescence leaking through the SHG filter or SHG emission from the neuron [31]. Mapping the TPEF and SHG signals (Figure 3.6c) enables the observation of how the neurons forming the nerve ring innervate with the isthmus of the pharynx.

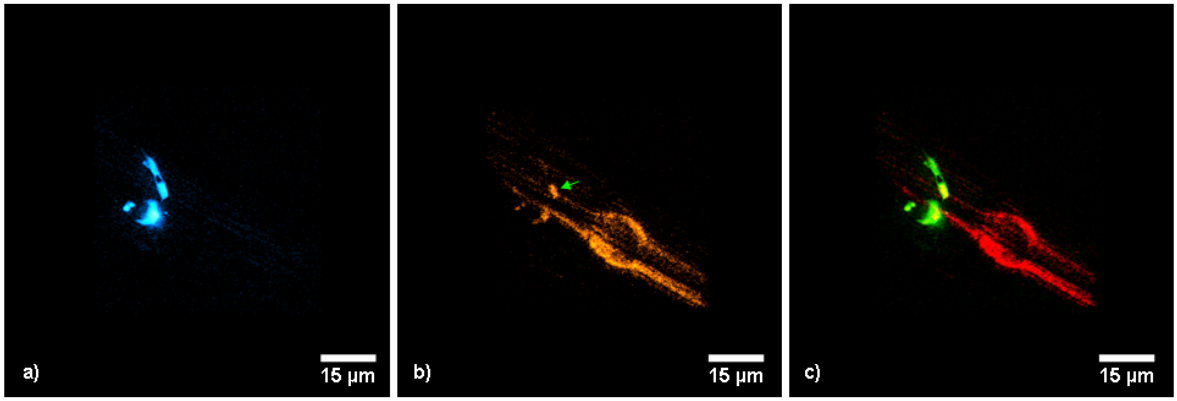

Figure: 3.6. 3D projections of a) TPEF signal from neurons forming the nerve ring expressing GFP (blue) and b) SHG signal from the pharyngeal region (orange) of the *C. elegans* nematode. c) Merged TPEF (Green) and SHG (red) images of both structures. The 3D projection is composed of 55 stacks separated 1 µm. A single x-y optical section was taken in less than 2 seconds. For the SHG image an average of 10 frames was applied to improve the signal-to-noise ratio. All the images are 500x500 pixels.

To further demonstrate the capabilities of this laser the uterus of an adult *C. elegans* nematode (see Figure 3.7) was imaged. Figure 3.7a shows a set of VD-type motor-neurons expressing GFP. On the upper part of image 3.7a, the ventral nerve cord and motor-neurons cell bodies (near the vulva) can be clearly observed (bright spots at the top end of the image). Additionally, in the same image on the lower and upper parts, a weak epi-detected SHG signal from body wall and uterus muscles is observed (see green arrows Figure 3.7a).

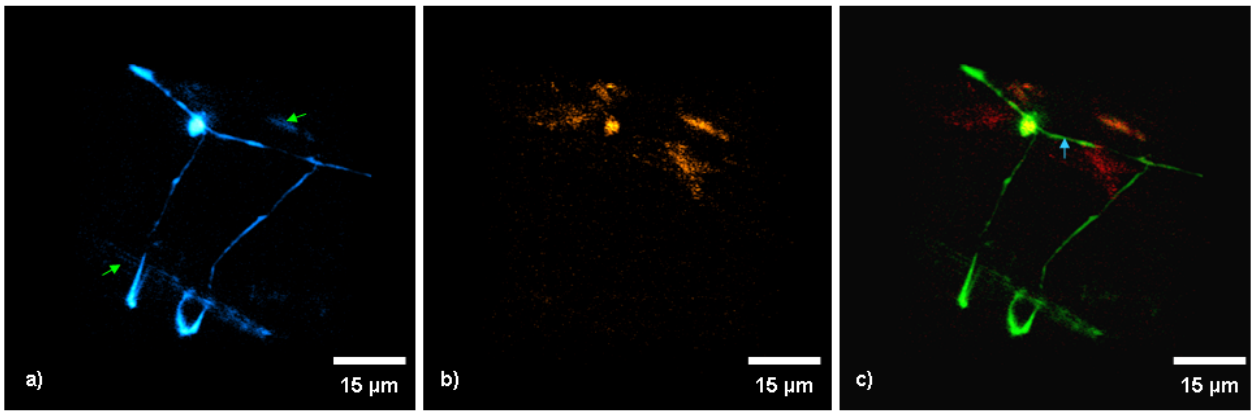

Figure: 3.7. 3D projections of a) TPEF (blue) of a set of motor-neurons expressing GFP and b) SHG (orange) signal of the muscles in the uterus region of a *C. elegans* mid body region. c) Merged TPEF (Green) and SHG (red) images. The 3D projection is composed of 50 stacks separated 1 µm. A single x-y optical section was taken in less than 2 seconds. For the SHG image an average of 10 frames was applied to improve the signal-to-noise ratio. All the images are 500x500 pixels.

In panel 3.7b, the vulva muscles (*C. elegans* diagonally positioned) can be observed together with a motor-neuron cell body (bright spot). This spot, similarly to Figure 3.6b, could be due

to auto-fluorescence leaking through the filter or SHG emission similar to the one observed in Figure 3.7a. The superposition of both signals enables the observation of the vm-type 1 and 2 vulva muscles and a portion of the body wall muscles in close relation with the motor-neurons that are responsible for locomotion (blue arrow).

Based on both imaged regions from the *in vivo C. elegans* samples, a very efficient TPEF signal is observed despite the fact that a very low peak power is used. The main reason for this is that the SDL system operating wavelength is located around the GFP maximum two-photon action cross-section [25, 28, 29]. The relaxation of the required intensities to excite GFP, would, in principle, maximize sample viability given that the ratio of the energy absorbed to the input energy flux determines the possible induced sample damage.

3.2.2. SDL performance tests using several fluorescent markers

This device was designed to operate at a fixed wavelength; however, it can be used for TPEF imaging using other bio-markers. To experimentally demonstrate this, different dyes in solutions (available in the lab) were excited with a constant laser output power of ~10 mW (measured at the sample plane). These were JC-1 (Invitrogen T-3168), Fluorescein (FD70 Sigma-Aldrich) and DiO (Invitrogen D3898) having a concentration of 1 mg/ml in Milli-Q water. In addition to these Calcium green (Invitrogen C-3732) and Fluo-4 (Invitrogen F-14217) were also used as supplied. Finally, a fluorescent sample, consisting of conventional red water paint (slightly diluted in water) was applied onto a zero thickness cover-glass. The dried sample was placed directly at the sample plane of the microscope. The emitted fluorescent spectrum had a bandwidth of 40 nm (measured at the full width half maximum) and was centered at 600 nm.

The relative TPEF signal intensities were recorded using the photo multiplier tube (PMT) voltage value. For each image the background signal was first set to zero and then the emitted signal was adjusted so that only a few pixels were saturated (with an intensity of 255). In each case, low TPEF signal resulted in high PMT voltages and vice versa [32]. Figure 3.8 shows images of different dyes that were placed on top of a cover-glass. In each image, the voltages resulting from the excitation with the SDL laser system were recorded.

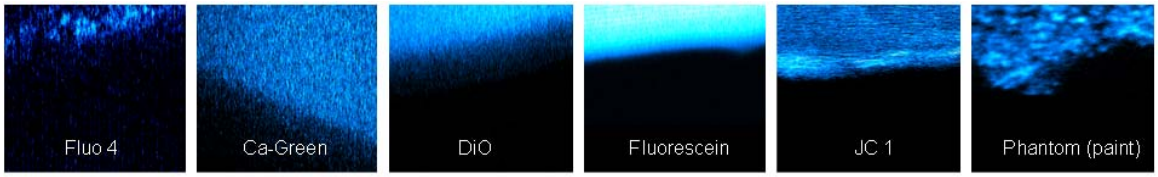

Figure: 3.8. TPEF images from different dyes in solution. All the images are 500x500 pixels. The field of view of all the images is of 40x40 μm.

It is important to mention that, the precise detector setting may vary not only between instruments but also between samples. However the excitation/emission general trend should

not change, meaning that the PMT values shown here are not absolute but they are relative guides to help in understanding the imaging capabilities of the laser.From above it can be observed that the laser can be used for efficiently exciting different biological markers. The threshold peak power to obtain nonlinear images was measured for all the samples. For the brightest sample (JC1) 0.5 W were required corresponding to a FOM2p of 0.0003 W^2 while for the dimmer case (Ca-Green) 5 W were required having a FOM2p of 0.022 W^2. To further illustrate its applicability a theoretical estimation on how efficiently the laser would excite other dyes was carried out. These calculations were based on the two-photon action cross-section of several dyes relative to GFP at 965 nm (~180 Goeppert-Mayer, data taken from ref. 29). By performing such calculation it is possible to determine that the expected TPEF signal compared to GFP are 0.05 for Bodipy, 0.20 for Alexa 488, 0.47 for dsRed, 1.00 for mVenus, 1.15 for YFP, and 1.54 for mCitrine.

3.2.3. SDL assessment for time-lapse and depth imaging

Alternative applications (based on the use of GFP) in which the laser can be used are monitoring membrane potentials [33], selective non-linear optical sensing of electrophysiological processes in *C. elegans* [34], protein dynamics recording inside living cells through photo-bleaching experiments [35], and depth imaging just to mention a few.

From these applications additional tests were performed to assess the suitability of the SDL laser system for the more general use in NLM. I will first start by describing the suitability of such system to be used to photo-bleaching experiments [35] as the means to assess its performance for long-term time-lapse imaging studies. Then I will briefly discuss the tests performed to evaluate the SDL performance for depth imaging studies.

The photo-bleaching experiments consisted on attempting to bleach a cell nucleus (expressing GFP) as fast as possible, to simulate a long-term time-lapse imaging experiment being this the worst case scenario where the dye is continuously irradiated with a large dwell time.

The relative two-photon signal intensities were recorded using the PMT voltage value form the whole image. In this experiment, the continuous exposure time-lapse experiment lasted for 0.5 hours. The average power was 34 mW (measured at the sample plane). By analyzing the results obtained on figure 3.9 (bottom panel), long-term time-lapse studies could be carried out by imaging the sample for four seconds (500X500 points image takes around <1 second). This means that if four frames are accumulated (to improve the signal-to-noise ratio) every 5 minutes, it will be possible to image a specimen for up to 34 hours. In this case, the sample would be exposed for short periods of time allowing it to recover after every exposure.

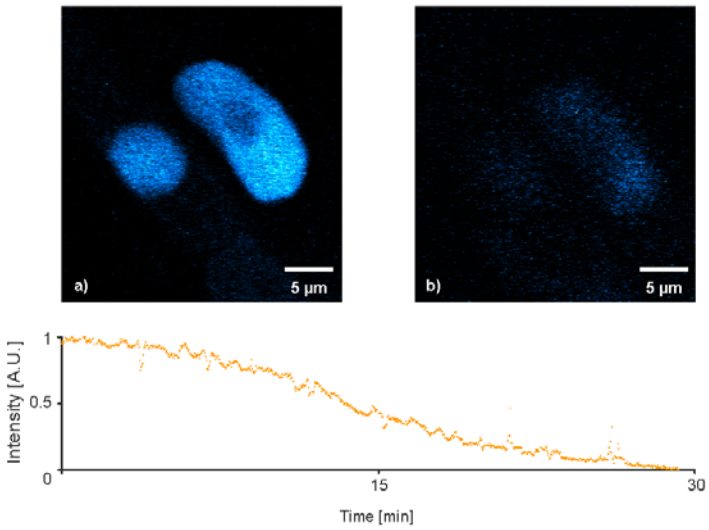

Figure: 3.9. Photo-bleaching rate experiments employing the SDL at a constant average power of 34mW at a) the beginning of the imaging and b) after 0.5 hrs of continuous exposure in the nonlinear microscope.

Moreover, this experiment was carried out employing the maximum available power, however, this could also be modified accordingly always taking into account the sample integrity during the whole study. These results demonstrate that such laser system is suitable for performing long-term time-lapse imaging studies.

Depth imaging is one of the main advantages of NLM. The aim of this experiment is to demonstrate that this is indeed the case. This was first attempted using a 20x, 0.5 NA objective as it provides an increased working distance. A thick sample containing GFP was used for obtaining a 3D stack (data not shown). The employed average output power was < 50 mW. In this case, it is known that the SDL system pulses are long (1.5 ps). This together with the low NA, as expected, produced a large focal spot generating thus a weaker confinement of the light. To address this, the next step consisted on employing a higher NA microscope objective (available in the laboratory). Although the working distance was shorter, the size of the point spread function is smaller, providing thus higher intensities

For this purpose a phantom sample consisting of fluorescent beads embedded in 2% agarose gel was employed. The experiment consisted on analyzing the decay of the generated TPEF intensity versus the imaging depth at a constant average power of 10 mW and under high NA conditions. Figure 3.10 shows the obtained results.

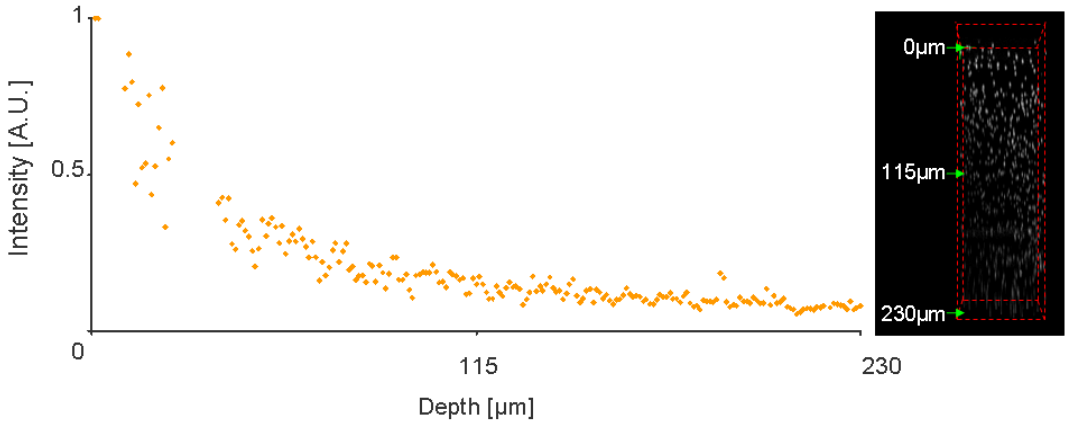

Figure: 3.10. Left panel is the intensity decay as a function of depth. The right panel is the image of a phantom sample obtained employing the SDL prototype at a constant average power of 10 mW. Maximum depth is 230 µm.

From the experimental results, it can be visualized that the limiting factor in this test is not the power requirement as all the sample features can be observed even at a depth of 230 µm. In this case what limits the imaging efficiency using the SDL are the aberrations caused by the sample at deeper planes (see the enlarged features of figure 3.10 at the maximum imaged depth caused by loss of the diffraction limited performance of the system) together with the working distance of the microscope objective. As a future work infrared optimized water immersion microscope objectives, which combine large working distances together with high NAs, could be used to further increase the achievable penetration depth. A strategy to eliminate aberration effects caused by refractive index mismatch will be presented on chapter four.

As it has been observed, the SDL system operates at a fixed wavelength, the delivered pulses are five times broader compared with other laser sources, the repetition rate is six times higher than what other laser sources provide. Nevertheless, this novel laser source can be employed for different nonlinear bio-imaging applications. This has been carried out by employing the FOM2p for the design of such laser system. The next question to be answered in this thesis was: Can this laser system be employed as an alternative source to substitute the conventional Ti:S system considering its size, price and operating advantages?. This question will be answered in the next subsection.

3.3. SDL comparaison vs. Ti:Sapphire laser

In this section the SDL device performance was compared to the Ti:S laser which has been used as a standard excitation source for NLM workstations in many research labs for more than two decades. The experiments were performed employing two nonlinear imaging modalities (TPEF and SHG) in a wide range of specimens including *in vivo* samples.

For such purpose a Ti:S laser system was added to the NLM work station following the same design criteria employed on section 2.1 (chapter 2). A flip mirror was used to either select the Ti:S laser or the SDL system to enable a sequential acquisition using both sources and also to use the existing optical elements to minimize the system complexity. In figure 3.11 the additional path for using the Ti:S laser system can be observed.

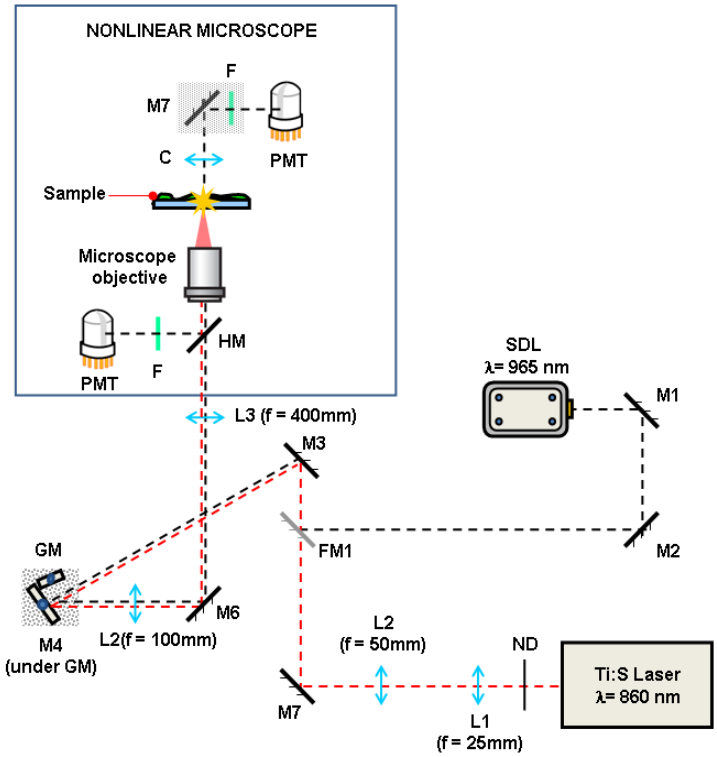

Figure: 3.11. Schematic of the experimental setup used for nonlinear imaging. SDL is the Semiconductor disk laser at 965 nm; Ti:S is the titanium sapphire laser at 860 nm; M#, mirrors; ND, neutral density filter; L#, lenses; FM1, is the flip mirror; GM are the galvanometric mirrors; HM, dichroic mirror; C is the condenser optics (NA = 1.4); F#, band pass filters; and PMT are the photo multiplier tubes.

All the TPEF signal comparison experiments were carried out using the Ti:S laser at 860 nm (as the laser in the laboratory needs to be purged to be able to reach wavelengths above 900 nm in a stable way) and the SDL prototype working at 965 nm. To obtain the following images, a similar average power was applied for both acquired signals. This is performed to allow a fair comparison between both sources. It is important to mention that to interpret such images; the wavelength difference directly related with the two-photon action-cross section needs to be considered (see figure 3.3)

The first trial was performed employing a fluorescent beads sample. A single frame was taken using both sources (see figure 3.12). As is can be observed the obtained signal from both lasers has a similar quality. However it was required to almost double the peak power of

the Ti:S laser as its two-photon action cross-section is 3 times less due to its operating wavelength [29].

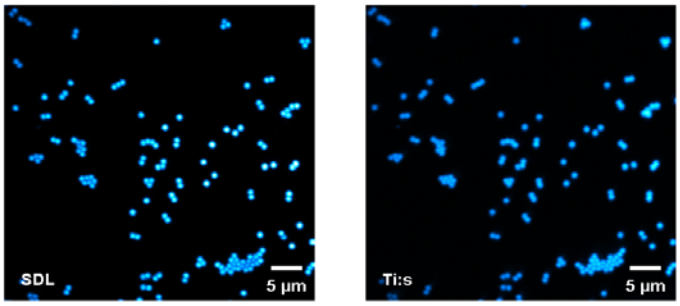

Figure: 3.12. Single fames taken from a fluorescent beads sample (TPEF signal depicted in blue). Left panel depicts the image taken with the SDL prototype employing 50 W peak power. Right panel depicts the image obtained using the Ti:S laser using 90 W peak power given that the two-photon action cross-section is 3 times less for the employed operating wavelength.

With this conditions the obtained images using the SDL have almost twice the contrast ratio compared with the ones obtained using the Ti:S obtained image (SDL contrast ratio 17.5:1 and Ti:S contrast ratio 8.9:1). In this sense it can be concluded that the SDL system will provide good quality images based on its wavelength and its operating specifications.

In a similar way, a living *C. elegans* nematode expressing GFP in motor-neurons was imaged. In this trial the same comparison of both signals was carried out (also accounting for the two-photon action cross-section of the Ti:S laser). Figure 3.13 depicts the obtained results acquired using both lasers.

In the top row of figure 3.13 a single frame is shown using both laser systems. In order to optimize the signal-to-noise ratio the result of 10 frame accumulation is depicted in the bottom row of the same figure. In this case it is also evident that both lasers are able to deliver images having a similar quality as both contrast ratios have similar values independently of the frame accumulations performed. The SDL contrast ratios are 13.3:1 and 18.7:1 for the single and accumulated frames respectively. The Ti:S contrast ratios are 17.1:1 and 19.8:1 for the single and accumulated frames respectively.

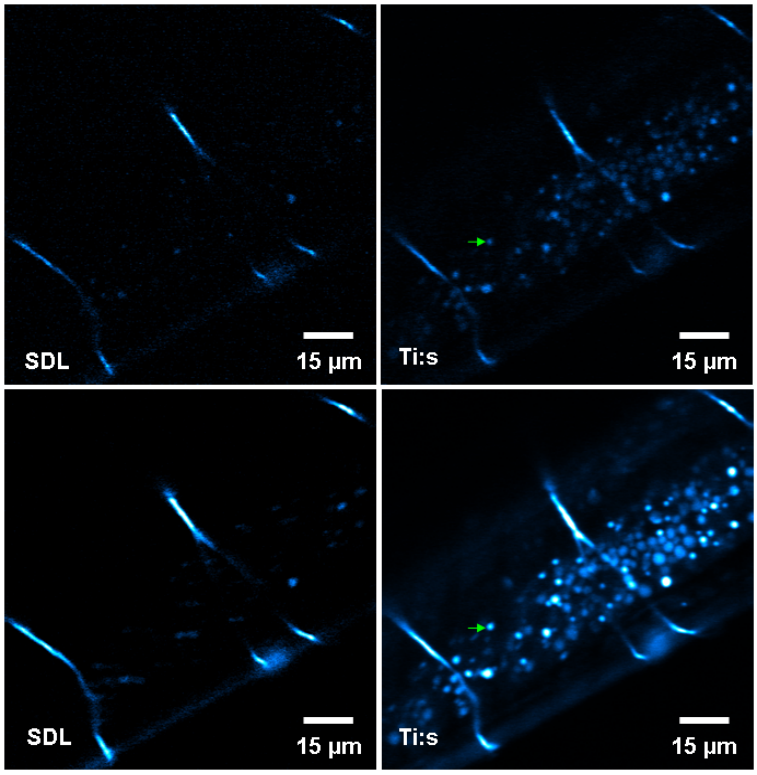

Figure: 3.13. TPEF signal taken from an *in vivo C. elegans* sample (blue). The top row is a single frame taken using both the SDL (left) and the Ti:S (right) lasers. Bottom row is an averaged version of the images taken with both lasers to enhance the signal-to-noise ratio (10 frames were acumulation). The green arrows point out the intestine of the *C. elegans* nematode, where the auto-fluorescence signal is generated.

In the right column of figure 3.13 (Ti:S laser) additional structures can be observed. These features are evident due to the auto-fluorescence (see green arrows) from the intestine of the *C. elegans* sample. Typically, auto-fluorescence signals are obtained as the excitation wavelength is reduced (i.e. larger excitation energies). This emission can be spectrally broad and it may sometimes be unwanted information, which often interferes with the signal obtained from the structure under study. In this sense the SDL prototype, due to its longer operating wavelength, gives a cleaner image.

Finally, the SHG signal obtained using both sources was assessed. In a similar way, a living *C. elegans* sample (figure 3.14 left column) and a starch granules where imaged (figure 3.14 right column). In this experiment the SHG nonlinear coefficient does not depend on the used wavelength. Therefore, as expected, the SDL required a higher peak power in order to obtain a signal with similar contrast to that obtained using the Ti:S laser as the excitation source. To obtain similar signal-to-noise ratio images, a larger amount of frames need to be averaged when the SDL was used (top row figure 3.14).

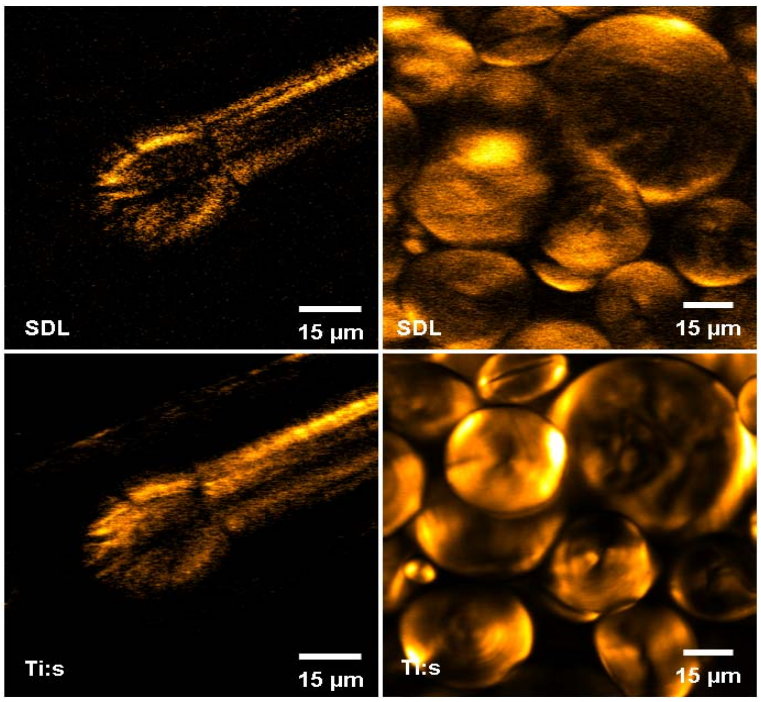

Figure: 3.14. SHG signal acquired from an *in vivo C. elegans* and strarch granules (yellow signal). Left column is the result of 15 averaged frames taken using both the SDL (top) and the Ti:S (bottom) lasers to image the *C. elegans* nematode. The right column is the result of 10 averaged frames taken using both the SDL (top) and the Ti:S (bottom) lasers to image the starch granules.

This requirement was due to the fact that a peak power of 50 W reaches the sample plane when the SDL prototype is used, while the peak power at the sample plane when the Ti:S laser is used is more than 5 times higher compared to the SDL due to its longer pulse width. For this reason, the obtained contrast ratio using the Ti:S laser in the *C. elegans* nematode is about two times higher compared with the one obtained using the SDL (Ti:S 4.5:1 and SDL 2.6:1). On the other hand, for the starch sample a slight change on the contrast ratio is observed as the obtained values are 16.7:1 for the SDL and 19.6:1 for the Ti:S system.

This experiment indicates that although the laser is able to generate nonlinear images, there is a need for higher peak powers (as average power is already high). This means that the laser has to deliver shorter pulse durations for the same average power. This information is currently being used for future improvements of such laser source.

As a future outlook, the miniaturization of these devices employing solid state technology was expected to happen as is has been observed with other technologies. The first proof of concept studies for reaching this goal will be presented in the next subsection.

3.4. Chip-sized Ultra-short pulsed laser systems

In the previous sub chapter a compact laser source was designed considering the case of samples expressing one of the most widely used fluorescent markers (GFP) in bio-imaging

research. In this characterization an experimental validation of the imaging thresholds for obtaining NL signal from different samples was recorded. These measurements were taken as a way to have a reference value to be able to assess the potential of ultrafast and ultra-compact electrically-pumped laser systems for bio-imaging and bio-medical applications.

In this sub section, part of what was planed as future work, was also performed in this thesis to offer alternative ultra-short pulsed chip-sized laser systems (provided by The University of Dundee) to be used for NLM applications. Moreover, this work was carried out to demonstrate the potential impact of compact devices to enable taking NL imaging technology outside the laboratories (i.e. bringing the technology towards the sample). The chip-sized devices were designed considering the sample optical properties to improve its interaction with the emitted light. To achieve this, the devices were based on InAs/GaAs quantum-dot structures, as these materials can be routinely grown to cover the spectral range between 1200 nm and 1300 nm. In addition to this, they offer important advantages in the context of USPLs such as, broad gain/absorption bandwidth, excellent noise characteristics and low optical losses [36-40]. This emission range was selected because it is known that at these wavelengths, the water absorption is located at local minima and at the same time scattering effects are minimized.

Chip-sized lasers currently provide moderate peak powers due to the long pulse durations and very high repetition rates since they are still on its development stage. Therefore, the same strategy of wavelength matching followed with the SDL was applied in this case. The most suitable fluorescent marker was also selected. By making such consideration this ensures that although having such power conditions it is possible to demonstrate the potential use of chip-sized devices for TPEF imaging.

It should be noted that, the use of longer excitation wavelengths will result on a reduction of resolution as the diffraction limited focal volume scales linearly with wavelength in each dimension. However, the advantage of employing such wavelengths will be helpful for achieving larger penetration depths and the minor loss of resolution is a reasonable compromise.

The use of sources operating around 1200 and 1300 nm has been experimentally demonstrated. In [41], a comparison between 1280 nm with 775 nm excitation (generated by a Ti:S-pumped optical parametric oscillator and a Ti:S oscillator, respectively) was carried out for imaging tissue at different depths. The results demonstrated that employing 1280 nm it is possible to image at twice the depth when compared to the depth achievable using 775 nm excitation. The advantages of this wavelength for NLM applications are therefore linked to the larger penetration depths which result from the decreased scattering [41], the reduced probability of photo damage (based on the wavelength dependence of multi-photon absorption related processes) and its intrinsic ability to filter auto-fluorescence [42].

In this context, compact Cr:forsterite lasers emitting at 1230 nm have been demonstrated as excitation sources for NLM with great success [43, 44]. Additionally, a few semiconductor laser diode systems with amplification schemes have been successfully demonstrated as light sources for NLM applications at the abovementioned wavelength [13-15]. These laser diode systems are typically built-in two or more amplification stages (based on semiconductor and/or fiber amplifiers), as well as extra-cavity dispersion compensation schemes.

In this subsection the first semiconductor pulsed laser diode systems working within the spectral range of 1260 nm having characteristics compatible with NLM applications are demonstrated.

Preliminary results of these low-cost, chip-sized (chip dimensions up to 6 mm) based devices, for NL imaging applications are presented. These systems are based on all-semiconductor quantum-dot structures with an emission wavelength centered around 1260 nm. This emission is located within the infrared penetration window of most biological tissues. Such asset could potentially offer greater penetration depths and reduced sample damage [41, 42] compared with the classical ultra-short pulsed laser systems (Ti:S). All this could lead to a major progress and a wider spread adoption of nonlinear imaging technology.

In this research, several devices were tested. To show the efforts of pushing the peak power to meet NLM requirements, the improvement of the obtained figure of merit is shown for three of the latest tested devices. It is important to recall that the FOM2p is useful for determining if the laser source is suitable for NL excitation as the detected signal level from a two-photon process is proportional to this FOM2p. In this sense, the threshold figure of merit obtained with the SDL device considering the brightest dye was of 0.003 (recorded at the sample plane). This reference value was employed to asses the suitability of chip-sized devices to be used for NL imaging applications. Table 3.1 contains the specifications for these devices (see table 3.1). See also figure 3.1 for a comparison of the performance of these devices versus other laser systems.

Table 3.1. Chip-sized ultra-short pulsed laser systems.

Chip-sized laser system	**Pulse duration [pS]**	**Rep. Rate [GHz]**	**Output**		
			Avg. Power [mW]	**Peak Power [W]**	**FOM2p [W^2]**
a) Edge emitting system	1.0	10	100	10	1
b) Tunable laser and semiconductor optical amplifier	3	10	370	12.3	4.5
c) External-cavity passively mode-locked laser	10.5	0.648	208	30.5	6.3

Comparing the figure of merit with the threshold value obtained in the previous subsection enabled to validate the suitability of using these devices for obtaining a NL signal from a sample when the two-photon action cross-section is well matched. This enabled to show a proof of principle demonstration and to validate the efforts carried out to push the performance of such devices towards their limits.

To test the devices, these were property connected, mounted and coupled into the NLM workstation. In this part special considerations must be taken into account as the peak power delivered still requires passing through several optical elements to couple the light into the microscope. In this sense a special path was built (according to section 2.1 design considerations) in the NL imaging work station, to reduce as much as possible such losses. The beam was expanded to fill the back aperture of a CFI Apochromatic, 60x, 1.4NA, Oil immersion, microscope objective (λS, Nikon). The sample was scanned in x-y directions using a translation stage (Märzhäuser Wetzlar, IM 120 x 100). To acquire the TPEF image a band pass filter (KG3 Schott) was placed in front of a PMT (Hamamatsu, H9305-03). The tested configurations can be observed in figure 3.15.

In an effort to demonstrate the use of chip-sized devices for TPEF imaging, the three latest device configurations are shown in Figure 3.15 (see right panel).

The first configuration consists on an edge emitting device with an emission wavelength centered at 1260 nm. This device delivered 1 ps pulses at a repletion rate of 10 GHz, and an average power of 100 mW. Under this configuration the output peak power was 10 W. Based on the experimental data obtained using the SDL system it was clear that this amount of peak power could be enough to produce TPEF images. However, as the device was on the low side of the threshold value, the requirement of increasing the amount of power was carried out by designing two extra configurations. The second system consisted on a tunable device (1245-1295 nm) amplified by a chip-sized Quantum-dot based semiconductor optical amplifier (SOA). Such amplifiers are extremely suitable for boosting the power of ultra-short pulses due to their high gain saturation characteristics, broad gain bandwidth, fast gain recovery times and low noise figure [45]. Although this configuration provided larger pulses (3 ps), the average power was increased to 370 mW and the peak power was 12.3 W. The repetition rate in this configuration was also 10 GHz.

Aiming to produce as much peak power as possible, one of the solutions was the use of an external cavity configuration. In this case the third configuration was built to have a similar repetition rate to that of the SDL, corresponding to 648 MHz. By doing so the peak power was increased to 30.5 W.

The tests performed using the configurations depicted on figure 3.15 will be described in the following text.

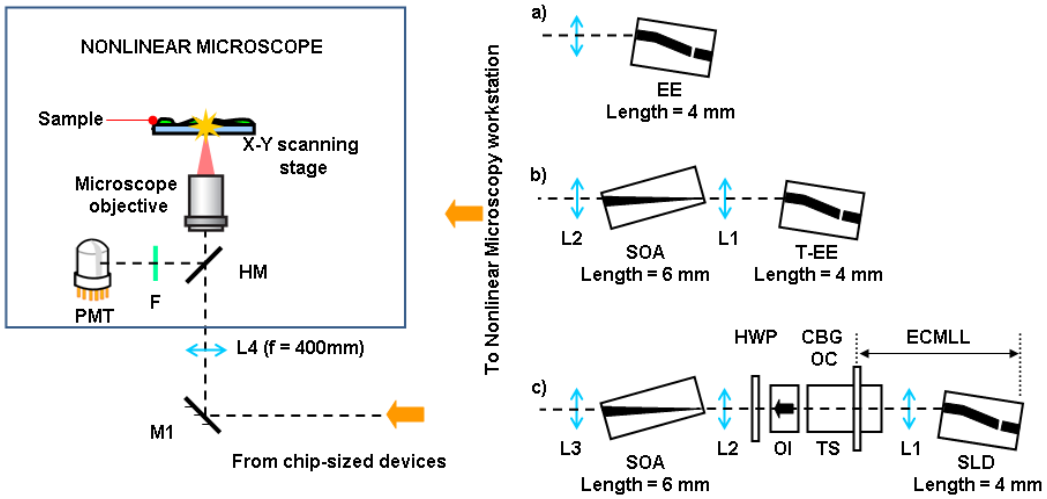

Figure: 3.15. Quantum-dot ultra-short pulsed laser systems showing the three tested configurations. A) Edge emitting (EE) device, b) Tunable edge emitting (T-EE) device + semiconductor optical amplifier (SOA) c) external cavity mode-locked laser configuration (ECMLL) + SOA. SLD, super-luminescent diode; L#: lenses; CBG OC, chirped Bragg grating output coupler; TS, motorized translation stage; OI, optical isolator; HWP, half wave plate; ; M#, mirror; HM, dichroic mirror; F, band-pass filter; PMT, photomultiplier tube.

From table 3.1 it is possible to observe that the first chip-sized device configuration (see figure 3.15a) is capable of producing TPEF images if the FOM2p is compared to that obtained with the SDL system (see section 3.2). As it has been measured in chapter 2, at near infrared (NIR) wavelengths, the major loss occurs in the microscope objective. Therefore, the obtained peak power at the sample plane was around 1.5 W and the FOM2p was 0.02 W^2. Nonetheless if this is compared to the threshold measurements taken on section 3.2, this amount of peak power is enough to nonlinearly excite a fluorescent dye if the two-photon action cross-section is matched.

The two-photon action cross-section of Crimson dye at 1260 nm is ~16 GM [20]. For the nonlinear imaging demonstration, a sample of 15 µm crimson fluorescent microspheres (Invitrogen, F-8839) was used. This type of sample is commonly used for blood flow determination. However for the purpose, of the TPEF demonstration, these were placed in water solution and sandwiched between two cover-glasses.

Using the configuration 3.15a, the image of figure 3.16a (right panel) was obtained. This image is the result of integrating 10 frames from the same sample region. This procedure was performed to increase the signal-to-noise ratio. However it can be clearly observed that individual spheres cannot be clearly resolved. In fact this effect can be attributed to the beam profile which suffers from strong aberrations (astigmatism). Although this was partially corrected with an aspherical lens, no other aberration correction strategies were implemented to avoid generating additional losses reducing the available power. Nevertheless, if more

peak power would be available, such correction could be applied as this would allow better focusing and therefore higher intensities necessary for an efficient nonlinear interaction.

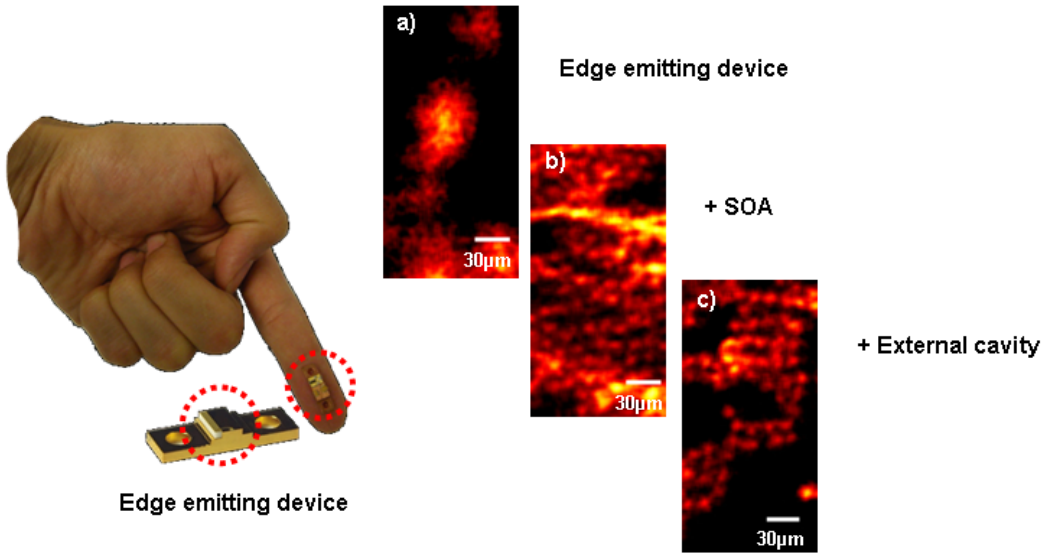

Figure: 3.16. Left side demonstrates the size of an edge emitting device on top of a mount. Right panel are TPEF images obtained with the quantum-dot ultra-short pulsed laser configurations. a) Edge emitting device, b) Tunable edge emitting device + SOA and c) external cavity configuration (ECMLL), + SOA.

For the second configuration an amplification stage was added to the setup (see figure 3.15b). By adding the SOA it can be observed on table 3.1, that the system FOM2p has considerably increased by a factor of four from the previously tested device. In this case the peak power at the sample plane was 1.85 W and the FOM2p was 0.1 W^2 which is five times higher than the previous one. To analyze the impact of having this increased figure of merit, the test sample was imaged. In this case individual spheres can be better visualized besides the fact that the output of the system is still astigmatic 3.16b. The improvement on the image quality can be attributed to the fact that more peak power is available at the sample plane, thus enabling a more efficient nonlinear process. As in the previous case ten frames of the same region were integrated to obtain the final image presented in figure 3.16b. Please note that the scanning speed is limited by the scanning stage (a single frame acquisition takes up to five minutes). Despite that, the obtained results enable to demonstrate the use of these compact lasers for NLM applications. Importantly, this confirms that the FOM2p can be effectively used by the laser manufacturers to optimize the devices for NL imaging. If this parameter is pushed closer to a value of 1 W^2 (at the sample plane), then NL imaging will be possible without having to average frames.

The last laser system configuration to be demonstrated is a master-oscillator power-amplifier (MOPA) based on a quantum-dot external cavity mode-locked laser (QD-ECMLL), amplified by a tapered quantum-dot SOA, with an emission centered at the 1260 nm spectral

band (see figure 3.15c). The choice of an external-cavity mode-locking configuration was built to reduce the repetition rates from what it is obtained directly from these devices due to its short cavity size, as well as offering the possibility to easily vary the pulse repetition rate [40, 46- 48]. At the same time this will have an impact on the FOM2p.

In this configuration an external-cavity design, and an external chirped volume Bragg grating was used as an output coupler. The output power from the pulsed oscillator was boosted by a tapered quantum-dot SOA with a similar epitaxial structure than the oscillator in order to maximize mode matching between both devices. By keeping the pulse energy or peak power of the amplifier input constant, it has been verified that a lower repetition rate corresponding to a lower average input power resulted in a higher SOA gain and a higher peak power, due to the gain saturation characteristics of the SOA. As a result, a lower repetition rate of 648 MHz, resulted in 30.5 W peak power together with a 208 mW average power, and 6.3 W^2 FOM2p.

These values represent the best results ever obtained for the high peak-power pico-second optical pulse generation from an all-semiconductor laser diode system working in the spectral region between 1200 nm and 1300 nm. This scheme uses only a single amplification stage and without external pulse compression, which represents a step beyond to what previous results have been achieved with diode-based systems [13-15].

From the above results it can be observed that the output peak power delivered by the external cavity configuration is similar to the one employed at the sample plane in section 3.2. However, in this experiment, the available peak power at the sample plane was ~ 4.5 W which corresponds to a FOM2p of 0.14 W^2. This amount to peak power is still low compared to the target value none the less it is possible to obtain 2.5 times more peak power compared to the previous device.

Although the beam has also an increased amount of astigmatism, in these experiments the fluorescent beads can be clearly identified (see left panel of figure 3.16c). This is attributed to the fact that the laser is able to deliver higher peak powers in comparison with the last two devices. It is important to mention that also in this case, 10 frames were averaged to improve the signal-to-noise ratio as the peak powers in the sample plane are still near the threshold. As before, if more peak power is available at the sample plane a reduction on the amount of averaged frames could be possible. This enables to demonstrate the potential of the edge emitting devices for nonlinear imaging applications at the 1245−1295 nm wavelength range.

Although this system operates at a fixed wavelength of 1260 nm, it could also be used to efficiently excite a wide range of fluorescent dyes via TPEF such as, mkate variants, TurboFP635, TurboFP650, mRaspberry, mPlum, mGrape3, Neptune, NirFP, mNeptune as these have similar or higher two-photon action cross-section compared to the Crimson dye [20]. Future improvements will be carried out to keep increasing the peak power from the

SOA output. This can be achieved by further decreasing the repetition rate of the external cavity configuration, improving the beam quality (having a uniform intensity in the beam profile rather than an astigmatic one), and improving the input coupling efficiency between the output from the external cavity configuration and the SOA.

The USPL systems presented in this section are the first demonstration of low-cost, chip-sized based devices working in the spectral region of 1245 nm - 1295 nm, with power levels compatible with NLM. This wavelength range is located within the infrared penetration window of most biological tissues. This asset could potentially offer greater penetration depths and reduced sample damage compared with other ultra-short-pulsed semiconductor laser systems operating below this wavelength range.

Importantly, by lowering the repetition rate to 648 MHz, a higher peak power of 30.3 W was achieved together with a 208 mW average power, a 321-pJ pulse energy and a 6.3 W^2 FOM2p. Using a constant pulse energy and peak power as the input, it has been demonstrated that a lower repetition rate, corresponding to a lower average input power, enabled a high SOA gain and consequently the generation of higher peak power (and energy) pulses, due its gain saturation characteristics.

Moreover, and unlike previous demonstrations of nonlinear imaging with ultrafast laser diode systems, it has been presented for the first time systems that incorporate only a single amplification stage, and do not include external dispersion compensation, enabling a rather more compact and less complex laser system.

Preliminary TPEF imaging results indicate that this quantum-dot laser systems are promising as a high peak-power ultra-short pulsed light sources, with a wavelength emission that could potentially cover 1000 nm - 1300 nm, which is very useful for nonlinear bio-imaging applications including micro-endoscopes, lab-on-a-chip devices etc.

These chip-sized devices could lead to major progress and a widespread adoption of nonlinear imaging technology. Increasing the peak output powers of these devices to reach the target requirements of NLM will continue as part of future work.

3.5. Summary

In this chapter a novel compact source based on an SDL design has been presented for the first time to the best of my knowledge for NLM applications. Its operating parameters were advantageous as the operating wavelength matches the two-photon action cross-section of GFP making it an ideal source for one of the most widely used fluorescent markers in bio-imaging research. This condition enabled the excitation of such protein using very low peak powers which is beneficial when dealing with living specimens. To demonstrate that the source is not limited to be used only with GFP, an assessment of different dyes was performed by recording the parameters required to have an optimum NL signal. These tests

demonstrated the suitability of such system to be used with several commercially available fluorescent dyes.

Furthermore specific tests were carried out to fully characterize the SDL prototype. These consisted on long-term imaging experiments assessed through photo-bleaching rate experiments employing *C. elegans* nematodes expressing GFP. This resulted in the conclusion that the laser is able to image living specimens in a successful way without compromising the sample viability. Deep imaging tests (using phantom samples) demonstrated the feasibility of using the system to image thicker specimens without the requirement of additional power. The only limitation was the aberration effects caused by the inhomogeneous structure of the sample and the working distance of the microscope objective.

The SDL was compared side-to-side with one of the most widely used lasers in research laboratories (Ti:S). For that, different samples were used to produce TPEF and SHG signals. Such experiments enabled to conclude that, although the laser is able to generate NL images under high NA conditions; there is a need for higher peak powers (as average power is already high). This means that the laser has to deliver shorter pulses for the same average power in order to reduce the amount of frame accumulation performed for SHG imaging. This information has already been sent to the collaborators involved in the development of such source and a second generation of SDL devices is already being developed.

As a continuation of the research activities and attempting to make a step forward in the use of compact laser sources, three of the latest chip-sized USPL systems in different configurations, were characterized and tested for NLM. From these results it was observed that the average powers of quantum-dot lasers are gradually increasing and have already reached output average powers ranging within hundreds of mW corresponding to a few watts of peak power. Such powers are within the threshold values measured using the SDL device; however the design is suitable for exciting fluorescent dyes in NL fashion if the two-photon action cross-sections of the employed fluorescent markers/proteins are well matched. The preliminary TPEF imaging results here presented indicate that these laser systems are promising as high peak-power pulsed light sources, with a wavelength emission that could potentially cover 1000 nm - 1300 nm, which is very useful for nonlinear bio-imaging applications.

Based on the results obtained so far, it is important to note that the characterized lasers can be integrated in a standard set-up at the first moment as it has been demonstrated in this chapter (SDL and chip-sized devices), and then go towards the development of fully integrated compact NL imaging systems such as the development of micro endoscopes and/or lab-on-a-chip devices for clinical use. This will enable bringing the technology towards the sample or into the clinics. Importantly it has been demonstrated that even having low peak powers reaching the sample plane it is possible to have an efficient TPEF excitation if the laser

operating wavelength is designed to match the two-photon action cross-section of commercially available biological dyes. This condition offers the advantage that very low average and corresponding peak powers can still be used to image living biological specimens, thus relaxing the required intensities to image the samples enabling for an increased viability and a reduced specimen photo-damage.

References

1. U. Keller, "Recent developments in compact ultrafast lasers," Nature **424**, 831-838 (2003).

2. U. Keller, "Ultrafast solid-state laser oscillators: a success story for the last 20 years with no end in sight," Applied Physics B-Lasers and Optics **100**, 15-28 (2010).

3. D. Kopf, K. J. Weingarten, L. R. Brovelli, M. Kamp, and U. Keller, "Diode-pumped 100-fs passively mode-locked cr-lisaf laser with an antiresonant fabry-perot saturable absorber," Optics Letters **19**, 2143-2145 (1994).

4. D. Kopf, K. J. Weingarten, G. Zhang, M. Moser, M. A. Emanuel, R. J. Beach, J. A. Skidmore, and U. Keller, "High-average-power diode-pumped femtosecond Cr:LiSAF lasers," Applied Physics B-Lasers and Optics **65**, 235-243 (1997).

5. D. Kopf, G. Zhang, R. Fluck, M. Moser, and U. Keller, "All-in-one dispersion-compensating saturable absorber mirror for compact femtosecond laser sources," Optics Letters **21**, 486-488 (1996).

6. K. Svoboda, W. Denk, W. H. Knox, and S. Tsuda, "Two-photon-excitation scanning microscopy of living neurons with a saturable Bragg reflector mode-locked diode-pumped Cr:LiSrAlFl laser," Optics Letters **21**, 1411-1413 (1996).

7. J. M. Girkin, and G. McConnell, "Advances in laser sources for confocal and multiphoton microscopy," Microscopy Research and Technique **67**, 8-14 (2005).

8. S. Sakadzic, U. Demirbas, T. R. Mempel, A. Moore, S. Ruvinskaya, D. A. Boas, A. Sennaroglu, F. X. Kartner, and J. G. Fujimoto, "Multi-photon microscopy with a low-cost and highly efficient Cr:LiCAF laser," Optics Express **16**, 20848-20863 (2008).

9. G. Robertson, D. Armstrong, M. J. P. Dymott, A. I. Ferguson, and G. L. Hogg, "Two-photon fluorescence microscopy with a diode-pumped Cr:LiSAF laser," Applied Optics **36**, 2481-2483 (1997).

10. R. Aviles-Espinosa, S. Santos, A. Brodschelm, W. G. Kaenders, C. Alonso-Ortega, D. Artigas, and P. Loza-Alvarez, "Third-harmonic generation for the study of Caenorhabditis elegans embryogenesis," Journal of Biomedical Optics **15** (2010).

11. S. Tang, J. Liu, T. B. Krasieva, Z. P. Chen, and B. J. Tromberg, "Developing compact multiphoton systems using femtosecond fiber lasers," Journal of Biomedical Optics **14** (2009).

12. A. C. Millard, P. W. Wiseman, D. N. Fittinghoff, K. R. Wilson, J. A. Squier, and M. Muller, "Third-harmonic generation microscopy by use of a compact, femtosecond fiber laser source," Applied Optics **38**, 7393-7397 (1999).

13. M. Kuramoto, N. Kitajima, H. C. Guo, Y. Furushima, M. Ikeda, and H. Yokoyama, "Two-photon fluorescence bioimaging with an all-semiconductor laser picosecond pulse source," Optics Letters **32**, 2726-2728 (2007).

14. K. Taira, T. Hashimoto, and H. Yokoyama, "Two-photon fluorescence imaging with a pulse source based on a 980-nm gain-switched laser diode," Optics Express **15**, 2454-2458 (2007).

15. H. Yokoyama, H. C. Guo, T. Yoda, K. Takashima, K. Sato, H. Taniguchi, and H. Ito, "Two-photon bioimaging with picosecond optical pulses from a semiconductor laser," Optics Express **14**, 3467-3471 (2006).

16. H. J. Koester, D. Baur, R. Uhl, and S. W. Hell, "Ca2+ fluorescence imaging with pico- and femtosecond two-photon excitation: Signal and photodamage," Biophysical Journal **77**, 2226-2236 (1999).

17. K. Konig, T. W. Becker, P. Fischer, I. Riemann, and K. J. Halbhuber, "Pulse-length dependence of cellular response to intense near-infrared laser pulses in multiphoton microscopes," Optics Letters **24**, 113-115 (1999).

18. Y. Ding, R. Aviles-Espinosa, M. A. Cataluna, D. Nikitichev, M. Ruiz, M. Tran, Y. Robert, A. Kapsalis, H. Simos, C. Mesaritakis, T. Xu, P. Bardella, M. Rossetti, I. Krestnikov, D. Livshits, I. Montrosset, D. Syvridis, M. Krakowski, P. Loza-Alvarez, and E. Rafailov, "High peak-power picosecond pulse generation at 1.26 mu m using a quantum-dot-based external-cavity mode-locked laser and tapered optical amplifier," Optics Express **20**, 14308-14320 (2012).

19. R. Aviles-Espinosa, G. Filippidis, C. Hamilton, G. Malcolm, K. J. Weingarten, T. Suedmeyer, Y. Barbarin, U. Keller, S. I. C. O. Santos, D. Artigas, and P. Loza-Alvarez, "Compact ultrafast semiconductor disk laser: targeting GFP based nonlinear applications in living organisms," Biomedical Optics Express **2**, 739-747 (2011).

20. M. Drobizhev, N. S. Makarov, S. E. Tillo, T. E. Hughes, and A. Rebane, "Two-photon absorption properties of fluorescent proteins," Nature Methods **8**, 393-399 (2011).

21. U. Keller, and A. C. Tropper, "Passively modelocked surface-emitting semiconductor lasers," Physics Reports-Review Section of Physics Letters **429**, 67-120 (2006).

22. A. McWilliam, A. A. Lagatsky, C. T. A. Brown, W. Sibbett, A. E. Zhukov, V. M. Ustinov, A. P. Vasil'ev, and E. U. Rafailov, "Quantum-dot-based saturable absorber for femtosecond mode-locked operation of a solid-state laser," Optics Letters **31**, 1444-1446 (2006).

23. U. Keller, K. J. Weingarten, F. X. Kartner, D. Kopf, B. Braun, I. D. Jung, R. Fluck, C. Honninger, N. Matuschek, and J. A. derAu, "Semiconductor saturable absorber mirrors (SESAM's) for femtosecond to nanosecond pulse generation in solid-state lasers," IEEE Journal of Selected Topics in Quantum Electronics **2**, 435-453 (1996).

24. D. Maas, A. R. Bellancourt, M. Hoffmann, B. Rudin, Y. Barbarin, M. Golling, T. Sudmeyer, and U. Keller, "Growth parameter optimization for fast quantum dot SESAMs," Optics Express **16**, 18646-18656 (2008).

25. C. Xu, W. Zipfel, J. B. Shear, R. M. Williams, and W. W. Webb, "Multiphoton fluorescence excitation: New spectral windows for biological nonlinear microscopy," Proceedings of the National Academy of Sciences of the United States of America **93**, 10763-10768 (1996).

26. E. Spiess, F. Bestvater, A. Heckel-Pompey, K. Toth, M. Hacker, G. Stobrawa, T. Feurer, C. Wotzlaw, U. Berchner-Pfannschmidt, T. Porwol, and H. Acker, "Two-photon excitation and emission spectra of the green fluorescent protein variants ECFP, EGFP and EYFP," Journal of Microscopy-Oxford **217**, 200-204 (2005).

27. G. A. Blab, P. H. M. Lommerse, L. Cognet, G. S. Harms, and T. Schmidt, "Two-photon excitation action cross-sections of the autofluorescent proteins," Chemical Physics Letters **350**, 71-77 (2001).

28. R. Heim, A. B. Cubitt, and R. Y. Tsien, "IMPROVED GREEN FLUORESCENCE," Nature **373**, 663-664 (1995).

29. Developmental Recourse for Biophysical Imaging Optoelectronics, “Two photon action cross sections” (Cornel University, 2010), http://www.drbio.cornell.edu/cross_sections.html.

30. Education in Microscopy and Digital Imaging, “Suitable dyes for multi-photon” (Zeiss virtual campus 2011), http://www.zeiss.com/C12567BE00472A5C/EmbedTitelIntern/MultiphotonSuitableDyes/$File/MultiphotonSuitableDyes.pdf

31. S. Psilodimitrakopoulos, V. Petegnief, G. Soria, I. Amat-Roldan, D. Artigas, A. M. Planas, and P. Loza-Alvarez, "Estimation of the effective orientation of the SHG source in primary cortical neurons," Optics Express **17**, 14418-14425 (2009).

32. T. R. Neu, U. Kuhlicke, and J. R. Lawrence, "Assessment of fluorochromes for two-photon laser scanning microscopy of biofilms," Applied and Environmental Microbiology **68**, 901-909 (2002).

33. B. J. Baker, H. Mutoh, D. Dimitrov, W. Akemann, A. Perron, Y. Iwamoto, L. Jin, L. B. Cohen, E. Y. Isacoff, V. A. Pieribone, T. Hughes, and T. Knopfel, "Genetically encoded fluorescent sensors of membrane potential," Brain Cell Biology **36**, 53-67 (2008).

34. A. Khatchatouriants, A. Lewis, Z. Rothman, L. Loew, and M. Treinin, "GFP is a selective non-linear optical sensor of electrophysiological processes in Caenorhabditis elegans," Biophysical Journal **79**, 2345-2352 (2000).

35. J. White, and E. Stelzer, "Photobleaching GFP reveals protein dynamics inside live cells," Trends in Cell Biology **9**, 61-65 (1999).

36. E. U. Rafailov, M. A. Cataluna, and W. Sibbett, "Mode-locked quantum-dot lasers," Nature Photonics **1**, 395-401 (2007).

37. X. D. Huang, A. Stintz, H. Li, L. F. Lester, J. Cheng, and K. J. Malloy, "Passive mode-locking in 1.3 mu m two-section InAs quantum dot lasers," Applied Physics Letters **78**, 2825-2827 (2001).

38. E. U. Rafailov, M. A. Cataluna, W. Sibbett, N. D. Il'inskaya, Y. M. Zadiranov, A. E. Zhukov, V. M. Ustinov, D. A. Livshits, A. R. Kovsh, and N. N. Ledentsov, "High-power picosecond and femtosecond pulse generation from a two-section mode-locked quantum-dot laser," Applied Physics Letters **87** (2005).

39. M. G. Thompson, A. R. Rae, M. Xia, R. V. Penty, and I. H. White, "InGaAs Quantum-Dot Mode-Locked Laser Diodes," Ieee Journal of Selected Topics in Quantum Electronics **15**, 661-672 (2009).

40. M. A. Cataluna, Y. Ding, D. I. Nikitichev, K. A. Fedorova, and E. U. Rafailov, "High-Power Versatile Picosecond Pulse Generation from Mode-Locked Quantum-Dot Laser Diodes," Ieee Journal of Selected Topics in Quantum Electronics **17**, 1302-1310 (2011).

41. D. Kobat, M. E. Durst, N. Nishimura, A. W. Wong, C. B. Schaffer, and C. Xu, "Deep tissue multiphoton microscopy using longer wavelength excitation," Optics Express **17**, 13354-13364 (2009).

42. I. H. Chen, S. W. Chu, C. K. Sun, P. C. Cheng, and B. L. Lin, "Wavelength dependent damage in biological multi-photon confocal microscopy: A micro-spectroscopic comparison between femtosecond Ti : sapphire and Cr : forsterite laser sources," Optical and Quantum Electronics **34**, 1251-1266 (2002).

43. M. C. Chan, T. M. Liu, S. P. Tai, and C. K. Sun, "Compact fiber-delivered Cr : forsterite laser for nonlinear light microscopy," Journal of Biomedical Optics **10** (2005).

44. W.-J. Lee, C.-F. Lee, S.-Y. Chen, Y.-S. Chen, and C.-K. Sun, "Virtual biopsy of rat tympanic membrane using higher harmonic generation microscopy," Journal of Biomedical Optics **15** (2010).

45. T. W. Berg, and J. Mork, "Saturation and noise properties of quantum-dot optical amplifiers," Ieee Journal of Quantum Electronics **40**, 1527-1539 (2004).

46. Y. Ding, M. A. Cataluna, D. Nikitichev, I. Krestnikov, D. Livshits, and E. Rafailov, "Broad Repetition-Rate Tunable Quantum-Dot External-Cavity Passively Mode-Locked Laser with Extremely Narrow Radio Frequency Linewidth," Applied Physics Express **4** (2011).

47. Y. Ding, D. I. Nikitichev, I. Krestnikov, D. Livshits, M. A. Cataluna, and E. U. Rafailov, "Fundamental and harmonic mode-locking with pulse repetition rate between 200 MHz and 6.8 GHz in a quantum-dot external cavity laser," in Lasers and Electro-Optics Europe (CLEO EUROPE/EQEC), 2011 Conference on and 12th European Quantum Electronics Conference, (Munich, Germany, 2011), p. CF_P23.

48. M. Xia, M. G. Thompson, R. V. Penty, and I. H. White, "External-Cavity Mode-Locked Quantum-Dot Laser Diodes for Low Repetition Rate, Sub-Picosecond Pulse Generation," Ieee Journal of Selected Topics in Quantum Electronics **17**, 1264-1271 (2011).

Chapter 4

Adapting the NL microscope for enhanced sample imaging

In the previously presented chapters, I have shown two different strategies to push forward the limits of nonlinear microscopy (NLM). These were based on the exploitation of label-free techniques for generating contrast and in the use of novel laser devices designed for nonlinear (NL) imaging. All the advantages of each strategy were presented. However, in both cases, aberrations appear as a fundamental problem that limits the efficiency of the NL excitation for producing two-photon excited fluorescence (TPEF), second harmonic generation (SHG) or third harmonic generation (THG) images. Aberrations deteriorate the focused beam reducing its intensity. This is particularly important if long penetration depths, one of the main advantages of NLM, are to be reached. Therefore, in this chapter, I will present a strategy to compensate, not only for the aberrations induced along the beam path formed by the different optical elements, but also for those caused inside the sample. The results presented in this section will also enable understanding how to deal with some of the effects encountered in the previous chapters such as reducing the aberrations for implementing a faster scanning strategy, and the possibility to image deeper inside the sample (see chapter 2).

To get started with the strategy developed in this chapter, it is important to go through the main advantages of NLM and then understand how these imaging devices can be affected by the presence of aberrations. I will then give a quick outlook of the different techniques and implementations to overcome aberration effects. Based on the limitations of the state of the art techniques for aberrations correction, the strategy and results obtained in this thesis will be presented.

As it has been discussed in the introduction chapter, NLM has several inherent advantages in contrast with confocal laser scanning microscopy. These are intrinsic optical sectioning, reduced out of focus photo-damage, larger penetration depths etc. This has allowed the technique to become an important tool in biology [1]. Although this technique allows larger penetration depths compared with confocal microscopy (based on the use of infra red (IR) wavelengths), aberration effects and scattering limit the full exploitation of its imaging capabilities. Aberrations lead to a spreading of the focusing spot inside the sample, both in axial and lateral directions, reducing the resolution and the intensity. As a consequence, the contrast of the imaged sample drops drastically [2-4]. As it has already been discussed (see chapter 1), aberrations in a microscope are not only caused by the intrinsic optical elements quality and alignment, but also by the refractive index mismatch from the objective,

immersion media, cover-glass, and more importantly, by the inhomogeneous structure of biological samples [5]. In addition, when imaging inside semi-transparent samples, the image quality is weakly affected by scattering up to a depth of several scattering lengths [6].

To deal with these problems, microscopists are starting to adopt different Adaptive Optics (AO) sensing schemes to correct the aberrated wavefronts (WFs). Such WFs can be corrected in the excitation beam [7], in the collected signal beam or in both depending on the employed microscopy technique. For example, in wide field techniques such as PALM or STORM, only the correction of the collected signal is important in order to maintain the contrast of the acquired images [8]. In confocal microscopy, both the excitation and collected beams need to be compensated to improve the intensity of the reconstructed images [9, 10]. In NLM, there is no need to correct on the collected beam as no confocal aperture is required. However, correcting the excitation beam is a must as this will ensure a better focusing and therefore, a more efficient NL process.

In practice, measuring and correcting the excitation beam aberrations at the sample plane of a nonlinear microscope is a difficult task. Nevertheless, some strategies to do this have already been implemented. These strategies can be divided into sensor-based and sensor-less techniques.

In sensor-less schemes, iterative algorithms are generally used to control a deformable mirror (DM) or a Spatial Light Modulator [11, 12]. Optimization is performed by improving a merit function based on an image-quality related parameter, such as the total intensity within the imaged area [13, 14]. This implies that the sample must be imaged several times until the employed algorithm is able to find a solution. The success of the algorithm is dependent on the initial guess of the optimization process, the employed algorithm (genetic, modal, etc.), and the stopping criteria. This process enables to compensate the aberrations without having to measure them. Although the use of optimized algorithms that reduce sample exposure have been reported [6, 15], this still implies that an area of interest within the sample has to be exposed a considerable number of times. This may result in unwanted exposure which is prone to produce photo-bleaching and photo-toxic effects on the sample [16].

In sensor-based schemes optical aberration measurements can be performed through a sensing device such as a wavefront sensor (WFS) or an interferometer [5, 17, 18]. This information is then sent to an adaptive element to compensate for such aberrations. The standard implementation of this technique, when used for microscopy applications, suffers from important drawbacks. Collecting the excitation beam in forward direction requires careful consideration: first, because the upper layers of the sample will produce aberrations that might interfere with the measurement if the lower layers are being corrected, and second because an additional lens with the same or higher numerical aperture (NA) than the used microscope objective must be introduced into the setup. In this case, the optical quality and alignment of this element with the optical axis may induce undesirable aberrations that must

be calibrated. In a backward configuration the backscattered excitation signal (normally collected in double pass scheme) has the same intensity level as the spurious reflections, making it difficult to distinguish between these two [10, 18, 19].

Despite that, sensor based schemes are powerful techniques as WF aberrations are directly obtained. Thus, alternative solutions can be considered. Interferometric methods or confocal depth selection mechanisms have been successfully applied for a direct WF measurement. These principles have proved to work well as they enable to filter/select the excitation beam at the imaged focal plane [10, 20]. However, they work only in thick and highly scattering samples [10] or rely on complex experimental setups [18].

As a result other methodologies, similar to those already used in astronomy, have been implemented. In particular AO has been broadly used in astronomy to compensate for the changing turbulent medium in the atmosphere which produces aberrations and deteriorates the image of objects to be observed. By employing a WFS it is possible to measure the distortions produced when distant light sources travel through the changing atmosphere, employing a reference point source called guide star. This can be a natural star or a laser producing fluorescence in the atmosphere [21]. Then such information is fed to a DM, in order to restore the image quality.

The above principle has been applied for moderate scattering samples imaged through linear fluorescence microscopy. This method consists of artificially inserting a small secondary light source (i.e. a fluorescent bead) inside the sample [22] which is fixed after its preparation. This allows for a direct measurement of the sample aberrations using a Shack-Hartmann (SH) WFS, therefore allowing the correction of the aberrations.

However, since this technique is based on the introduction of beads inside the sample by using a microinjection needle or negative pressure protocols [22], it is prone to cause sample damage, limiting its potential for *in vivo* imaging studies. Besides, this, beads are randomly distributed inside the fixed sample, therefore a suitable bead placed at the right location should be found in the field of view (FOV) and for each depth to be imaged. This adds complexity as sample preparation is required for the aberration measurement process.

In this chapter I will present an analysis of the interaction between the light source with the coupling optics and the biological sample. This will be divided in two parts. The first part will cover the interaction of the light source with the coupling optics, tube lens and conjugation lens. A detailed analysis of the effects caused to light passing through different reflective and transmissive elements will be described. These results will enable understanding how to adapt the optical system (NL microscope), to achieve an enhanced light interaction without having to worry about the distortions produced by the employed coupling elements.

In the second part the interaction of light with the microscope objective, immersion fluid, cover-glass and different samples will be analyzed. This will be carried out introducing a simple and non invasive methodology developed in this thesis work, called the "Non Linear-Guide Star" (NL-GS) concept. This methodology was proposed considering the difficulties of employing a direct way to understand the changes caused to the light as it interacts with the sample causing optical aberrations on the excitation beam (as mentioned before). This concept will be explained in detail together with the experiments performed to validate it and the considerations to be taken when applying such methodology.

Both independent characterizations will be analyzed first and then merged in a strategy to adapt the microscope to achieve a more efficient interaction with both the coupling optics and the sample. This strategy will enable to push the imaging performance of the developed NLM work station towards its limits. This is demonstrated using both *in vitro* and *in vivo* biological samples in which the enhancement of the corrected images, when compared with the non-corrected ones, results in an improvement of more than one order of magnitude in the total collected signal intensity.

4.1. Adaptive optics system implementation

In this section the developed NLM work station was prepared for aberrations correction by implementing an AO system. The integration of such technology into the NLM workstation was carried out in a similar approach to the one described on section 2.1 (i.e. considering the Titanium:Sapphire (Ti:S) beam diameter and the microscope objective to be used, the DM pupil size and height etc.). The microscope setup existing lenses where kept (L3 and L6, see figure 4.1) however the mirror used to reflect the light form the galvanometric mirrors to the microscope input was changed for a flip mirror.

To perform the aberrations correction, an electromagnetic DM (Imagine Optic, France, mirao 52-e), with a ±50 μm peak to valley WF amplitude stroke, was used. This device has a reflective membrane that can be deformed electromagnetically by applying control voltages to the actuators that are fixed on its back side. The shape of the mirror depends on the combination of forces applied to the membrane.

To have an efficient performance of the AO system, the pupil size of each optical element was considered. The DM has a pupil size of 15 mm in diameter and microscope objective has an input pupil diameter around 8 mm. The requirement is to use all the actuators in the DM active area and the full NA of the microscope objective. Therefore, the optical path was built keeping in mind that the laser output had a 1 mm diameter (measured using the WFS) and that this was expanded and collimated using a first telescope (LI and L2) thus having a 2 mm beam size that travelled all the way until the galvanometric mirrors.

Taking into account such conditions, the lens that was already placed in the microscopy setup (L3), the available space in the optical table, and the pupil size of the DM, L4 was selected to

enable filling the full DM active area. Now the beam has to be reduced again to take advantage of the full NA of the microscope objective, therefore L5 was selected to preserve the existing lens L6. Figure 4.1 shows the real setup placed on the optical table.

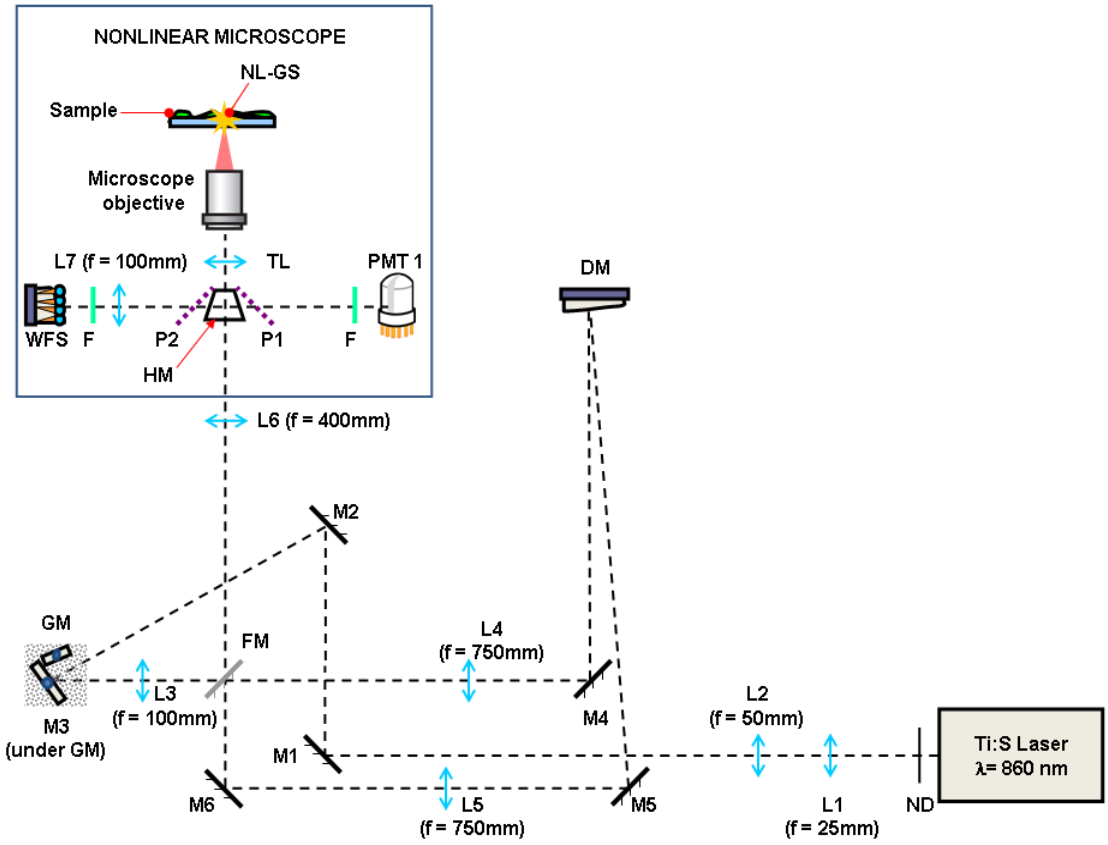

Figure: 4.1. Schematic experimental setup used for aberration measurements and wavefront correction. Ti:S is the Ti:Sapphire laser; ND, Neutral density filter; L#, lenses; M#, mirrors; GM are the galvanometric mirrors; FM, is the flip mirror; DM is the deformable mirror; HM is a dichroic filter; TL is the microscope tube lens; NL-GS is the nonlinear guide-star; P# microscope ports; F is BG39 filter; WFS is the wavefront sensor, and PMT is the photo multiplier tube. The microscope output port is manually selected either for the PMT or for the WF sensor. The DM, was placed as close to normal incidence as the optics mounts allow it for optimum actuator usage.

For the alignment of the added part of the setup, the flip mirror was employed to enable using the AO setup.

To determine the DM position an IR viewer was employed. In this step it is important to conjugate the pupil of the galvanometric mirror with the DM and the microscope objective. Then, the DM was placed considering the previous condition plus an additional one. To fulfill the first condition, the DM was placed in the position where the scanned beam does not displace, meaning that the optimum conjugation position has been achieved. The second one is that the DM, should be placed as close to normal incidence as the optics mounts from mirrors M4 and M5 allow it, to enable having an optimum DM actuator usage.

Finally, the WFS was placed at one of the microscope output ports. This was carried out to take advantage of the existing optical elements in the microscope such as the tube lens. In this way only an additional lens was employed to conjugate the objective entrance pupil with the micro-lens array of the WFS. This enabled to perform WF measurements which were used to characterize the static aberrations of the microscope and the sample induced aberrations. This will be described in the next subchapters.

4.2. Microscopy work station static aberrations characterization

In this section the characterization of all the aberrations in the microscope optical path caused due to the intrinsic optical elements quality and alignment will be analyzed. This was carried out by studding the accumulated effects produced by all the cascaded optical elements forming the optical path. As the light is coupled into the microscope using such elements the aberrations in this part of the setup were called “Coupling aberrations”. Therefore, the aberrations in the NLM workstation are caused by the laser, the optical elements such as neutral density (ND) filters, lenses, mirrors, dichroic filter, the tube lens and the WFS conjugation lens. Such aberrations can be measured in a single step as these are modified trough all the optical path until the last optical element before the measurement is taken.

For this purpose, a HASO3 32 (Imagine Optic, France) Shack-Hartmann wave front sensor was used. The sensor operation principle is based on the concept of measuring the displacement of a spot pattern relative to a pre-calibrated one (i.e. for having a flat wavefront). This spot pattern is created by passing the incoming beam through a micro lens array that focuses the beam towards a charge-coupled device (CCD) array. The difference between the measured pattern and the pre-calibrated pattern is used to approximate the incoming WF. Figure 4.2 shows the concept.

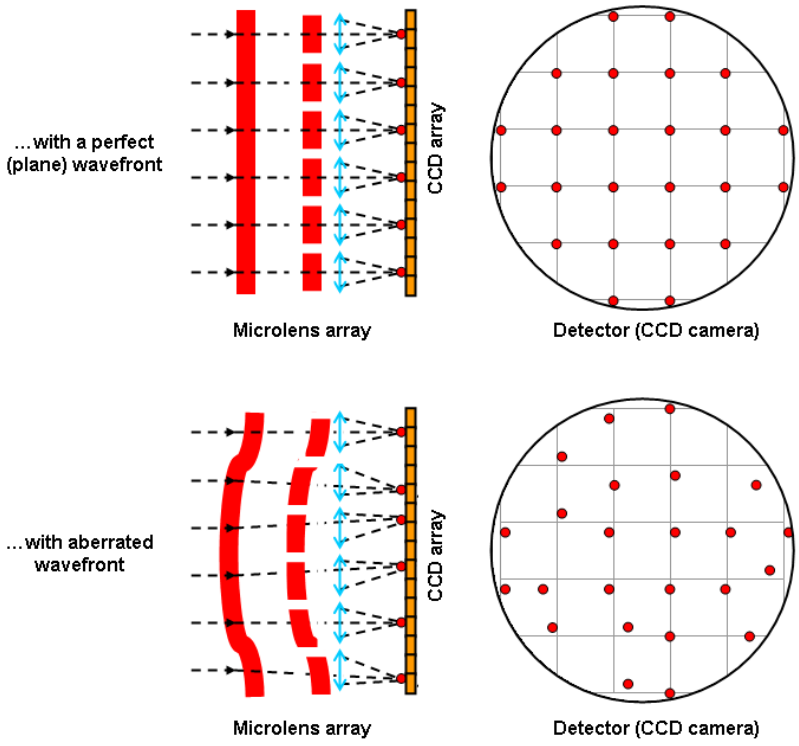

Figure: 4.2. Top panel is the schematic representation of a Shack-Hartmann wave front sensor acquiring a plane WF. The bottom panel depicts the case when an incoming aberrated WF is sensed.

The first step was to develop a compatible strategy to use the WFS in a simple configuration and location of the microscope as explained in the previous section. This study was carried out employing the Ti:S laser system coupled into de microscope (see figure 4.1). This laser source was selected because it is able to deliver enough peak power into the sample plane which will be required in the aberrations correction step as the beam will pass through additional optical elements.

Once the WFS was correctly aligned and the appropriate lenses were placed to have a reliable measurement, the laser beam was attenuated using the ND filter wheel to avoid damaging the sensing device. Then, the measurement was carried out by carefully adjusting its acquisition parameters using the WFS software.

From figure 4.3 it is possible to observe that the main sources of aberration in this part of the setup are astigmatism at 0º and 45º (Zernike coefficients 4 and 5 having values of -2.1 and -2.4 µm respectively).

After performing these experiments several times it was concluded that these aberrations are produced mainly by the optics inside the laser source. This conclusion was reached because between the preliminary measurements and the results presented in figure 4.3 the laser had to be completely switched off (due to electrical maintenance tasks at the whole ICFO building)

which involves changing the conditions inside the laser cavity (i.e. cooling and heating up the laser crystal). Comparing the preliminary measurements to what can be observed in figure 4.3 the values of astigmatism had a 10 % difference (data not shown).

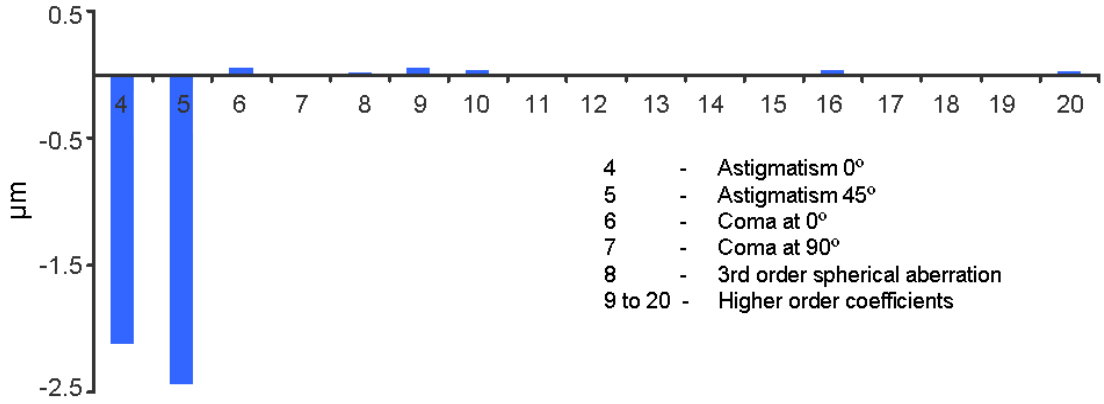

Figure: 4.3. Measured Zernike coefficients showing the accumulated effects produced by all the cascaded optical elements forming the optical path in the nonlinear microscopy work station ("Coupling aberrations").

If the laser is always set into standby mode, the conditions inside the laser cavity will remain almost constant therefore negligible changes in the recorded Zernike values were observed as a function of time.

These measurements enable to get the overall aberration effects caused by the static elements in the microscope optical setup. These aberrations behave in a static fashion as the elements do not have to be moved once the setup is built and aligned. This means that the information obtained in this characterization can be used to calibrate the system aberrations. Once this correction step is performed, it will be possible to proceed with the coupling aberrations correction. This will be further discussed in sub chapter 4.4.

4.3. The nonlinear-guidestar concept for sample aberrations characterization

In order to reduce specimen damage effects, for achieving a fast aberration correction. It is required to measure the sample induced aberrations. Firstly because, as it has been mentioned, current implementations are based on time consuming methodologies consisting on trial and error methodologies. Secondly because theoretical models cannot predict what happens inside an heterogeneous environment such as a biological sample which can be composed of different structures having a complex variation on its refractive indices.

In this subsection, the NL-GS concept will be explained in greater detail. Together with its application to measure the aberrations originated by the elements that are usually changed in every experiment such as the microscope objective, the immersion fluid, the cover-glasses and more importantly, those coming from inside the sample. For practical purposes, these

aberrations will be called “focusing aberrations”. The description of the obtained results will start by demonstrating that the NL-GS emission is independent from the excitation beam aberrations.

A SH WFS requires a point source to perform WF measurements. In this case, such point source will be given by the NL-GS. As it has been explained in the introduction chapter, TPEF naturally produces a small confined focal volume which can be used as an incoherent secondary light source. Thus in this strategy it is shown how this point source, the NL-GS, can be used in a practical and noninvasive way for single pass measurements of sample and objective aberrations in the NLM workstation using a SH WFS sensor. In this sense it will be demonstrated that the focal volume created inside the sample due to the NL excitation effect (TPEF emission) behaves as a point source, and therefore is suitable to be used in combination with the employed WFS. This will be followed by determining the optimum amount of measurements that should be taken for a given FOV taking on-axis and off-axis measurements. A comparison between on-axis vs. off-axis measurements will be presented at different depths. These measurements will be compared against a theoretical model that describes the evolution of depth induced aberrations using homogeneous samples.

For this part of the work, five fluorescent test-samples were used. The first two consisted of conventional red and orange water paint in water solution [23, 24] applied onto a 170 μm thickness cover-glass (EMS, Hatfield, Pennsylvania, USA). The dried samples had a final average thickness of ~40 μm. These were placed directly at the sample plane of the microscope. The emitted fluorescent spectrum from both test samples had a bandwidth of 40 nm (measured at the full width half maximum) centered at 550 and 600 nm, respectively.

The next two test-samples consisted of 1 μm and 0.28 μm diameter fluorescent microspheres (Duke Scientific Palo Alto, California USA) in water solution sandwiched between two cover-glasses. The emitted fluorescent spectrum was centered at 508 nm.

Finally the last test sample consisted of 1 μm diameter fluorescent microspheres (Duke Scientific, USA) dried at the bottom of a glass Petri-dish (MatTek corporation, USA, P50G-1.5-14-F), then 40 μl of beads in a concentration of 1:1000 were embedded in 120 μl of 2% agarose gel (Scharlab, Spain, AG00200500). A drop of this preparation was then placed on top of the cover-glass.

As before, the measurements were performed having the WFS located at one of the microscope output ports. A filter cube, containing a short pass dichroic filter (Chroma, Bellows falls, Vermont, USA, 750dcspxr, transmittance: 440-720nm, reflectance: 800-900nm) and a BG39 band pass filter (Schott, Germany, transmittance: 320-720nm) were used to separate the excitation beam from the generated TPEF signal. A 60x oil immersion microscope objective with numerical aperture (NA) = 1.4, (Plan Apo, Nikon, Japan) was used. Such objective possesses a high NA limited only by the refractive index of the sample.

As the WFS (that is based on a standard CCD camera) sensitivity is less than a few nanojoules, the integration time needed to measure such WF was adjusted between 0.5 s and 1 s.

In order to extend the guide star concept for microscopy applications, a key point not properly appreciated in state of the art works [22, 25, 26] is that fluorescence, being an incoherent process, does not contain information about the aberrations gained by the excitation beam. Therefore, it allows for the implementation of single pass aberration measurement schemes. To test this, the excitation beam was first parked at the desired region of the sample to generate the TPEF signal (i.e. the NL-GS). As stated before, this emission, being an incoherent process, does not retain the aberrations of the excitation beam, and therefore it can be used to measure focusing aberrations.

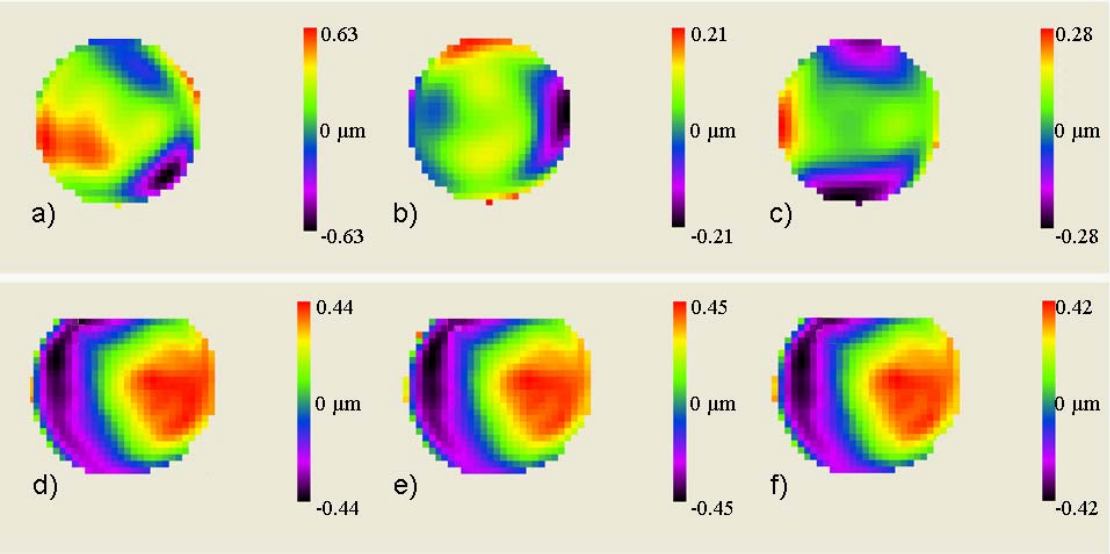

Figure: 4.4.(a, b, c) three different WFs of the excitation beam showing an RMS variation of a 70% (0.079 µm to 0.261 µm RMS) and (d, e, f) their corresponding generated WFs measured using the SH WFS. The measured NL-GS WF is similar in all three cases, with a maximum wavefront error variation of 7% (from 0.252µm to 0.271µm RMS). The planes (tilts) and spherical (focus) components of the WFs have been removed.

To do this, the DM was arbitrarily shaped to change the WF of the excitation beam while observing the TPEF of the red-paint test sample. The WFs of the excitation beam are displayed in Figures 4.4(a-c) where a root mean square (RMS) variation of 70% (from 0.079 µm to 0.261 µm RMS) can be observed for the three different cases. As expected, this change of illumination conditions produced similar NL-GS WFs (see Figures 4.4d-f) having a dispersion of only a 7% on its RMS value (from 0.252 µm to 0.271µm RMS). The only difference that could be observed is a variation of the generated NL-GS brightness (the lower the aberration, the higher the collected signal). This shows that the NL-GS is both, reproducible, reliable and independent from the excitation beam aberrations.

The next step was to verify that a NL-GS behaves as point source, enabling the WF measurement inside a sample using the SH WFS. To do that the WF generated by a NL-GS, (i.e., from the point spread function generated by the TPEF volume, inside the red-paint) was compared with the generated WF produced by a physical point source such as a fluorescent spherical bead of i) 1 μm and ii) 0.28 μm in diameter. All three samples were placed in the same substrate in order to preserve the same experimental conditions, thus enabling to switch between samples by only changing the cover-glass lateral position. The measured WF maps are shown in Figure 4.5.

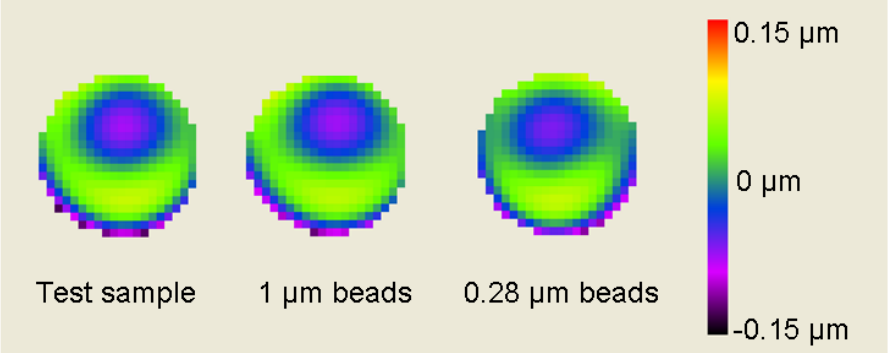

Figure: 4.5. Recorded wavefront maps of three different WFs generated from i) NL-GS produced inside the red-paint test-sample, ii) from 1 μm radii fluorescent beads, and iii) 0.28 μm radii fluorescent beads. The RMS values are 0.042, 0.040, and 0.037 μm, respectively. The planes (tilts) and spherical (focus) components of the WFs have been removed.

The resulting RMS wavefront error (WFE) is similar for the three cases having an average dispersion of 8%, indicating that the WF measured by the NL-GS is not affected by the fact of having a confined focal volume created by the NL effect. Finally, the Zernike coefficient analysis in this case showed that in the three samples, the dominant aberration is coma at 90°.

Continuing with the NL-GS principle validation, the third step was to measure the isoplanatic patch first in in a thin sample to get rid of sample induced aberrations. This effect is described in astronomy by the isoplanatic angle which describes the maximum allowable displacement between the location of the natural guide-star and the real object to be imaged [21]. Usually aberrations are more efficiently corrected near the region where the measurement is taken in comparison with the surrounding areas. This can be verified taking advantage of the fact that the NL-GS can be placed in the exact location where the correction is required. In particular, for this experiment the WF of 9 NL-GSs was recorded, one on-axis and the remaining ones at equidistant positions of ~17.9 μm apart from the center (the complete FOV for this experiment was of ~ 44.8 μm). This was performed using both paint test samples and considering two different regions on each sample in order to test the repeatability of the results. Figure 4.6 is an example of the WF maps recorded (results depicted for the orange-paint test-sample).

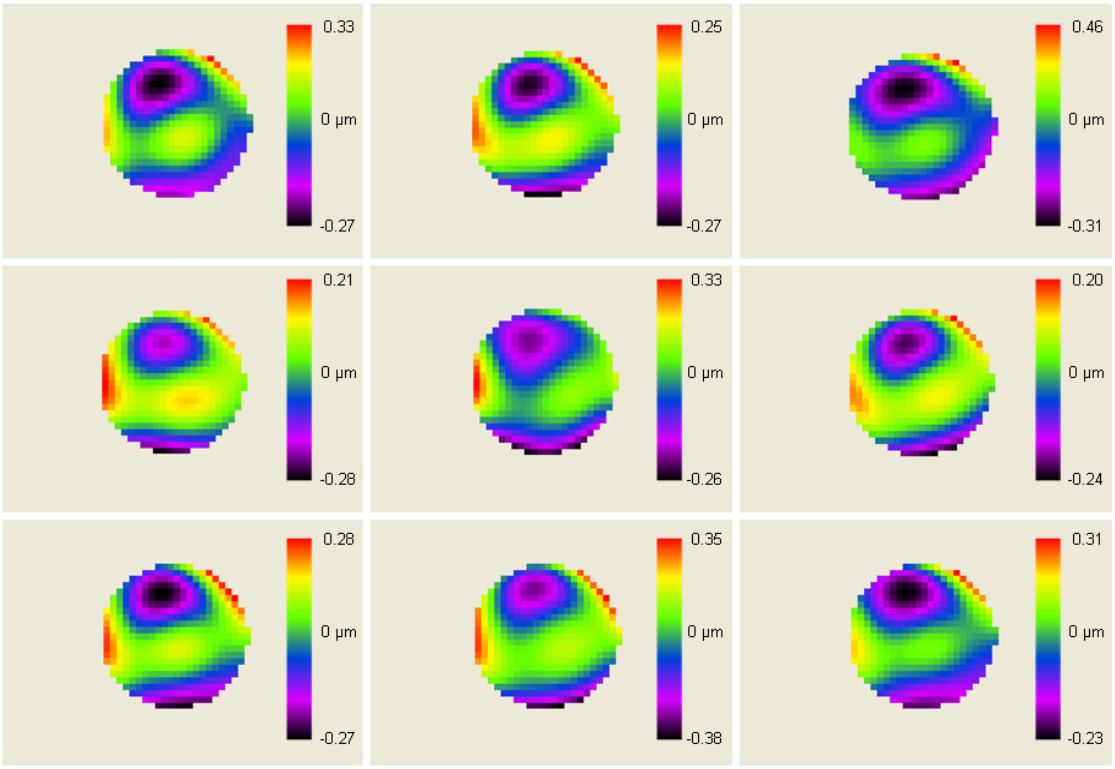

Figure: 4.6. Recorded off-axis NL-GS at 8 equidistant locations from the on-axis position (average RMS WFE is ~0.120 µm). The 8 recorded positions were ~17.9 µm apart from the center (on-axis RMS WFE is ~0.114 µm). The FOV for this experiment was ~44.8µm. The planes (tilts) and spherical (focus) components of the WFs have been removed.

All the measurement trials demonstrated that even if the immersion fluid, cover-glass and sample region, are changed, the aberrations are similar in the entire FOV. This is consistent with the quality of the employed microscope.

To further assess the performance of the proposed methodology at different depths, a comparison between on-axis vs. off-axis measurements was carried out. This was performed to study the aberration effects produced by the sample at different depths. These measurements were compared with a theoretical model that describes the evolution of depth induced aberrations in homogeneous samples (i.e. the test samples employed in this case).

In what follows, the WF was measured as a function of depth. In the past, image analysis techniques have intended to describe the fluorescent signal as a function of depth [27]. This has been done by analyzing the fluorescence intensity at the central and peripheral regions of thin samples, instead of measuring aberrations.

The measurements using the NL-GS were carried out using the last sample containing beads suspended in agarose gel at different depths.

The FOV for this experiment was ~75 µm. Five measurements were performed at the on-axis position for different beads at depths of 10, 50 and 100 µm inside the sample. Then five additional measurements were taken for each of the 4 corners of the FOV. These were separated approximately ~35 µm from the on-axis measurement which is almost twice the distance employed in the previous experiment. This was carried out to represent sample features positioned as far as possible from the optical axis.

The procedure was repeated for each depth. Examples of the measured WFs at the specified depths are shown in figure 4.7 (left panel is the off-axis measurements, middle panel is the on-axis measurements and the right panel shows the elongation of the point spread function as a function of depth). From these results, it can be confirmed that the evolution of the WFE as a function of depth has a similar behavior for both cases (off-axis and on-axis).

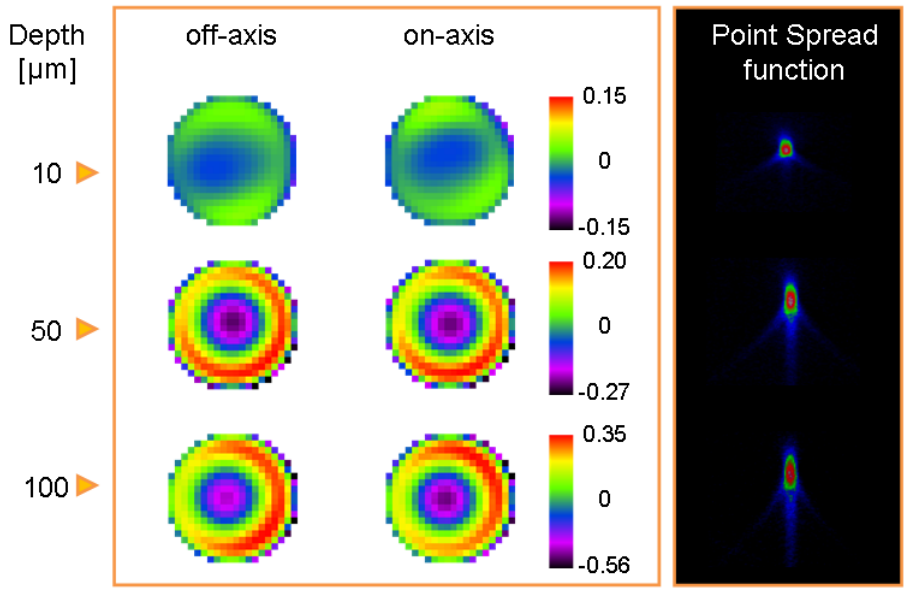

Figure: 4.7. Example measurements of the WFs taken at different depths from the test sample: (left) off-axis, (middle) on-axis and (right) corresponding point spread functions. The WFEs in µm are: 0.02 and 0.023 for a depth of 10 µm, 0.121, and 0.122 for a depth of 50 µm and 0.215 and 0.236 at a depth of 100 µm for the off-axis and on-axis measurements respectively.

From the shape of the WF maps shown on figure 4.7, it can be observed that the WF distortion is mainly caused by spherical aberration having a similar WFE across the FOV at each analyzed depth. In these experiments spherical aberration reached up to ~69% of the total measured aberrations at 100 µm inside the sample. The right panel of figure 4.7 demonstrates the enlargement of the point spread function as it is imaged deep inside the sample. The next step is to compare the obtained WFE for both cases (off-axis vs. on-axis) at different depths. As it was previously observed on the WF maps, such distortions seem to be similar at first sight. By plotting the RMS WFE within both cases for the different depths, the behavior observed in figure 4.7 can be confirmed as these have similar magnitudes.

An average dispersion in the total RMS WFE of only ~ 9.1% is observed between all the measured points (see figure 4.8); this can be attributed to the experimental error as different regions inside the sample were measured.

Moreover, it can be observed that the off-axis aberration effects behave similarly to the on-axis for the employed FOV. The similarity of these results enables to compare the experimental data with what it is predicted by established theoretical models [2]. As it can be observed on figure 4.8, the measured WFs follow the same trend compared to what is predicted by theory, where spherical aberrations increase linearly as a function of depth (see purple line). These results enable to confirm that the employed methodology is capable of measuring sample induced aberrations using a model sample.

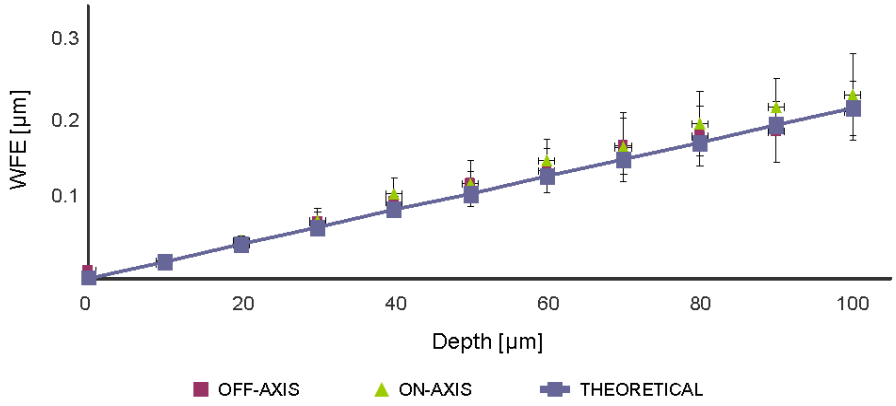

Figure: 4.8. WFE measurements taken at different depths inside a test sample. The dark red squares are the WFE measurements recorded at the off-axis position the green triangles are the on-axis WFE measurements and the purple line is the theoretical calculation of aberrations behavior considering the parameters of the test sample.

As it has been observed previously on figure 4.7, the shape of the WF map is given mostly by the spherical aberration. This is already known as theoretical models have described the effects of index mismatch in simple interfaces, such as the test samples used to on this research [2].

Based on the observation that spherical aberrations represent up to ~69% of the total WFE (when imaging deep inside the sample), the corresponding coefficients were studied. As before, the aim of this analysis is to observe the depth dependence of spherical aberrations especially to compare the off-axis case against the on-axis measurements for third, fifth and seventh order spherical aberration. As it is expected, it can be observed that both measurements (off-axis vs. on-axis) behave similarly within the analyzed order of spherical aberration. From figure 4.9 it can be observed that the Zernike coefficient values have a slight dispersion, this was calculated to be on average ~6.5%, ~2.8% and ~2.7% for third, fifth and seventh order spherical aberrations respectively. As before this can be attributed to the experimental error as different regions inside the sample were measured.

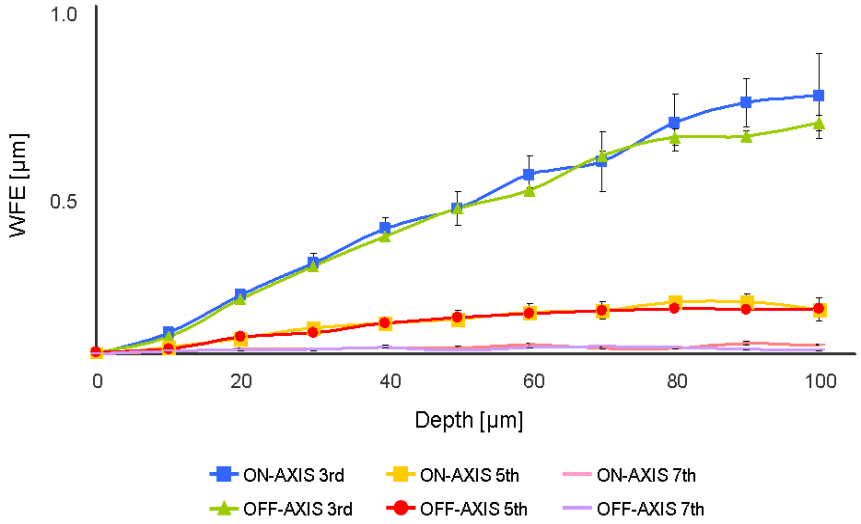

Figure: 4.9. Third, fifth and seventh order Spherical aberration measurement plots obtained at different depths using the test sample.

All these results confirm that for the employed high numerical aperture objective and at a distance of ≤35 µm from the microscope optical axis, the off-axis aberrations behave similarly to the on-axis aberrations. Thus revealing that within a radius ≤ 35 µm only a single on-axis measurement would be required to compensate most of the aberrations contained in the FOV for each optical section to be imaged. For the case of recording only a single on-axis NL-GS measurement agrees with previous works, where a central pixel has been iteratively corrected (employing a sensor-less approach) accounting for most of the aberrations present in the entire FOV [15].

Furthermore, in thicker, more inhomogeneous samples or when a larger field of view is required, multiple NL-GS can be acquired by placing them at different positions within the FOV. This would enable the correction of a wider area or volume.

All these experimental results measured through the use of the NL-GS concept demonstrate its robustness. This has been done for the first time to the best of my knowledge by showing that the NL-GS concept is able to measure the aberrations caused by the focusing part of the system independently of the excitation beam. Then the off-axis aberration effects at a given plane were compared to the obtained on-axis results to find out the amount of measurements to be taken for characterizing the FOV aberrations. The study was then performed at different depths comparing the on-axis vs. the off-axis cases by observing the WF maps. To validate the methodology, the measured WFEs were compared with a theoretical model used to predict aberrations in homogenous samples having an index mismatch [2]. Finally the predominant aberration (spherical) behavior at different depths was analyzed demonstrating that within the here presented conditions, off-axis aberrations behave similarly to the on-axis aberrations. All this demonstrates that by acquiring a single measurement within the FOV of the employed microscope objective will capture most of the aberrations.

In the following sub section an experimental demonstration on how to employ the NL-GS concept will be presented. The aim is to take full advantage of the data recorded through this concept to restore the imaging capabilities of the microscopy work station while imaging deeper inside the sample. This will be carried out by actively modifying the microscopy system to enhance the interaction of the excitation beam with the optical elements of the microscope and then with the imaged sample.

4.4. Full coupling and focusing aberrations correction

The strategy to perform the full aberrations correction of the microscopy system including the sample contributions will be outlined. Then several correction examples will be presented to shown that the recorded information using the NL-GS can be employed for correcting aberrations in a single step with the help of a DM. This is demonstrated using both *in vitro* and in *vivo* biological samples. By doing so it is demonstrated how the enhancement of the corrected images, when compared with the non-corrected ones, results in an improvement of more than one order of magnitude in the total collected signal intensity.

In the previous subchapters, the measurement process of the aberrations introduced by both the optical elements in the path that goes from the laser to the objective pupil called "Coupling aberrations" and in the objective, the refractive index matching oil, the cover-glass and the sample called "Focusing aberrations" where described. In this section a strategy to correct all the aberrations present in the microscopy setup will be presented employing biological samples.

To properly asses the aberrations coming from the NL-GS, it is important to first eliminate the passive aberrations of the microscope system. Taking into account this, the first correction was applied to correct for the coupling aberrations. In the present experiment a closed-loop configuration was chosen [21]. The SH WFS was located at the microscope objective pupil plane to measure the WF of the excitation beam (using the microscope output port). The aberrations were recorded, and then the first 20 Zernike coefficients were transmitted to the AO control software. Note that coupling aberrations only need to be corrected once, resulting in a permanent calibration of this part of the system. Figure 4.10 shows this correction. Once Coupling Aberrations are corrected, the aberrations generated from the objective pupil to the output port of the microscope (i.e. including the conjugation lens) were measured and taken into account as a reference for all the subsequent WF measurements.

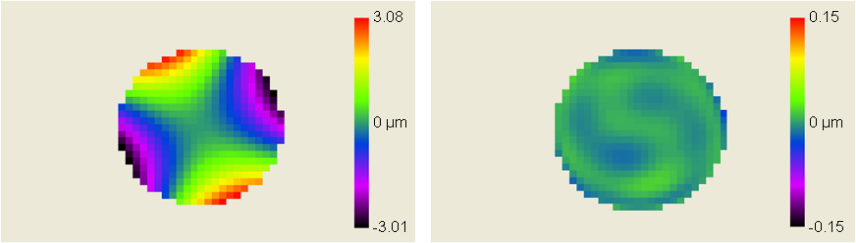

Figure: 4.10. Resulting system calibration correction applied to the excitation beam and coupling optics. Left panel aberrated excitation beam and right panel corrected beam using a closed-loop configuration. The initial WFE was 1.31 µm. After the system was calibrated for coupling aberrations, the residual wavefront error was 0.007 µm. The planes (tilts) and spherical (focus) components of the WFs have been removed.

The second correction step consisted on measuring the Focusing Aberrations. To do that, it was taken into account the fact that the TPEF signal from the NL-GS is the result of an incoherent process and destroys the WF phase information of the excitation beam. Therefore the NL-GS does not inherit the coupling aberrations as demonstrated before. Then the WF generated from the NL-GS will only contain the focusing aberrations which can be measured in a single step by employing the SH WFS. Once aberrations were measured, they were directly transmitted to the DM in a Zernike coefficients format and then it was shaped only once. This allowed recording images with minimized aberrations. Here it is also important to say that focusing aberrations were measured at a different wavelength from that to the excitation beam. In the here proposed methodology, it has been assumed that focusing aberrations introduced in the excitation beam are similar to those introduced in the measured TPEF signal [25]. Therefore it has been assumed that chromatic aberration, i.e., the effect of the wavelength change, is smaller than the total contribution of the Focusing Aberrations (this will be discussed further). Notice also that if a small amount of scattered light is produced, it would be simply added to the background without changing the recorded WFs [22].

Based on the designed correction strategy, the next step was to prepare different *in vivo* and *in vitro* biological samples to demonstrate how the measurement methodology demonstrated in the previous sub-sections can be used to improve the imaging quality of the NL microscopy workstation, pushing it towards its limits.

Caenorhabditis elegans (*C. elegans*) samples were employed for the *in vivo* correction trials. The selected nematode strain expresses the “cameleon” (calcium indicator) [28] fluorescent protein in the pharyngeal region. Such protein is composed of four domains: cyan fluorescent protein (CFP), calmodulin, M13 (a calmodulin binding domain), and yellow fluorescent protein (YFP). For these particular set of experiments only the TPEF signal from the CFP was excited using 860 nm. The selection of this fluorescent protein was based on the knowledge gained with the strategy presented in chapter 3. For this experiments the two-photon action cross-section was also well matched to enable an efficient nonlinear excitation

using low powers and at the same time obtaining as much fluorescent photons as possible. The maximum two-photon action cross-section for such fluorescent protein is located around the employed excitation wavelength [29]. This condition was of extreme importance for performing the WF measurements coming from the NL-GS, as the WFS is based on a standard CCD camera. Its sensitivity is of less than a few nanojoules therefore, the integration time needed to measure such WF was adjusted to 800 ms.

To evaluate the performance of the proposed strategy for correcting focusing aberrations, the WF values of the NL-GS inside a living specimen were directly measured, at the center of the FOV (based on the isoplanatic patch validation) and at different depths. It is worth noticing that the produced spherical aberrations due to the oil and sample refractive index mismatch can be non-negligible and that these will not be distinguished from the aberrations produced only from the sample itself.

For the first trial an *in vivo C. elegans* sample sandwiched between two cover-glasses was used (see appendix A 1.8 for detailed mounting procedures). In this case corrections were performed inside the terminal bulb of the pharynx which is located between the hypodermal layers and encased in a basement membrane. As it is imaged inside the terminal pharyngeal bulb, the structure is mainly composed of muscle. The pharyngeal region of this sample was selected as it is formed by different interfaces producing different magnitudes of index mismatch. The experiments were performed at three different depths corresponding to the surface, mid-plane and upper-plane of the pharyngeal region.

In Figure 4.11 the correction steps can be observed. Firstly the sample was imaged without applying any correction (Figure 4.11a). Secondly the coupling aberrations correction was applied (Figure 4.11b). This was followed by generating the NL-GS inside the living sample (see red spot on Figures 4.11b, 4.11e and 4.11h) to correct for the focusing aberrations. Please note that the result shown in this last correction step includes both the coupling and focusing aberrations correction.

To obtain the intensity improvement in both correction steps the intensity values form all the pixels were added and then the ratio with respect to the uncorrected image was obtained. For the images taken at a depth of 25 μm, an enhancement of 1.75 was measured when correcting for coupling aberrations, then, the intensity enhancement went up to 3.61 when focusing aberrations were corrected. In this case the recorded WFE was 0.16 μm and the main source of aberration was third order spherical aberration (see Figures 4.11, a, b, and c). The same procedure was performed at different depths for the same pharynx (see Figures 4.11 d–i). The WFEs were of 0.24 μm and 0.43 μm for images taken at a depth of 35 μm and 45 μm, respectively. In agreement with what is predicted by theoretical models [30] it was found that third order spherical aberration increased approximately in a linear fashion as the NL-GS was used to measure aberrations deeper inside the sample (data not shown). At 35 μm an intensity improvement of 1.90 was obtained by correcting the coupling aberrations and an

improvement of 2.35 was achieved by correcting the focusing aberrations. At 45 µm the improvement factor was 1.62 after correcting the coupling aberrations and 2.02 for correcting the focusing aberrations. As it was expected, the intensity enhancement after the correction is bounded by the amount of aberrations present in this sample [7, 27, 31].

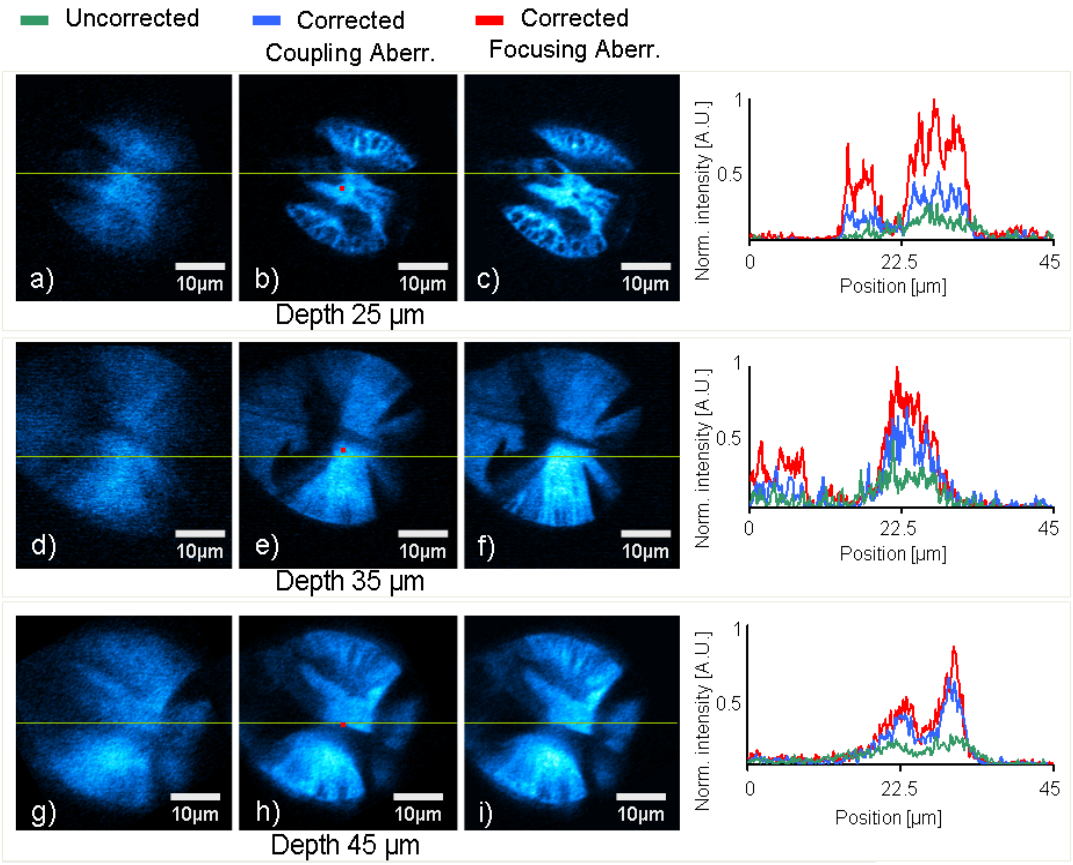

Figure: 4.11. Single frame images taken from an *in vivo C. elegans* sample. The imaged depths are 25 µm, 35 µm and 45 µm for the first, second and third rows respectively. The improvement factors with respect to the uncorrected case are 1.75 for (b) and 3.61 for (c); 1.90 (e) and 2.35 (f); 1.62 (h) and 2.02 (i). The gained improvement factor with respect to the coupling aberrations are 2.06 (c), 1.24 (f), and 1.24 (i). The plot profiles on the last column correspond to green line on each image. The red spot corresponds to the position where the NL-GS was measured. The WFS integration time was set to 800 ms for all the cases.

In addition to the total image intensity increase after each correction step, a plot profile was traced on each image to show the normalized intensity and contrast enhancement in a specific region of interest (right column in Figure 4.11). Importantly, the background signal (dark parts of the images) remains unchanged (no noise has been introduced after the correction). As a consequence, this directly gives an improvement in the contrast. As it is imaged deeper inside the sample greater intensity improvements are expected, compared to the corrections made at the superficial layers. This is, however, not the case for Figure 4.11i. This could be due to experimental variables inherent of working with living specimens such as sample preparation, positioning, etc. Nonetheless, this experiment demonstrated that the NL-GS is

able to capture the sample induced aberrations inside a living specimen in a noninvasive way. The use of this methodology eliminates the need of complex algorithms and the process of acquiring multiple images being able to minimize photo-bleaching effects. At the same time it provides the required information in a single and quick measurement to achieve an overall intensity improvement.

In what follows (see Figures 4.12 and 4.13), the nematodes are placed at larger depths in order to verify if the unexpected correction deviation observed in Figure 4.11i is preserved. Furthermore for the next set of experiments the NL-GS principle was tested at increased depths by adding an additional interface and a scattering media. In this case a 1% agar pad was used as it has a similar refractive index to deep epidermis and basal layers of skin [32]. The final thickness of such interface was 90 μm. The nematode was placed on top of this layer sandwiched between two cover-glasses (see appendix A 1.8 for detailed mounting procedures). The total imaging depths in these experiments were 115 μm, 125 μm and 135 μm (similar regions were imaged inside the nematode than the ones acquired in the previous experiment plus the 90 μm agar pad). In this way the procedure was performed at the limit of the working distance of the employed high numerical aperture microscope objective. The correction steps where performed as it was explained before and at different depths inside the sample. The results are presented in Figure 4.12.

In these experiments, it was found that the agar pad increased the WFE by an average factor of ~ 4.5 times and for third order spherical aberration an average factor of ~3.9 times compared to what it was recorded on the previous experiment. When correcting for the coupling aberrations the measured intensity improvements were 1.89, 1.58 and 1.29 (Figures 4.12 b, e and h) for a depth of 115, 125 and 135 μm respectively. As the coupling aberrations were calibrated previously it results in a similar amount of correction as the one achieved in the case were no agar was placed before the sample. This was followed by correcting for the coupling aberrations, in this case the achieved intensity improvements were 5.32, 4.78 and 9.1 (Figures 4.12 c, f and i) for depths of 115, 125 and 135 μm respectively. As before, the NL-GS is able to capture the focusing aberrations even passing through a 90 μm interface that increases the amount of spherical aberrations. This steady increase in intensity can be also observed in the line profile traced in a region of interest to demonstrate the intensity improvement achieved employing the NL-GS (see green lines in Figure 4.12). In addition, the contrast improvement is clear since the aberration correction only increases the points with a local maximum, while the local minima remains unaltered.

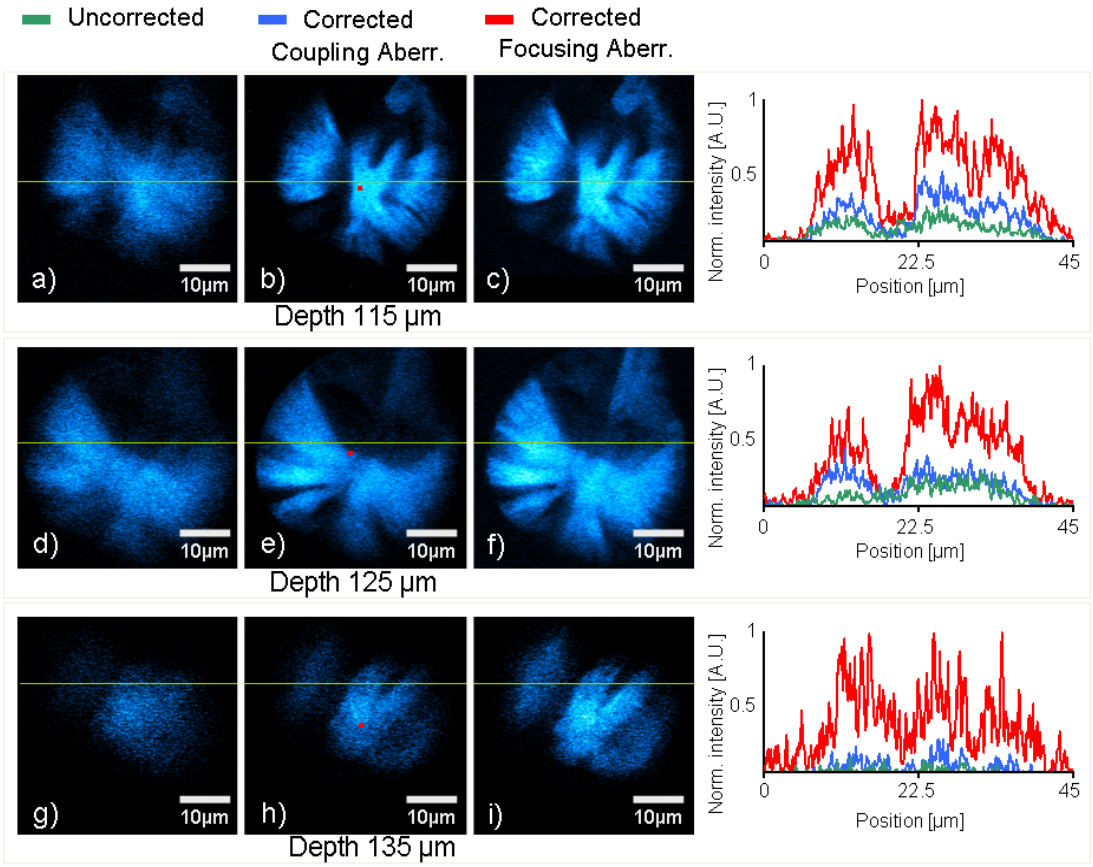

Figure: 4.12. Single frame images taken from an *in vivo C. elegans* sample. The imaged depths are 115 µm, 125 µm and 135 µm for the first, second and third rows respectively. The improvement factors with respect to the uncorrected case are 1.89 for (b) and 5.32 for (c); 1.58 (e) and 4.78 (f); 1.29 (h) and 9.1 (i). The gained improvement factor with respect to the coupling aberrations are 2.82 (c), 3.03 (f), and 7.08 (i). The plot profiles on the last column correspond to the green line on each image. The red spot corresponds to the position where the NL-GS was measured. The WFS integration time was set to 800 ms for all the cases.

Furthermore, the objective of this study was to thoroughly test the capabilities of the NL-GS methodology in scattering samples. For this purpose two different samples were examined.

The first one consisted of a nematode placed on top of a pad (same thickness as before) with a higher concentration of agar (2%). This made the agar pad more opaque producing an increase in light scattering (see Figure 4.13). The second sample was a brain slice having sparsely distributed neurons that is highly scattering, see appendix A 1.8 and 1.9 for detailed mounting procedures (Figure 4.14).

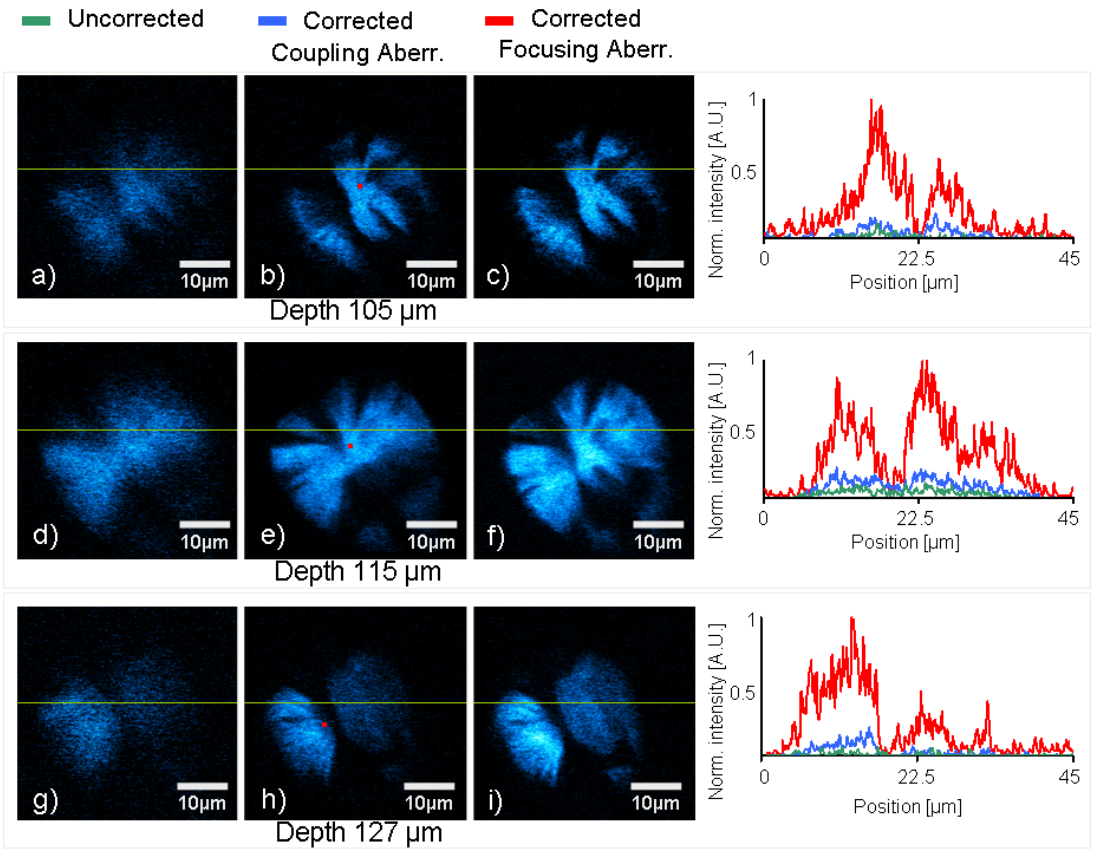

Figure: 4.13. Single frame images taken from an *in vivo C. elegans sample*. The imaged depths are 105 µm, 115 µm, and 127 µm for the first, second, and third rows, respectively. The improvement factors with respect to the uncorrected case are 1.70 for (b) and 17.04 for (c); 2.15 (e) and 11.24 (f); 1.94 (h) and 22.59 (i). The gained improvement factor with respect to the coupling aberrations are 10 (c), 5.23 (f), and 11.66 (i). The plot profiles on the last column correspond to the green line on each image. The red spot corresponds to the position where the NL-GS was measured. The WFS integration time was set to 800 ms for all the cases.

In this experiment (see Figure 4.13 second column) the first step was to correct for the coupling aberrations. As before a similar correction factor was obtained. In this case, the RMS WFE increased by an average factor of ~5.2 times and the spherical aberration by ~ 4.5 times (compared with the first experiment). The achieved intensity improvements were 1.7, 2.15 and 1.94 (Figures 4.13 b, e and h) for depths of 105, 115 and 127 µm, respectively. The intensity improvements after correcting for the focusing aberrations increased considerably as the amount of sample induced aberrations now play a major role limiting the intensity prior to its correction. The improvements were 17.04, 11.22 and 22.59 (Figures 4.13 c, f, and i) for depths of 105, 115 and 127 µm respectively. This intensity improvement is evident as shown in the plot profile. Here the focusing aberration corrections results in a major improvement. Again, the intensity and contrast improvement caused by the aberration correction is reflected in an increase of the points having a local maximum, while the local minimum remains unaltered.

With the previous results the capability of the NL-GS methodology for measuring and correcting the sample aberrations in the situation where the main source of aberration is the sample (in this case the agar pad) has been demonstrated. In other type of specimens, the imaging depth is limited by the scattering of the tissue which changes exponentially with depth [10] (while aberration effects change linearly). Thus the next experiment consists on applying the NL-GS concept to samples having a larger scattering coefficient. In this case mouse brain slices were employed.

These samples were modified to express green fluorescent protein (GFP) in sparsely distributed neurons (see appendix A 1.9 for detailed preparation and mounting procedures), and had a total thickness of 60 µm (cut on a cryostat). For the experiments, the samples were placed on a glass bottom Petri dish containing fresh medium to keep the slice at optimum conditions. As before two different depths were imaged. For a WF measurement in such conditions it is necessary to have at least a spot within the region of interest where the NL-GS emission intensity can be sensed by the WFS (see red spot on Figures 4.14b and e). Then the NL-GS is used to measure the sample induced aberrations. In this conditions where the fluorescent protein is not very efficiently excited using the Ti:S at 860 nm, the WFS integration time required to be adjusted.

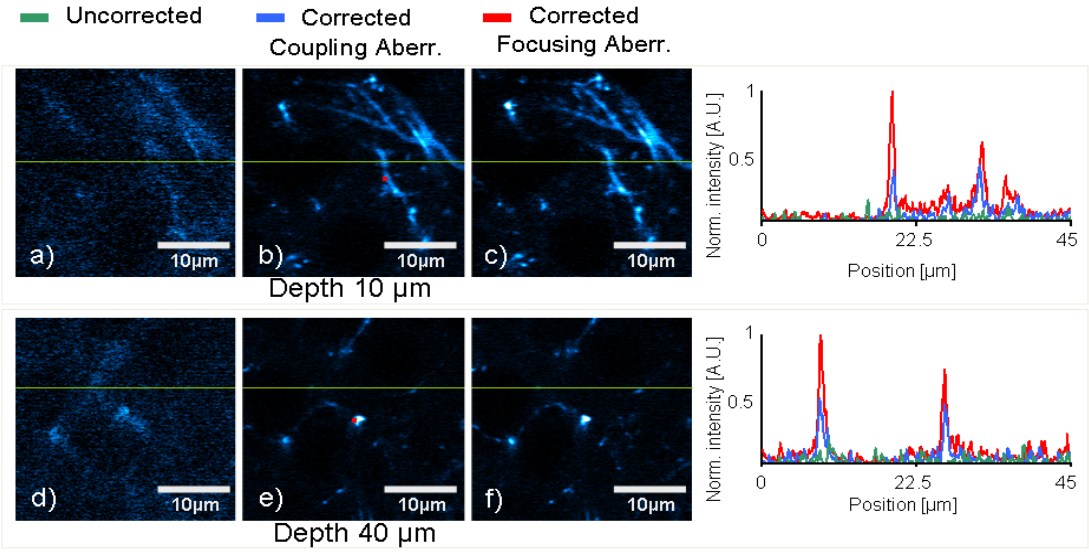

Figure: 4.14. Single frame images taken from mouse brain slices expressing GFP in sparsely distributed neurons. The imaged depths are 10 µm and 40 µm for the first and second rows, respectively. The improvement factors with respect to the uncorrected case are 2.74 for (b) and 5.69 for (c); 1.98 (e) and 3.91 (f). The gained improvement factor with respect to the coupling aberrations are 2.08 (c) and 1.98 (i). The plot profiles on the last column correspond to the green line on each image. The red spot corresponds to the position where the NL-GS was measured. The WFS integration time was set to 1000 ms for all the cases.

As it was mentioned in chapter 3 the Ti:S laser two-photon action cross section is 3 times less due to its operating wavelength and in that case it was required to almost double its peak power. However, accounting for the fact that the employed wavelength used to excite GFP

will not perform as if the maximum two-photon action cross-section is well matched; a new commercially available IR optimized microscope objective (CFI Apo 60x Oil λS, Nikon Japan with enhanced transmission) was used. Figure 4.14 shows the obtained results.

The intensity improvements gained by correcting for the coupling aberrations were 2.74 and 1.98 were obtained at depths of 10 μm and 40 μm, respectively (see Figures 4.14 b and e). The next step was to correct for the focusing aberrations. In this case, it was found that the RMS WFE was 0.213 μm and 0.284 μm at depths of 10 and 40 μm, respectively. As before, the third order spherical aberration was dominant having a value of −0.51 μm and −0.67 μm at depths of 10 μm and 40 μm respectively. As it was expected the aberration effects remained moderate while scattering effects resulted in the requirement of an efficient excitation strategy to image the sample.

After correcting for the focusing aberrations, the resulting intensity improvements on the generated images were 5.69 and 3.91, at 10 μm and 40 μm respectively.

By comparing the results obtained for both, moderate (Figures 4.11-4.13) and strongly scattering samples (Figure 4.14), it can be observed that AO has a larger impact on the correction when moderate scattering specimens are employed, as they allow imaging at deeper planes. For more scattering samples, it was found that a correction is still possible and the obtained improvements are in agreement with those achieved by using other sensor-based adaptive optics correction schemes (~2) [10]. However, scattering will dominate as the imaging goes deeper. This suggests the requirement of more power to image the sample or the use of other strategies such as the use of index matching media inside *in vitro* samples to reduce scattering [15].

It is important to remember that for this particular experiment, the NL-GS was created at different depths (i.e. at the plane where the correction was required). In addition, based on the isoplanatic patch measurements the NL-GS was placed only at the on-axis position. Nevertheless, to verify these results, a line profile was traced (see the green line of figures 4.11 – 4.14) at different locations from the on-axis position. Also in this case, the improvement obtained after the correction is still significant. This means that field aberrations are not a limiting parameter within the considered samples and microscope objectives. In addition, by using the NL-GS concept one can take advantage of the fact that the position of this reference light source is always kept on hands of the user and several FOV corrections, using different NL-GS, could be considered for a particular study. Then, as it is done in multi laser guide-star telescopes, stitching methods should be considered for the reconstruction of the final aberration corrected images. Similarly, as it was shown, several NL-GS can be collected for different depths in thicker samples. This means that in general, such principle could be used, according to the requirements of each sample, for acquiring aberration-corrected three dimensional images.

Note that the correction of the excitation beam is based on a measurement that has been done at a different wavelength (fluorescence signal). This shift however did not affect the NL-GS method, resulting in a clear signal intensity and contrast improvement as it can be seen from Figures 4.11 – 4.14. This independence of the correction with the wavelength shift is probably due to the employed microscope objectives, which are corrected for chromatic aberrations from ultra violet to IR. These results agree with previous works where chromatic effects have already been reported to be negligible over a significant wavelength difference [25, 26].

Finally, in many applications for example when imaging microfluidic channels, the NA of the imaging system could be limited by the refractive index mismatch of the sample. This introduces significant aberrations despite the fact that you are not using the highest NA as it is the case of water immersion objectives. This also applies for experiments in which the purpose is imaging the sample at greater depths. In this situation also water immersion objectives are normally used. The here presented technique can be equally used in such conditions and take advantage of the theoretical resolution. This is possible as the NL-GS concept was developed to measure the aberrations caused by the elements that are changed on every experiment such as the microscope objective, the immersion fluid, the cover-glass and the sample. Note that in this thesis it was decided not to use water immersion but oil immersion as these have the highest NA to be recovered.

4.5. Summary

The NL-GS concept has been demonstrated by correcting the measured aberrations induced by the sample and the objective in a single-step. This NL-GS is created by focusing the excitation beam inside the sample to produce a TPEF volume which is considered as a secondary light source. Furthermore, based on the fact that fluorescence is an incoherent process, it does not inherit the aberrations gained by the excitation beam.

The WF from the NL-GS can then be measured using a WFS placed at the output port of the NL microscope. Moreover, as the WF is directly expressed in the form of Zernike coefficients, it is possible to shape the adaptive element (DM) in a single step (i.e. without the need of any search algorithm) for correcting the measured aberrations. By doing so, image quality and contrast can be significantly improved without having to expose the sample for large periods of time. Consequently photo-bleaching and photo-toxicity are greatly reduced.

This methodology brings several advantages: it can be applied *in vivo*, it is simple, noninvasive and requires no additional sample processing (such as the incorporation of fluorescent beads). Moreover, the NL-GS can be created at any desired position inside a sample. This principle has been demonstrated with both, moderate and increased scattering samples. For moderate scattering samples, it has been found that the total signal

improvement can reach up to 22.5 times (see Figure 4.13i). For samples with increased scattering, it has been found that the correction is moderate but in agreement with other adaptive optics correction schemes [10]. All this demonstrates that, under the high resolution conditions (NA = 1.4) here used, this methodology is able to successfully deal with the aberrations present in the imaging system. Overall, this technique can be successfully employed in a great number of cases, for example in microfluidic channels or in general for other biological applications where a high resolution (i.e., not limited by the refractive index of the sample) is required.

References

1. W. Denk, J. H. Strickler, and W. W. Webb, "2-photon laser scanning fluorescence microscopy," Science 248, 73-76 (1990).

2. M. J. Booth, and T. Wilson, "Refractive-index-mismatch induced aberrations in single-photon and two-photon microscopy and the use of aberration correction," Journal of Biomedical Optics 6, 266-272 (2001).

3. D. Ganic, X. S. Gan, and M. Gu, "Reduced effects of spherical aberration on penetration depth under two-photon excitation," Applied Optics 39, 3945-3947 (2000).

4. F. Helmchen, and W. Denk, "Deep tissue two-photon microscopy," Nature Methods 2, 932-940 (2005).

5. M. A. A. Neil, R. Juskaitis, M. J. Booth, T. Wilson, T. Tanaka, and S. Kawata, "Adaptive aberration correction in a two-photon microscope," Journal of Microscopy-Oxford 200, 105-108 (2000).

6. D. Debarre, E. J. Botcherby, T. Watanabe, S. Srinivas, M. J. Booth, and T. Wilson, "Image-based adaptive optics for two-photon microscopy," Optics Letters 34, 2495-2497 (2009).

7. J. M. Bueno, E. J. Gualda, and P. Artal, "Adaptive optics multiphoton microscopy to study ex vivo ocular tissues," Journal of Biomedical Optics 15 (2010).

8. Z. Kam, P. Kner, D. Agard, and J. W. Sedat, "Modelling the application of adaptive optics to wide-field microscope live imaging," Journal of Microscopy-Oxford 226, 33-42 (2007).

9. M. J. Booth, M. Schwertner, and T. Wilson, “Specimen-induced aberrations and adaptive optics for microscopy,” Proc. SPIE 5894, 26–34 (2005).

10. J. W. Cha, J. Ballesta, and P. T. C. So, "Shack-Hartmann wavefront-sensor-based adaptive optics system for multiphoton microscopy," Journal of Biomedical Optics 15 (2010).

11. D. Debarre, M. J. Booth, and T. Wilson, "Image based adaptive optics through optimization of low spatial frequencies," Optics Express 15, 8176-8190 (2007).

12. M. J. Booth, "Wave front sensor-less adaptive optics: a model-based approach using sphere packings," Optics Express 14, 1339-1352 (2006).

13. P. N. Marsh, D. Burns, and J. M. Girkin, "Practical implementation of adaptive optics in multiphoton microscopy," Optics Express 11, 1123-1130 (2003).

14. W. Lubeigt, S. P. Poland, G. J. Valentine, A. J. Wright, J. M. Girkin, and D. Burns, "Search-based active optic systems for aberration correction in time-independent applications," Applied Optics 49, 307-314 (2010).

15. J. M. Girkin, J. Vijverberg, M. Orazio, S. Poland, and A. J. Wright, "Adaptive optics in confocal and two-photon microscopy of rat brain: a single correction per optical section - art. no. 64420T," in Multiphoton Microscopy in the Biomedical Sciences VII, A. Periasamy, and P. T. C. So, eds. (2007), pp. T4420-T4420.

16. A. J. Wright, D. Burns, B. A. Patterson, S. P. Poland, G. J. Valentine, and J. M. Girkin, "Exploration of the optimisation algorithms used in the implementation of adaptive optics in confocal and multiphoton microscopy," Microscopy Research and Technique 67, 36-44 (2005).

17. P. Kner and Z. Kam, “Adaptive optics takes tissue imaging to the next level,” BioOpt. World 1, 32–34 (2008).

18. M. Rueckel, J. A. Mack-Bucher, and W. Denk, "Adaptive wavefront correction in two-photon microscopy using coherence-gated wavefront sensing," Proceedings of the National Academy of Sciences of the United States of America 103, 17137-17142 (2006).

19. M. J. Booth, "Adaptive optics in microscopy," Philosophical Transactions of the Royal Society a-Mathematical Physical and Engineering Sciences 365, 2829-2843 (2007).

20. X. Tao, O. Azucena, M. Fu, Y. Zuo, D. C. Chen, and J. Kubby, "Adaptive optics microscopy with direct wavefront sensing using fluorescent protein guide stars," Optics Letters 36, 3389-3391 (2011).

21. F. Roddier, “Adaptive Optics in Astronomy,” Cambridge University Press, (1999).

22. O. Azucena, J. Crest, J. A. Cao, W. Sullivan, P. Kner, D. Gavel, D. Dillon, S. Olivier, and J. Kubby, "Wavefront aberration measurements and corrections through thick tissue using fluorescent microsphere reference beacons," Optics Express 18, 17521-17532 (2010).

23. I. G. Cormack, P. Loza-Alvarez, L. Sarrado, S. Tomas, I. Amat-Roldan, L. Torner, D. Artigas, J. Guitart, J. Pera, and J. Ros, "Lost writing uncovered by laser two-photon fluorescence provides a terminus post quem for Roman colonization of Hispania Citerior," Journal of Archaeological Science 34, 1594-1600 (2007).

24. R. Aviles-Espinosa, G. Filippidis, C. Hamilton, G. Malcolm, K. J. Weingarten, T. Suedmeyer, Y. Barbarin, U. Keller, S. I. C. O. Santos, D. Artigas, and P. Loza-Alvarez, "Compact ultrafast semiconductor disk laser: targeting GFP based nonlinear applications in living organisms," Biomedical Optics Express 2, 739-747 (2011).

25. O. Azucena, J. Crest, S. Kotadia, W. Sullivan, X. Tao, M. Reinig, D. Gavel, S. Olivier, and J. Kubby, "Adaptive optics wide-field microscopy using direct wavefront sensing," Optics Letters 36, 825-827 (2011).

26. X. Tao, B. Fernandez, O. Azucena, M. Fu, D. Garcia, Y. Zuo, D. C. Chen, and J. Kubby, "Adaptive optics confocal microscopy using direct wavefront sensing," Optics Letters 36, 1062-1064 (2011).

27. V. A. Hovhannisyan, P. J. Su, and C. Y. Dong, "Characterization of optical-aberration-induced lateral and axial image inhomogeneity in multiphoton microscopy," Journal of Biomedical Optics 13 (2008).

28. R. Kerr, V. Lev-Ram, G. Baird, P. Vincent, R. Y. Tsien, and W. R. Schafer, "Optical imaging of calcium transients in neurons and pharyngeal muscle of C-elegans," Neuron 26, 583-594 (2000).

29. M. Drobizhev, N. S. Makarov, S. E. Tillo, T. E. Hughes, and A. Rebane, "Two-photon absorption properties of fluorescent proteins," Nature Methods 8, 393-399 (2011).

30. M. J. Booth, M. A. A. Neil, and T. Wilson, "Aberration correction for confocal imaging in refractive-index-mismatched media," Journal of Microscopy-Oxford 192, 90-98 (1998).

31. E. Theofanidou, L. Wilson, W. J. Hossack, and J. Arlt, "Spherical aberration correction for optical tweezers," Optics Communications 236, 145-150 (2004).

32. C. Y. Dong, B. Yu, P. D. Kaplan, and P. T. C. So, "Performances of high numerical aperture water and oil immersion objective in deep-tissue, multi-photon microscopic imaging of excised human skin," Microscopy Research and Technique 63, 81-86 (2004).

Chapter 5

Conclusions and future prospects

5.1. Conclusions

In this thesis several strategies for pushing nonlinear microscopy (NLM) towards it limits have been presented. These have been implemented by considering the most important aspects for the design of a nonlinear (NL) imaging device. Such aspects are: the performance of the optical elements at IR wavelengths together with the employed excitation source, the optical sample properties and the type of study to be performed. It is always important to keep in mind that the biological specimen should be considered as the most important part of the study to provide a cutting edge NLM device for bio-imaging research. This means that the sample is the only part in the system that cannot be altered and should be manipulated as less as possible, as any external interference can lead to erroneous conclusions.

In this way, the main driving force of the here presented thesis has been focused on researching the main aspects for pushing the limits of NLM. The research here presented was also considered as part of the Fast-dot and the Stelum European projects (where I participated) given that this research is of great importance for the laser development and bio-imaging industry.

In this context, three strategies were carried out to accomplish the thesis objectives. These were 1) taking advantage of the light and the sample interaction to gain contrast, 2) The use of compact laser systems designed to match the two-photon absorption peak of one of the most widely used fluorescent dyes (the green fluorescent protein) for reducing the required peak intensities to image the sample and 3) The demonstration of the nonlinear guide-star concept to measure sample aberrations to obtain the information on how to modify/adapt the NLM for restoring its diffraction limited performance at different depths. From the results obtained in each strategy, it can be concluded that the main goal of this thesis, which was focused of pushing the limits of NLM, has been achieved. This has been carried out following the methodology of adapting the required part on a NL microscope to enhance its interaction with a living specimen.

The first strategy was based on developing a way of having a light source that could efficiently interact with both the optical elements and take advantage of the optical properties of the sample to generate contrast. This was carried out by building a NLM workstation based on a state of the art fiber-based laser source operating at 1550 nm for performing third harmonic generation (THG) microscopy. The use of this device has aided on the

simplification and integration of NLM techniques into biology, thanks to its compact design, output wavelength, pulse duration and repetition rates. Moreover, these lasers use reliable state-of-the-art telecommunications components that have been developed for long-term operation, minimum maintenance and moderate cost.

In this strategy the key aspects were the characterization of the optical elements transmission (at IR wavelengths) in the microscope path until the microscope objective. This last element was selected based on performance tests based on transmittance measurements and intensity calculations for achieving an optimum performance at IR wavelengths. The THG signal was confirmed by recording the emitted spectrum from a test sample and then through imaging experiments of different samples and model organisms. The performance of the developed device was compared with a conventional THG system. In this comparison the main advantages of the NLM workstation design where clearly demonstrated. These are based on the fact that laser source operating wavelength (1550 nm) generates a THG emission near the peak sensitivity of most commercial detectors (516 nm). In contrast with the other tested system (operating at 1028 nm), the use of 1550 nm eliminates the requirement of ultraviolet (UV) grade optics or the use of THG signal amplification schemes such as lock-in amplification. Based on this it is possible to reduce the amount of average and peak power required to image a sample up to seven times and still have a strong THG signal. Importantly the use of this NL imaging technique takes advantage of the optical properties of the sample to generate contrast as biological specimens have different structures with variations in their refractive indices giving a rise to THG at the interfaces.

All these advantages were demonstrated as part of the first strategy to reduce the sample manipulation and interference. Firstly by reducing the power requirements to image the sample and secondly by proposing the use of a label-free technique.

To further demonstrate the advantages of this methodology, morphogenesis studies were performed on living *Caenorhabditis elegans* (*C.elegans*) embryos. In this study all the developmental stages were identified starting from the cell division stage inside the adult nematode, the gastrulation process, the ventral closure, the elongation and the young larvae after hatching. In the latest developmental stages where the elongation and the beginning of the cuticle synthesis occurs, the developed NLM workstation was able to acquire such changes. However the movement of the nematodes was faster that the acquisition speed of the developed system. To address this, several solutions were proposed such as imaging the samples at lower temperatures to slow down its development, the use of laser systems having an increased repetition rate for allowing a faster imaging, and the minimization of aberrations as the samples are imaged at different depths for acquiring a three dimensional (3D) models.

The effects of the employed laser wavelength were studied by comparing the control samples versus irradiated samples as there is no available information of long-term imaging using this wavelength. In this study it was observed that the more developed embryos (after two-fold)

have a higher survival rate. This suggests that the development of different tissue such as cuticle or epidermis may act as a protection to this radiation.

Finally the sources of THG signal inside the different structures of the nematode still needs to be investigated. This can be done by performing co-localization studies using fluorescent markers to find out which structures are producing the signal. Once all the structures are identified, then use of fluorescent markers can be over passed, thus making the here presented technique at the employed wavelength useful to follow developmental processes *in vivo* and in a label-free way.

Despite the efforts of showing a label-free technique, the use of fluorescent markers is a highly common and well established practice. In addition, Two-photon excited fluorescence (TPEF) can be used to perform such co-localization studies. Therefore it is important to achieve an efficient interaction of the light source with the sample expressing a fluorescent protein to minimize sample interference such as photo-damage and photo-toxic effects.

Based on these requirements, in the second strategy the use of a compact laser system designed specifically for optimizing such conditions was demonstrated. In this strategy the operating parameters of such laser system were based on the two-photon figure of merit (FOM2p) and its operating wavelength.

Firstly, the FOM2p is a single number employed to relate the key operating aspects of an ultra-short pulsed laser system (average power, repetition rate and pulse duration) for NL imaging applications. This enabled to theoretically compare a laser system performance with other devices. In particular, the semiconductor disk laser (SDL) used for this thesis had a repetition rate of 500 MHz, pulse duration of 1.5 ps and an output power of 287 mW. This resulted in a FOM2p of 1.36 W^2 (at the sample plane). This is comparable with what is obtained when using the standard titanium sapphire (Ti:S) laser (1.56 W^2).

Secondly, together with the operating parameters it is important to optimize the two-photon absorption of the excitation light to be used. This was carried out by designing the laser system to operate at the peak of the two-photon action cross-section of one of the most widely used fluorescent markers in bio-imaging research: the green fluorescent protein (GFP). By having such wavelength set to 965 nm really allows reducing the peak power conditions required for an efficient excitation.

The developed prototype available for this thesis resulted in a compact (140x240x70 mm), affordable and easy to use device. Additionally the SDL is operated using a simple web interface as it is able to self start the mode-locking operation once it is switched on thanks to the semiconductor saturable absorber mirror (SESAM).Such system represents the first demonstration of the use of a VECSEL for nonlinear microscopy. The laser is sealed, requires no cleaning or realignment meaning that minimum maintenance is needed. This device has a high potential for its integration in clinics, biological laboratories etc.

To demonstrate the performance of the laser, several experiments were devised. The first trials were conducted using test samples such as fluorescent beads and fixed biological samples labeled using different biological markers. Here the SDL was able to efficiently excite such dyes using a reduced amount of peak power (0.04 KW). Then the compact source was employed to image living *C. elegans* samples. In this case TPEF the emission coming from neurons in different parts inside the nematode was efficiently observed without causing damage. In addition second harmonic generation (SHG) signal was recorded from pharyngeal, uterus, and body wall muscles based on the increased repetition rate of the system. The extended versatility of this device was presented by experimentally demonstrating that this laser source is also suitable to efficiently excite a wide range of biological markers

Moreover, the applicability of this device for different bio-imaging applications was demonstrated. One of these areas is time-lapse studies. This was assessed through photo-bleaching experiments demonstrating that the laser system can be used to follow developmental processes up to nine hours. Another application is depth imaging experiments. In this context the system was tested first under low numerical aperture (NA) conditions to have a long working distance. In this case, as expected the low NA produced a large focal spot, generating thus a weaker confinement of the light. From these results it was observed that higher peak power is required. To overcome this, the tests were performed under high numerical aperture conditions (i.e. the point spread function is smaller and therefore intensity is higher). In this case the system was able to be used for imaging at a total depth of 230 μm. The results indicated that this devise has the potential to be used for such task, however, the only limitation is that sample induced aberrations limit its performance reducing the diffraction limited performance of the NLM workstation.

Finally the system was compared against a Ti:S ultra-short pulsed laser system. In these experiments it was observed that the laser can efficiently be used for TPEF imaging (based on its design parameters) compared to the Ti:S system performance. In this context the SDL produced cleaner images due to the fact that the operating wavelength does not excite auto-fluorescent molecules inside the sample. Due to the fact that the Ti:S laser system in the lab cannot be tuned to the same operating wavelength as the SDL device, SHG tests were performed to remove the wavelength dependency. In these trials, it was observed that although the laser is able to generate nonlinear images, there is a need for higher peak powers (as average power is already high). Therefore, one of the main challenges of the proposed strategy is to develop a system delivering shorter pulses for the same average power without compromising its size, simplicity and affordability. This is something that it is currently being carried out with the collaborators. All these results enable to answer how to adapt the laser source for achieving an enhanced interaction with a sample expressing a fluorescent marker.

Preliminary experiments leading to the miniaturization of ultra-short pulsed devices were conducted. The devices available for this thesis were able to produce picosecond pulses at high repetition rates. These were developed to work at the spectral region of 1245 nm -1295 nm. Interestingly, this spectral range is located within the infrared penetration window of most biological tissues. Additionally this wavelength is suitable for imaging a considerable number of red fluorescent dyes. In particular, TPEF imaging experiments were carried out using test samples of fluorescent beads with a two-photon action cross-section peaking at these wavelengths.

NL imaging was carried out by testing different laser system configurations aiming to push up as much as possible its FOM2p (at the sample plane). These were 1) an edge emitting device having its wavelength centered at 1260 nm, 1 ps pulses, a repetition rate of 10 GHz, an average power of 100 mW, and a peak power 10 W corresponding to 0.02 W^2 at the sample plane, 2) a tunable device (1245-1295 nm) amplified by a chip-sized Quantum-dot based semiconductor optical amplifier (SOA) which provided pulses of 3 ps at 10 GHz repetition rate, an average power of 370 mW and a peak power of 12.3 W corresponding to 0.1 W^2 at the sample plane, and 3) an external cavity configuration for reducing the repetition rate to a similar value to what was obtained using the SDL device.

Importantly, by lowering the repetition rate from 10 GHZ to 648 MHz (using an external cavity configuration), a higher output peak power of 30.3 W was achieved together with a 208 mW average power, and a 6.3 W^2 FOM2p. By comparing the FOM2p (at the sample plane) of the first configuration with the third one, this was boosted 7 times, thus producing clearer images.

Due to the fact that edge emitting devices have an astigmatic output this reduces the available intensity for imaging. This cannot be corrected for the moment as the available output power is still moderate and therefore additional optics will further reduce it, limiting the ability to be tested for such purpose.

Moreover, and unlike previous demonstrations of nonlinear imaging with ultrafast laser diode systems, it has been presented for the first time systems that incorporate only a single amplification stage, and do not include external dispersion compensation, enabling a rather more compact and less complex laser system. The preliminary TPEF imaging results indicate that this chip-sized devices are promising as high peak-power ultra-short pulsed light sources. Importantly its emission wavelength that could potentially cover from 1000 nm to 1300 nm is very useful for nonlinear bio-imaging applications. These devices could lead to major progress and a widespread adoption of nonlinear imaging technology. Finally its dimensions (chip size 4 to 6 mm) could potentially enable these to be used for the development of micro-endoscopes, lab-on-a-chip devices etc.

Here the main challenge consists on increasing the peak output powers of such devices to reach the target requirements of NLM. This can be achieved by further decreasing the repetition rate through using an external cavity configuration, improving the beam quality (having a uniform intensity in the beam profile rather than an astigmatic one), and improving the input coupling efficiency between the output from the external cavity configuration and the SOA. This has already been talked with the partners involved in its development.

Finally, an extremely important aspect when imaging biological specimens is the fact that these are composed of different structures having a variation in their refractive index. This will affect the interaction of the excitation source and the biological sample causing index mismatch induced aberrations. This was observed in the previous strategies limiting the ability to preserve a diffraction limited performance of the NLM workstation. In this sense the third strategy for pushing NLM towards its limits was to understand how aberrations affect the imaging process. This strategy was developed as the state of the art techniques are based on indirect and complex methods of correcting for aberration effects. In these schemes aberrations are not measured.

The key aspects of the third strategy were based on performing the measurement of the microscope coupling optics aberrations using a wavefront sensor (WFS) located at the microscope camera port. The main target of this strategy was the measurement of the aberrations caused by elements that are changed in every experiment (microscope objective, immersion fluid cover-glass and sample) called focusing aberrations. This resulted in a simple and noninvasive way of measuring sample induced aberrations though a concept developed in this thesis work called the “nonlinear guidestar” (NL-GS).

This concept was exhaustively tested prior to its application. Then confirmation experiments were carried out to demonstrate that the NL-GS is able to measure sample induced aberrations independently of the laser source. This is based on the secondary light source created inside the sample which is mainly based on the focal volume produced through TPEF. This secondary light source is defined this as the NL-GS.

The NL-GS was used as the point source to measure focusing aberrations. In this case it was confirmed that the NL-GS behaves similarly to a physical point source such as a fluorescent bead, being able to be used in combination with the Shack-Hartmann WFS. This was followed by experimentally determining the minimum number of NL-GSs to be used for a given FOV and at different depths to efficiently correct for sample induced aberrations. The results revealed that off-axis aberrations are similar to on-axis aberrations even at different depths. This methodology is able to follow what it is predicted by theory. Here spherical aberration was dominant; therefore an exhaustive analysis was performed observing the spherical aberration components also considering the on-axis versus the off-axis aberrations. The results revealed that a single NL-GS can be used to correct most of the aberrations present in the FOV.

An adaptive optics (AO) path was designed and built on the existing NLM workstation to evaluate the performance of the developed concept using living samples. This design was based on a deformable mirror (DM) used for the wavefront correction of the whole microscope including the sample contribution.

The coupling aberrations were corrected using the excitation beam and a closed-loop configuration while the focusing aberrations where performed in an open-loop through the NL-GS concept.

In vivo C. elegans nematodes and mouse brain slices where used for the correction trials. The experiments were performed at different depths, using scattering pads, and using highly scattering samples.

The results revealed that the total intensity and contrast could be improved when the coupling aberrations correction was performed. However, the greater intensity improvements were observed at greater depths using the *C. elegans* nematodes and the increased scattering pad. This was observed at a depth of 127 µm where the improvement of the total generated intensity was of 22.59 times.

Finally for the more scattering sample (mouse brain slice) it was also possible to achieve an intensity improvement up to 5.69 times. However, it was observed that scattering will dominate as the imaging goes deeper inside the sample. This suggests the requirement of more power to image the sample or the implementation of other strategies such as the use of index matching media inside *in vitro* samples to reduce scattering. AO will have a larger impact on the correction when moderate scattering specimens are employed, as they allow imaging at deeper planes.

In this way the whole system was adapted based on the measurements carried out using the NL-GS concept to shape a DM in a way that it compensates the aberrations including the sample contribution.

Overall the presented strategies where employed to demonstrate on how to manipulate the different aspects that constitute the NLM: the ultra-short pulsed laser source, the coupling optics and the sample to be imaged, while at the same time, reducing sample manipulation. This was carried out to enhance the interaction between them, allowing pushing the performance of the imaging device towards its limits.

5.2. Future prospects

The challenges found during the development of this thesis for pushing NLM towards its limits such as: 1) the requirement of faster imaging, 2) having a compact and more efficient ultra-short pulsed laser system, and 3) aberration correction implemented on every imaging device are the aspects to be targeted and included into a compact imaging device..

For this goal, the interaction of the laser system, the coupling optics and the sample should be taken into account for the design of a compact device that includes the advantages gained with the strategies demonstrated in this thesis. The imaging system should be available for all public in order to generalize its use in clinics and hospitals. Ideally, the whole imaging device must be compact as current microscopes are still big, robust enough to be taken out from the laboratories, allowing it to be transferred to the place where the sample is. In addition, the imaging device should combine a laser source designed for the application to be targeted and enable imaging using different modalities such as TPEF, SHG, THG, etc in a simultaneous and efficient way.

The encountered challenges of this thesis should be considered as a whole for the development and integration of a solution. The faster scanning strategy could be carried out by implementing a compact laser system operating at an increased repetition rate and a reasonable FOM2p. However, one of the main aspects for having a reasonable FOM2p is the requirement of higher peak powers. To do this, the use of active optical elements for pulse compression and aberrations correction can be used. In this way the requirement of an active element that enables to manipulate the light in a way that it is possible to keep on pushing NLM towards its limits is desired.

In this sense, I have been actively involved on the design of devices to target such requirements considering the current difficulties of combining various methodologies in a single device.

Aiming to offer a simpler but efficient strategy to what state of the art devices offer, I have been actively involved in the design and testing of what it is called the super imaging unit (SIU) in collaboration with Citizen Japan,. This device will be based on a spatial light modulator attached to the rear plane of any microscope objective reducing the complexity of having to build a pulse compressor and a dedicated adaptive optics path in an existing setup. This is quite important as pupil conjugation and size adaptation can be eliminated together with the requirement of using large amounts of space in the optical table. In addition, this will enable minimizing the amount of the elements in the optical path, thus reducing the laser source power requirements.

As before, this unit is designed for the specific application of NL microscopy, it is compact, affordable and can be implemented into any microcopy technique. Importantly, it could potentially be used for further pushing NLM performance towards its limits, as it enables the manipulation of light for performing pulse compression [1], pulse shaping [2, 3] and AO using a single device [4] among many other applications not only limited to be used only for NLM.

These applications have already been reported to have an impact on NLM performance; however they are based on external, bulky and expensive devices. This will enable targeting the main challenges presented in this thesis.

Future applications that could be developed using chip-sized lasers are the design of lab-on-a-chip devices or micro-endoscopes. Here the main challenge is to have a compact head including the laser system. An optimized performance it is required to send the light through an optical fiber. I have already tested the possibility to perform imaging though a fiber bundle obtaining satisfactory results, however pulse pre-chirping is required. This could also be potentially solved using the SIU. All, this opens up interesting opportunities for a faster incorporation of the chip-sized semiconductor ultra-short pulsed light sources for portable NL imaging applications outside research labs.

References

1. P. Xi, Y. Andegeko, D. Pestov, V. V. Lovozoy, and M. Dantus, "Two-photon imaging using adaptive phase compensated ultrashort laser pulses," Journal of Biomedical Optics 14 (2009).
2. H. Kawano, Y. Nabekawa, A. Suda, Y. Oishi, H. Mizuno, A. Miyawaki, and K. Midorikawa, "Attenuation of photobleaching in two-photon excitation fluorescence from green fluorescent protein with shaped excitation pulses," Biochemical and Biophysical Research Communications 311 (2003).
3. G. McConnell, "Pulse shapes for optimized two-photon laser scanning microscopy," Journal of Physics D-Applied Physics 41 (2008).
4. C. Li, M. Xia, Q. Mu, B. Jiang, L. Xuan, and Z. Cao, "High-precision open-loop adaptive optics system based on LC-SLM," Optics Express 17 (2009).

Appendices

A. Appendix (*Sample culture and mounting protocols*)

1.1. C. elegans Nematode growth media

To make one liter of nematode growth media, the following items are required:

Item	Amount
NaCl	3 gr
Bacto agar	17 gr
Bacto peptone	5 g
1M CaCl2	1 ml
1M PPB	25 ml
5mg /ml Cholesterol in ethanol	1 ml
1M MgSO4	1 ml
Fungizone	0.4 µl
MiliQ Water	972 ml

To make 25 ml of 1M PPB, mix 3.3 ml of 1M K2HPO4 with 21.7 ml of 1M KH2PO4.

Mix the NaCL, the agar and peptone and add 972 ml of miliq water. Cover the bottle and autoclave.

Cool the bottle in the water bath for 20 minutes at 55ºC

Add the CaCl2, MgSO4, 1M PPB, cholesterol and fungizone, then mix thoroughly.

In the laminar flow cabin, pour the nematode growth media into Petri dishes trying to achieve an even surface.

Leave the plates overnight at room temperature.

1.2. Luria Broth for bacterial culture

Item	Amount
Yeast extract	5 gr
Tryptone	10 gr
NaOH	2 g
NaCl	5gr
Bacto agar	15 gr
MiliQ water	1 lt

Mix all the items contained on the list inside a bottle. Close the container and autoclave the solution for 30 minutes.

Cool down the mixture in the water bath set at 55ºC.

Inside the laminar flow cabin, place the mixture in Petri dishes and allow them to cool at room temperature.

Bacterial suspension is obtained by seeding bacteria from a plate into 10 ml of LB media in a tube. Once this has been done the container must be left overnight in a shaking incubator set at 375ºC

Bacteria OP50 (*Escherichia coli*) can be then added to the plates and left overnight at room temperature.

1.3. C. elegans freezing media

Item	Amount
NaCl	0.585g
KH2PO4	0.68
Glycerol	30g
1M NaOH	0.56 ml
MiliQ water	100 ml

Mix all the items listed above, inside a container. Close the container and autoclave the solution for 30 minutes.

Cool down the mixture in the water bath set at 55ºC.

Add to the solution 0.1 M MgSO4 and 100 ml of M9 buffer and mix.

1.4. C. elegans M9 Protocol

Item	Amount
NaCl	5gr
KH2PO4	3 gr
NaH2PO4	6 gr

Dissolve the ingredients in one liter of distilled water inside a container. Close the container and autoclave the solution for 30 minutes.

Cool down the mixture in the water bath set at 55ºC.

Inside the laminar flow cabin add 1 ml of 1M MgSO4

1.5. Adult C. elegans mounting protocol for in vivo imaging

The selected *C. elegans* strains to be imaged are grown in nematode growth media and feed with OP50 (*Escherichia coli*). Adult worms were anesthetized using 0.8 µl of 25-mM sodium azide (NaN3) and mounted on a 2% agar pad sandwiched between two cover-glasses (No. 1 - 0.13 to 0.16 mm). The preparations were sealed using melted paraffin and were imaged at room temperature.

1.6. Other model organisms mounting protocols for in vivo imaging

For zebrafish imaging, embryos where dechorionated and then anesthetized using 0.016% tricaine. These were mounted on 1.5% low melting agarose between two cover-glasses glasses (No. 1 - 0.13 to 0.16 mm). The preparations were sealed using nail polish and were imaged at room temperature.

For drosophila imaging, embryos were mounted on 1.5% low melting agarose between two cover-glasses glasses (No. 1 - 0.13 to 0.16 mm) and employing a set of spacers to avoid altering the embryo shape. The preparations were sealed using nail polish and were imaged at room temperature.

1.7. C. elegans growth and mounting protocol for developmental imaging.

N2 wild type *C. elegans* are grown in nematode growth media and fed with OP50 (*Escherichia coli*). Worms were synchronized and embryos were attained in order to get a large number of specimens for the imaging experiments. A large number of embryos, from different developmental stages were mounted on a poly-L-lysine (Poly-L-lysine hydrobromide, Sigma Aldrich) coated thin cover-glass (No. 1 thickness) with 10 µl of M9

buffer. The embryos where sandwiched between two thin glass cover-glasses which were separated with 50μm polystyrene micro spheres (Polymer microsphere suspension, Thermo Scientific). All this was done to avoid damaging and altering the embryos original shape 2. Samples were sealed with melted paraffin for sample stability and were imaged at constant room temperature (20 ºC).

1.8. C. elegans mounting protocol for depth imaging

The selected strains to be imaged are grown in nematode growth media and feed with OP50 (*Escherichia coli*). Adult worms were anesthetized using 0.8 μl of 25-mM sodium azide (NaN3). These where mounted in 3 different arrangements in order to have an additional interface, producing different magnitudes index mismatch and scattering effects. These were: i) A sample preparation where the nematodes were sandwiched between two cover-glasses, ii), a sample having a 1% agar pad of 90 μm (Scharlab, Spain AG00200500) facing the microscope objective with the nematodes mounted on top, sandwiched between two cover-glasses, and iii) a sample preparation with the same mounting procedure as the second one, but having an agar pad with a final concentration of 2%. The preparations were sealed using melted paraffin and were imaged at room temperature.

1.9. Mice brain slices preparation and mounting protocol for depth imaging

With the aim to obtain mice expressing green fluorescent protein (GFP) in sparsely distributed neurons in the cortex, DNA construct CAG-GFP (1 μg/μl) was electroporated in embryonic day 15 animals by *in utero* electro-poration. After birth, animals were allowed to develop normally to collect brains at postnatal day 16. Animals were perfused and mouse brain slices having a total thickness of 60 μm (cut on a cryostat) where obtained. These were placed on a bottom glass Petri dish containing fresh medium to keep the slice in optimum conditions. The preparations were imaged at room temperature.

B. Appendix Full *Microscopy setup*

1.1. Complete nonlinear microscopy setup

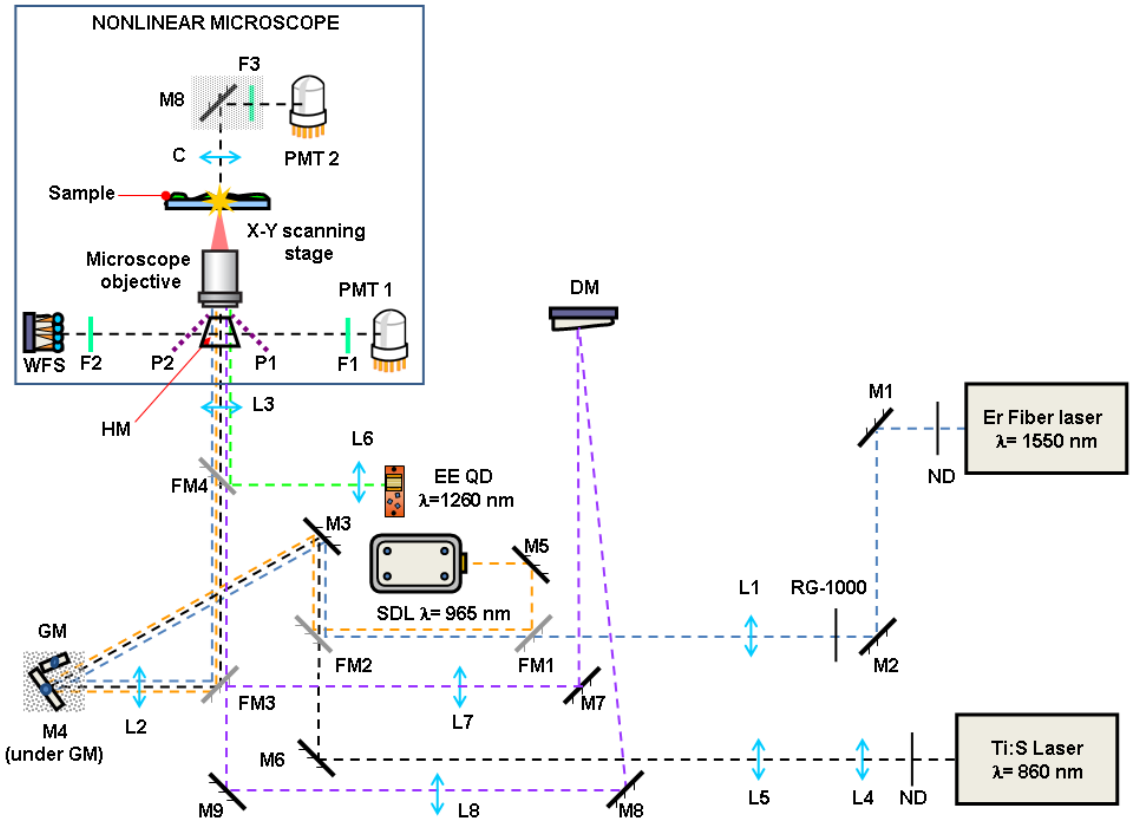

Experimental setups (developed in this thesis having the same layout as they are mounted at the optical table) built for two-photon excited fluorescence (black, yellow and green paths), Second harmonic generation (black and yellow paths), third harmonic generation (blue path) and Adaptive optics (purple path). Ti:S is the titanium sapphire laser at 860 nm and Er Fiber laser is the FemtoFiber FFS laser at 1550 nm, SDL is the Semiconductor disk laser at 965 nm and EE QD are the quantum dot edge emitting devices at 1260 nm.

ND, Neutral density filters; M#, mirrors; RG1000, bandpass filter; L#, lenses; FM#, flip mirrors; GM, galvanometric mirrors; DM, deformable mirror; HM, dichroic filter; C, condenser optics; F#, band pass filters; PMT#, photomultiplier tubes; P#, microscope output ports; and WFS, wavefront sensor.